Atomistic Simulations on the Mechanical Behavior of Bio-inspired Brittle Matrix Nanocomposites

A thesis submitted
in partial fulfillment for the degree of

Doctor of Philosophy

by

MATHIAZHAGAN S.

Department of Aerospace Engineering
INDIAN INSTITUTE OF SPACE SCIENCE AND TECHNOLOGY
Thiruvananthapuram

June 2017

Atomistic Simulations on the Mechanical Behavior of Bio-inspired Brittle Matrix Nanocomposites

A thesis submitted
in partial fulfillment for the degree of

Doctor of Philosophy

by

MATHIAZHAGAN S.

Department of Aerospace Engineering
INDIAN INSTITUTE OF SPACE SCIENCE AND TECHNOLOGY
Thiruvananthapuram

June 2017

CERTIFICATE

This is to certify that this thesis entitled **Atomistic Simulations on the Mechanical Behavior of Bio-inspired Brittle Matrix Nanocomposites** submitted by **Mathiazhagan S**, to the Indian Institute of Space Science and Technology, Thiruvananthapuram, in partial fulfillment for the award of the degree **Doctor of Philosophy**, is a bona fide record of the research work carried out by him under my supervision. The contents of this thesis, in full or in parts, have not been submitted to any other Institute or University for the award of any degree or diploma.

Dr. S. Anup
Supervisor
Associate Professor
Department of Aerospace Engineering

Dr. A. Salih
Head of the department
Department of Aerospace Engineering

Place: Thiruvananthapuram
June 2017

DECLARATION

I declare that this thesis titled **Atomistic Simulations on the Mechanical Behavior of Bio-inspired Brittle Matrix Nanocomposites** submitted in partial fulfillment of the Degree of **Doctor of Philosophy** is a record of original work carried out by me under the supervision of **Dr. S. Anup**, and has not formed the basis for the award of any degree, diploma, associateship, fellowship or other titles in this or any other Institution or University of higher learning. In keeping with the ethical practice in reporting scientific information, due acknowledgments have been made wherever the findings of others have been cited.

Place: Thiruvananthapuram
June 2017

Name : Mathiazhagan S
Roll No. : SC11D022

ACKNOWLEDGMENTS

First I would like to express my deepest gratitude to my advisor Dr. S. Anup who gave me the opportunity to work on some of the most challenging problems. I am deeply indebted for his guidance and support.

I am also deeply indebted to my doctoral committee (DC) members: Chairmen, DC, Dr. A. Salih and Professor Kurien Issac, Department of aerospace engineering, Indian Institute of Space Science and Technology (IIST), Thiruvananthapuram, Professor M. S. Sivakumar, Department of Applied Mechanics, Indian Institute of Technology (IIT) Madras, Dr. D. Roy Mahapatra, Department of Aerospace Engineering, Indian Institute of Science (IISc) Bangalore, and Dr. P. Raveendranath, Department of Aerospace Engineering, and Dr. Umesh R. Kadhane, Department of Physics, from Indian Institute of Space Science and Technology (IIST) Thiruvananthapuram.

Lastly, I offer my gratitude and blessings to my father (A. Sekaran), my mother (S. Parvathi), my brothers (S. Muniraj and S. Muruganandam), my friends, my coworkers and all who supported me in any respect during the completion of my PhD.

ABSTRACT

There is a huge interest in the development of materials with superior mechanical properties, which have simultaneously high stiffness, strength, and toughness. Brittle matrix composites (BMC) are good candidates for such materials; they possess high stiffness and strength; however, their low toughness limits their industrial applications. In order to develop advanced materials with high toughness, the principles of structural biocomposite materials such as the staggered arrangements of reinforcements and the reinforcements in the form of nanometer-sized platelets are carried forward to the brittle matrix composites (BMC) in this thesis.

The mechanical behavior of bio-inspired brittle matrix nanocomposites is studied using atomistic simulations; moreover, the differences and similarities between the regularly staggered (RSM) and stair-wise staggered (SSM) arrangements of platelets are examined in detail. The effects of different strain rates on both the models are analyzed; different strain rate regimes and critical strain rates are found based on the different deformation mechanisms observed. The effect of aspect ratio (AR) of platelets is investigated and the existence of two critical ARs for SSM is found: a smaller critical AR which separates the platelet pullout and platelet fracture mechanisms, and a larger critical AR upto which the composite strength increases and remains constant thereafter. Further, the study of effect of platelet-matrix interface strength is done. The existence of critical interface strength is shown through our atomistic simulations; decohesions between platelet and matrix occur when the interface strength is below this critical value. Moreover, when the interface strength is weak i.e., below this critical value, SSM models show high toughness due to platelet sliding. However, in RSM models, strong interface strengths lead to high toughness. We also studied the length scale effect on these BMCs and the existence of critical length scale is found. The pull-out of platelet is the dominant mechanism and observed in all length scales studied. Whereas, a large amount of dislocation activities in matrix are observed when the length scale is above the critical length scale and geometric confinement on dislocation activities are found on smaller length scales. This thesis provides beneficial guidelines in designing tough bio-inspired brittle matrix nanocomposites.

TABLE OF CONTENTS

LIST OF FIGURES

LIST OF TABLES

ABBREVIATIONS

RSM	Regularly Staggered Model
SSM	Stair-wise Staggered Model
CMC	Ceramic Matrix Composites
BMC	Brittle Matrix Composites
CMNC	Ceramic Matrix Nanocomposites
MMNC	Metal Matrix Nanocomposites
SFRC	Short Fiber Reinforced Composites
MD	Molecular Dynamics
EAM	Embedded Atom Method
LJ	Lennard-Jones
LAMMPS	Large-scale Atomic\Molecular Massively Parallel Simulator
EM	Energy Methods
CNM	Coordinate Number Methods
CSP	Centrosymmetric Parameter
KE	Kinetic Energy
PE	Potential Energy
SR	Strain Rate
AR	Aspect Ratio
IS	Interface Strength
SLA	Shear Lag Analysis

TSC	Tension-Shear Chain model
KTM	Kelly-Tyson Model
ROM	Rule of Mixtures
FEM	Finite Element Methods
IFSS	Interfacial Shear Strength
IASS	Interatomic Shear Strength
RSS	Resolved Shear Strength
HP	Hall-Petch
2D	Two Dimension
3D	Three Dimension

SYMBOLS

σ_{LJ}	Length parameter in Lennard-Jones (LJ) potential
ϵ_{LJ}	Energy parameter in Lennard-Jones (LJ) potential
ε_{yy}	Strain along Y direction
σ_{yy}	Stress along Y direction
$\dot{\varepsilon}_{yy}$	Strain rate applied along Y direction
V_{yy}	Velocity applied along Y direction
L_0	Initial length of the model along Y direction
V	Volume in the case 3D model and area in the case of 2D model
r	Distance between two atoms
r_{cut}	Cut–off Radius
$r_y^{\alpha\beta}$	Y component of distance between atom α and another atom β
$F_y^{\alpha\beta}$	Y component of force between atom α and another atom β
$\phi_{LJ}(r)$	LJ potential function, which is a function of r
$\phi'_{LJ}(r)$	First derivative of LJ potential with respect to r
$\phi_{LJ}^{mod}(r)$	Modified LJ potential function
$\vec{a_x}$	Translation vector along X direction
$\vec{a_y}$	Translation vector along Y direction
$\vec{i}$	Unit vector in the X Direction
$\vec{j}$	Unit vector in the Y Direction
F	Platelet thickness

M	Matrix thickness or Platelet transverse gap
L	Platelet length
G	Platelet axial gap
P	Platelet overlap length
N_p	Number of platelets
N_a	Total number of atoms
Δt	Times step in MD simulations (0.001)
σ^p_{crit}	Tensile strength of platelet
σ^m_{crit}	Tensile strength of matrix
σ^i_{crit}	Tensile strength of interface
E_p	Young's modulus of platelet
E_m	Young's modulus of matrix
E_i	Young's modulus of interface
G_p	Shear modulus of platelet
G_m	Shear modulus of matrix
G_i	Shear modulus of interface
τ^p_{crit}	Shear strength of platelet
τ^m_{crit}	Shear strength of matrix
τ^i_{crit}	Shear strength of interface
ε^p_{crit}	Tensile failure strain of platelet
ε^m_{crit}	Tensile failure strain of matrix
ε^i_{crit}	Tensile failure strain of interface
γ^p_{crit}	Shear failure strain of platelet
γ^m_{crit}	Shear failure strain of matrix

γ_{crit}^{i}	Shear failure strain of interface
$AR_{C_{CS}}^{MD,N2}$	Critical AR corresponding to critical stress obtained from MD for RSM
$AR_{C_{CS}}^{MD,N5}$	Critical AR corresponding to critical stress obtained from MD for SSM
$AR_{C_{FS}}^{MD,N2}$	Critical AR corresponding to flow stress obtained from MD for RSMl
$AR_{C_{FS}}^{MD,N5}$	Critical AR corresponding to flow stress obtained from MD for SSM
$AR_{C}^{TSC,N2}$	Critical AR obtained from TSC for RSM
$AR_{C}^{TSC,N5}$	Critical AR obtained from TSC for SSM
$AR_{C,1}^{KTM,N5}$	First critical AR obtained from KTM for SSM
$AR_{C,2}^{KTM,N5}$	Second critical AR obtained from KTM or SSM

CHAPTER 1

Background

1.1 Introduction

Biocomposite materials, such as mollusk shells, bone, antler and etc., exhibit remarkable combinations of stiffness, strength and toughness which equal or exceed properties of their individual constituents; these biological materials are composites of calcite, hydroxyapatite or aragonite mineral platelets dispersed in a matrix of collagen or chitin (Ashby et al., 1995; Fratzl et al., 2004; Dunlop and Fratzl, 2010). In contrast, for most engineering materials, strength and toughness are usually mutually exclusive (Ritchie, 2011). To illustrate this, the toughness versus stiffness values of both the engineering and biological materials are shown in Fig 1.1 (Espinosa et al., 2009; Qin et al., 2009). The data lie on banana curve: an inverse relation between increasing toughness and

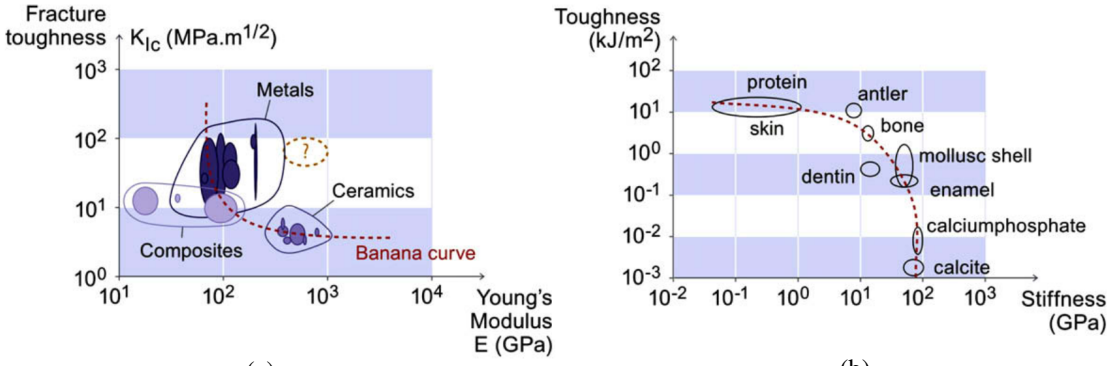

Figure 1.1 Toughness versus stiffness for (a) engineering materials and (b) biological materials. Figures adopted from Espinosa et al. (2009). The yellow region shows the property region of high toughness and stiffness that may be accessible through creating bio-inspired materials.

decreasing stiffness. The soft constituents occupy the upper left regions and stiff constituents occupy the lower right regions. The engineering composites occupy the lower left region which indicates a combination of low stiffness and low toughness. In contrast, the biocomposites occupy the upper right region which signifies a combination of

high stiffness and high toughness (Wegst et al., 2015). This shows the superior mechanical properties of natural composites in comparison to that of engineering composites. The strategies which nature utilizes to achieve these superior mechanical properties can be made use of in the design and development of high performance synthetic materials.

1.2 Mechanical Principles of Biological Materials

Biocomposite materials achieve superior mechanical properties using various strategies. Extensive research works have been conducted to find out these strategies; these research works include the following: i) Experiments done to observe the structure and deformation behavior of various biological materials (Landis et al., 1993; Kamat et al., 2000; Nalla et al., 2003; Gupta et al., 2004, 2006). ii) Theoretical models developed to understand the structure-property relationships of their nanostructures. Though models such as shear-lag type which were developed for discontinuous fiber reinforced composites were applied to biological nanocomposites (Kotha et al., 2000, 2001; Wei et al., 2012), the tension-shear chain (TSC) model which was developed by Jager and Fratzl (2000) and Gao et al. (2003) is the most popular model as it captures the prominent load transfer feature in these materials; that is the tensile stress is carried by platelets and shear stress by matrix (See Fig 1.2i for TSC model). iii) Various numerical simulations performed to elucidate salient mechanisms underlying in these biological materials. These simulations comprise both the continuum mechanics based such as finite element methods (FEM) (Ji, 2008; Luo et al., 2011; Yuan et al., 2011; Hambli and Barkaoui, 2012) and the explicit molecular dynamics (MD) simulations (Dubey and Tomar, 2008; Bhowmik et al., 2009; Qin et al., 2012; Libonati et al., 2014).

Few of the vital strategies which help natural biological materials to achieve the superior mechanical performance are listed here (Rho et al., 1998; Ji and Gao, 2010; Launey et al., 2010a; Wang and Gupta, 2010; Meyers et al., 2013) :

- Hierarchical structure. These materials have different structural configurations at different length scales, with each level building on the previous levels. For example, nacre has two to three orders of lamellar structure, and bone has up to seven orders of hierarchy. To study the effect of hierarchy on the mechanical properties, Zhang et al. (2011) developed a quasi-self-similar hierarchical composite model. They showed

that though the stiffness and strength decrease with number of hierarchical levels, the toughness increases initially and decreases above a optimum number of these levels. This optimal number of hierarchy is consistent with the experimentally observed hierarchical levels for different biological materials. Their study showed the significance of hierarchical structure in improving the toughness of biological materials.

- Staggered platelet–matrix composite. The structure found at the smallest level which is also referred to as the basic building block or the nanostructure of the hierarchical structured materials is made up of hard platelet-type inclusions embedded in soft protein matrix in a staggered alignment pattern (Rho et al., 1998; Ji and Gao, 2004). For instance, nacre (Fig 1.2a) has a nanostructure of aragonite mineral platelets (95–99%) embedded in a protein matrix (1–5%) (See Fig 1.2b, brick-and-mortar–BM). Bone (Fig 1.2e) has a nanostructure consisting of hydroxyapatite mineral platelets (50–60%) staggered in a collagen matrix (40–50%) (See Fig 1.2f, mineralized collagen fibrils–MCF). Idealized arrangements of platelets embedded in a matrix can be derived from these biological nanostructures–the regularly staggered model (RSM, shown in Fig 1.2c) and stair-wise staggered model (SSM, shown in Fig 1.2g). Using TSC model, Gao (2006), Zhang et al. (2010) and Lei et al. (2013) studied the variation of mechanical properties for different staggered patterns and showed that these RSM and SSM arrangements were able to achieve overall excellent mechanical performance by simultaneous optimization of higher strength and toughness.

- Nanometer–sized constituents. The hard platelets in the basic building blocks of most of these biocomposite materials have a size in nanometers. For example, aragonite bricks in nacre are a few hundred nanometers thick, while hydroxyapatite mineral crystals in the bone have a thickness of few nanometers. Gao et al. (2003) showed that materials become insensitive to flaws below a critical length which usually occurs at nanoscale; they obtained this critical length by comparing the fracture strength of cracked platelet obtained from Griffith criterion with the strength of defect-free platelets. Therefore, the nanometer size is indeed useful in designing materials with superior mechanical properties.

- Polymeric matrix. The matrix of the biological nanocomposites is made up of polymeric materials such as collagen. This matrix is crucial to mechanical behavior in

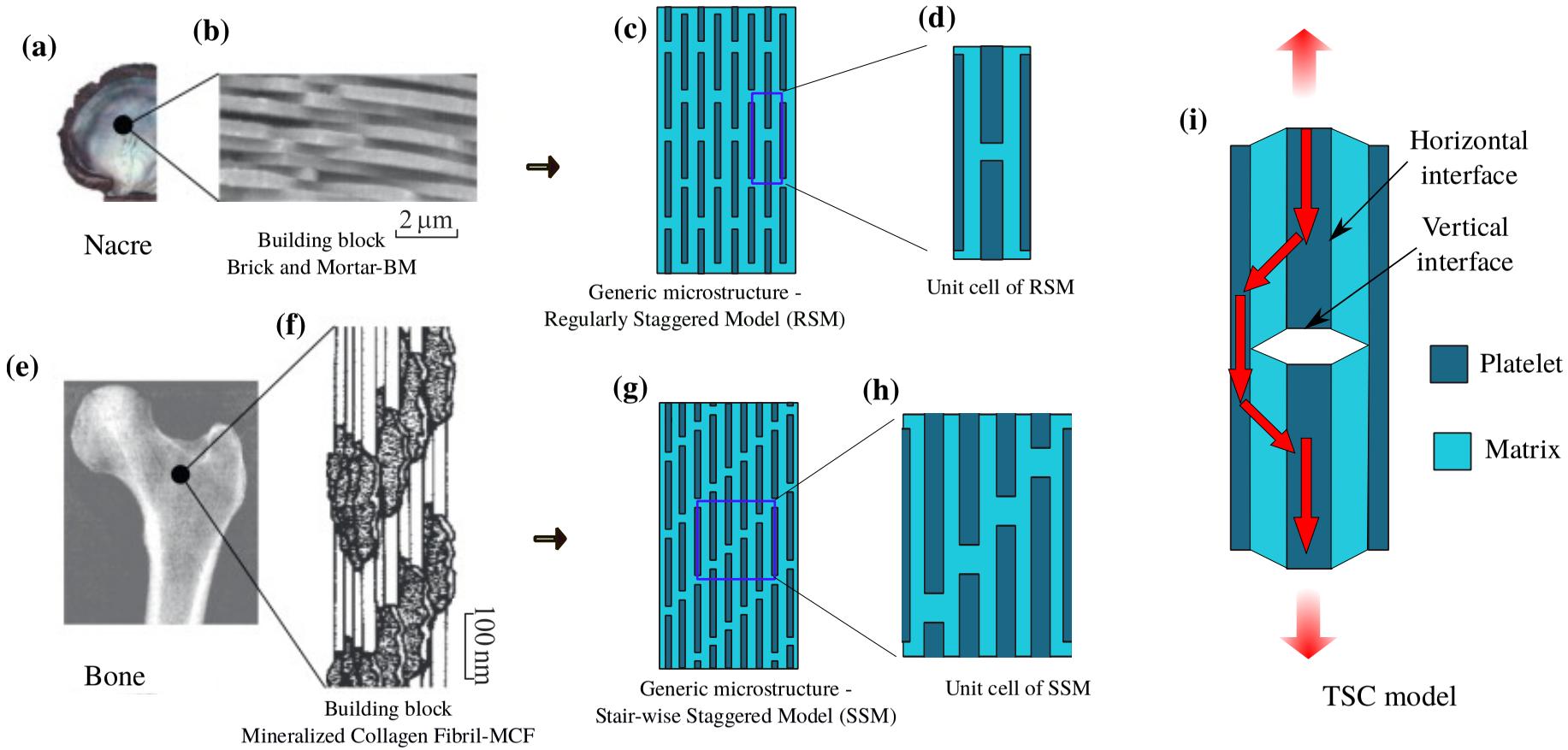

Figure 1.2 Biological and bio-inspired/idealized nanocomposites: (a) macroscopic image of nacre, (b) TEM image of its microstructure, (c) idealized microstructure–regularly staggered model (RSM), and (d) unit cell of the RSM; (e) macroscopic image of bone, (f) TEM image of its nanostructure, (g) idealized microstructure–stair-wise staggered model (SSM), and (h) unit cell of the SSM; and, (i) tension-shear chain (TSC) model developed for biological nanocomposites (Some figures are taken from Ji and Gao (2010)).

many aspects such as transferring of load through shear deformation, trapping cracks through matrix softness, and dissipating energy through its large deformation and viscoelastic properties (Ji and Gao, 2004; Gao, 2006).

- Interface property. As the mineral platelets have nanoscale size, the volume fraction of the protein-mineral interface can be enormous. Therefore, the interface properties should play a crucial role in the overall mechanical properties. Atomistic and continuum studies have shown that the interface strength depends on both the size and the geometry of mineral crystals and can be optimized through the miniaturization of minerals at the nanoscale (Ji, 2008, 2010).

- Optimal aspect ratio. Aspect ratio (AR) is defined as the ratio of length of the platelet to its thickness. The aspect ratio of platelets is very large in these biological materials, approximately 8–14 for nacre (Jackson et al., 1988; Rabiei and Bekah, 2010) and 30–40 for bone (Ji and Gao, 2004). The optimal value of the aspect ratio should balance many aspects of the mechanical properties of the nanostructure, e.g., the limiting strength of mineral, protein, and interface; the elastic stability of the nanostructure; and an effective load transfer in the nanocomposite structure of biological materials (Chen et al., 2009; Wei et al., 2012). The pullout of mineral platelets due to interface failure is a major failure mode and is necessary to achieve higher toughness; this type of failure occurs only if the AR is below an optimal value.

- Optimal modulus ratio. Modulus ratio (MR) is defined as the ratio of Young's modulus of the platelet to that of the matrix. The modulus ratio is about 1000 for biological materials. However, it is demonstrated that the optimal AR depends on MR; therefore this high value of MR is necessary to maintain optimal AR in biological materials (Chen et al., 2009; Wei et al., 2012).

From the above discussions, it is clear that the superior mechanical properties of the biological materials is mainly attributed to the stiffening, strengthening and toughening mechanisms occurring at the nanocomposite structure of these materials. Therefore, this nanocomposite structure, i.e., staggered arrangements of hard platelets reinforced in soft matrix, is believed to have huge potential for developing nanocomposite materials which is discussed further.

1.3 Bio-inspired Nanocomposites

In recent years, nanocomposite materials have gained wide spread attention, because they possess attractive mechanical properties, and unique electrical and thermal properties (Cammarata, 1994; Gleiter, 2000; Dzenis, 2008). In these nanocomposites, nanoparticles, nanotubes or graphenes are used as reinforcements in matrices such as polymers, metals or ceramics. These nanocomposites are manufactured in a way very similar to the other traditional composites; they are made by homogeneous dispersion of reinforcements in matrices. There are increasing applications for these nanocomposites in the form of thin films, coatings and bulk materials in aerospace, micro-electromechanical systems, energy devices and the biomedical industries (Zhang et al., 2004; Winey and Vaia, 2007; Yang et al., 2014; Zhang et al., 2016b). However at present, most man-made structural nanocomposites based on traditional approaches exhibit mechanical properties that fall short of their biological counterparts (Dzenis, 2008; Ji and Gao, 2010). A critical challenge in nanocomposite fabrication is the ability to realize materials that allow the exceptional mechanical properties (e.g., tensile strength, Young's modulus, and toughness) of nanoscale reinforcements to manifest in the macroscale properties of bulk materials. More specifically, the deficiency in the properties of traditional nanocomposites is related largely to the difficulty of obtaining well–dispersed large–volume fractions of nanoparticles and to a lack of geometrical and structural control. Moreover, there is insufficient understanding of the load transfer between the matrix and the nanoscale components. Natural biological nanocomposites provide a useful platform to study possible strategies for resolving these issues. The significant progress made in the understanding of the high toughness of biological nanocomposites can be applied to the development of the artificial bio-inspired nanocomposites (Launey and Ritchie, 2009; Sakhavand and Shahsavari, 2015; Wegst et al., 2015). Synthetic structural materials that could mimic such natural design could transform many engineering disciplines, especially the energy-related and transportation industries (Ortiz and Boyce, 2008; Launey and Ritchie, 2009). Therefore, the purpose is to stimulate further discussions on possible ways to suggest guidelines for the development of novel bio-inspired nanocomposites.

Many experiments have been carried out for the synthesis of novel bio-inspired

nanocomposites in the laboratory (Sellinger et al., 1998; Bonderer et al., 2008; Ortiz and Boyce, 2008; Dubey and Tomar, 2010; Wang et al., 2012). These biomimicking activities strongly validated the mechanical principles found in biomaterials. Here a few examples of man-made bio-inspired nanocomposites are discussed. For example, in order to duplicate the ordered brick-and-mortar arrangement and the ionic cross-linking of tightly folded biopolymer of nacre, Tang et al. (2003) prepared a nanocomposite with cationic polyeletrolytes (poly-diallyl-dimethyl-ammonium chloride – PDDA) and clays (montmorillonite–MTM) using layer-by-layer (LBL) assembly process; this composite's (PDDA/MTM) Young's modulus (11 GPa) and ultimate tensile strength (106 MPa) values approached that of nacre and lamellar bones, respectively. Podsiadlo et al. (2007) developed nacre-mimetic layered nanocomposites materials made up of poly(vinyl alcohol)/montmorillonite treated with glutaraldehyde (PVA-GA/MMT) using LBL assembly process. This polymer nanocomposites had superior stiffness (106 GPa) and strength (400 MPa), which was one order of magnitude higher than those of analogous nanocomposites; but with lower toughness. Moreover,the LBL assembly process is limited to the fabrication of thin films.

Further, the ice-templating or freeze casting method was developed to manufacture bulk nanocomposite materials. For example, using ice templeting process Munch et al. (2008) and Launey and Ritchie (2009) developed a suite of bulk nanocomposite materials using alumina (Al_2O_3) and polymethyl methacrylate (PMMA) constituents in lamellar and brick-and-mortar form; these nanocomposites have a tensile strength of about 200 MPa and fracture toughness of about 30 MPa$\sqrt{\mathrm{m}}$. The toughness of such composites is at least two orders of magnitude higher than its constituents, which is primarily attributed to the interfacial design and chemo-mechanics of the interface. Further, this group extended the synthesis of hybrid organic-inorganic composite to hybrid ceramic-metal composites (Al_2O_3/Al–Si) (Launey et al., 2010b). In particular, in this work lamellar Al_2O_3/Al–Si composites with a 36 vol% ceramic content were processed, and were found to display strengths of approximately 300 MPa and fracture toughness values that exceeded 40 MPa$\sqrt{\mathrm{m}}$. More recently using ice-templating process, Bouville et al. (2014) developed a superior material using almost 100% ceramic (Al_2O_3) material; this material has a higher stiffness (290 GPa), higher strength (470 MPa), and higher toughness (22 MPa$\sqrt{\mathrm{m}}$) values. Further, layered nanocomposites based on two

dimensional graphene-oxide (GO) with various functional groups have been developed with outstanding mechanical properties (Cui et al., 2014; Zhang et al., 2016b). In spite of these developments, few biomimetic materials have mechanical performance as good as natural biological materials such as nacre and bone. This could be because of technological restrictions and unclear understanding of the underlying toughening mechanisms and design principles of bio-inspired nanocomposites. Higher tensile strength and Young's modulus are relatively easy to achieve for artificial materials, but a simultaneous replication of high fracture toughness and other properties seems to be difficult. Therefore, a deeper understanding is needed which will be helpful for optimal design and fabrication of novel biomimetic materials.

It also needs to be mentioned that many studies exist where the biological nanocomposites are idealized and the relationships between the structure and properties are explored for the purpose of developing bio-inspired nanocomposites (Zhang et al., 2010; Begley et al., 2012; Shao et al., 2014; Barthelat, 2014; Rajan and Curtin, 2016; Khandelwal et al., 2017) (Refer Fig 1.2 for biological and bio-inspired/idealized nanocompoistes). For example, Begley et al. (2012) carried out a micromechanical analysis of the uniaxial response of idealized synthetic "brick and mortar" composites comprising platelets bonded together with a thin matrix. Their analytical model gave connections between the macroscopic mechanical properties and microstructure. In contrast to the TSC model, they considered the bonding at the vertical interface between the matrix to platelets (See Fig 1.2i for vertical interface). They demonstrated that for synthetic materials with strong mortar/brick bonding, the vertical interfaces play an important role in contributing to the overall composite stiffness; for short bricks, the vertical interfaces also play a significant role in raising the peak strength of the composite. However the predictions of their model are limited to elastic platelets, elastic perfectly plastic matrices and the volume fraction of matrix lower than 40%.

Thus, once much progress in characterization of biological materials had occurred (discussed in the previous section), the design of nanocomposites inspired from biological materials were undertaken through various manufacturing processes and analytical modeling of the idealized composites (discussed in above paragraphs). Thus, rapid growth in the field of bio-inspired nanocomposite materials is being witnessed. Though basic design guidelines for the fabrication of superior mechanical performance is ob-

tained from continuum mechanics based analytical methods, these methods lack the incorporation of plastic and toughening mechanisms that can occur in the bio-inspired nanocomposite materials with metallic and ceramic matrices. Numerical simulations such as molecular dynamics (MD) play a critical role in understanding these deformation and failure mechanisms as they consider the discrete nature of materials from the first principles. Moreover, MD simulations do not require any a priori assumptions of the deformation processes, and can capture size effect and failure of materials; these are not possible with continuum based simulations and theories. In this thesis also, MD simulations are used to find out the mechanisms active in these bio-inspired nanocomposite materials.

Basic design guidelines for developing bio-inspired nanocomposites have been proposed using explicit MD simulations. For example, Broedling et al. (2008) and Sen and Buehler (2009) conceived bio-inspired metallic matrix nanocomposites (MMNC) and analyzed their behavior using atomistic simulations. They mimicked the following strategies of nature in their MMNC: (i) the regularly staggered pattern of platelets, (ii) nanometer-sized platelets, (iii) ductile matrix phase (lesser in ductility compared to biological counterpart), and (iv) small modulus ratio between platelet and matrix (much smaller compared to that observed in natural biocomposites).

Broedling et al. (2008) considered MMNC made of hard nanosized Ni platelets embedded in soft Al matrix and studied the size dependent material properties and deformation mechanisms over a wide range of length scales with a fully atomistic resolution using a quasi-two-dimensional model. Their simulations revealed that dislocation nucleation, dislocation glide, deformation twinning as well as interfacial slip and decohesion occur on all investigated length scales. However, a transition in the dominant deformation mechanism occurs; interfacial sliding at small length scales and dislocation processes at larger length scales. It is also found that at larger length scales the geometric constraint on dislocation processes is relieved and the strength of the material decreases in agreement with the Hall–Petch relation.

Further, using full atomistic simulations, Sen and Buehler (2009) investigated model nanocomposite material made of nanosized hard–metal reinforced in soft–metal in regularly staggered pattern along with strong and soft interfacial behavior. They found that beyond a critical aspect ratio (AR_C), the flow stress saturates, and increase in aspect

ratio has no further effect. Moreover, they showed that the spacing between platelets perpendicular to the direction of loading has a Hall-Petch like effect on flow stress. Further, a comparison of the effect of various geometrical parameters on flow stress showed that a large improvement over the unreinforced matrix flow strength is possible by systematically designing the nanostructure.

In this thesis, the implementation of design principles of biological materials in the development of ceramic matrix or in more general brittle matrix nanocomposites is considered which is discussed in detail in the next section.

1.4 Novel Bio-inspired Ceramic-Matrix Nanocomposites

Monolithic structural ceramics such as Al_2O_3, ZrO_2, SiC, and Si_3N_4 have reasonably high Young's modulus (100–400 GPa) and strength (400–1100 MPa) but are brittle. They have very low intrinsic toughness of roughly 1 to 3 MPa$\sqrt{\mathrm{m}}$. These materials suffer from almost a complete lack of plastic deformation; this is due to the absence of mobile dislocation activity, although other modes of inelastic deformation, such as microcracking and in situ phase transformation, can provide limited alternative deformation mechanisms (Evans, 1990; Rosso, 2006; Launey and Ritchie, 2009; McEntire et al., 2015). As the ceramic materials are intrinsically brittle, they can only be toughened by extrinsic toughening mechanisms, such as crack deflection, crack bridging and/or sliding between crack surfaces; that is to make composites via addition of fibers, whiskers or particles reinforcements, and zirconia phase transformation reinforcing, etc (Evans and Marshall, 1989; Curtin, 1991). Many traditional micro-scale ceramic composite are developed by these methods. In addition, recently many nano-scale ceramic composites or ceramic nanocomposites, such as Al_2O_3/SiC, Si_3N_4/SiC; MgO/SiC; Mullite/SiC, were developed using traditional approaches to enhance the toughness of ceramics. These are all made by a homogeneous dispersion of the ceramic nano-reinforcements (such as SiC particle with size of 200 nm) in a ceramic matrix (such as Al_2O_3 or Si_3N_4) (Sternitzke, 1997; Ferroni and Pezzotti, 2002). Unfortunately, the improvement of mechanical properties is limited for both types of materials: traditional micro-scale and nano-scale ceramic composites. Inspired by the structure of nacre, researchers have suggested an alternative way to synthesize tough ceramics, such

as multilayered structures, instead of homogeneously dispersed compositions (Clegg et al., 1990; Wang et al., 2012). Though the toughness of multilayered composites is improved compared to the homogeneously dispersed ceramic composites, it is far below the mechanical performance of biological materials.

Another methodology adopted to address the issue of low toughness was to use CNTs, graphene, and SiC nanofibers as reinforcements in ceramic matrices. For example, Tomar et al. (2010) and Samvedi and Tomar (2009) studied the nanocomposite made up of spherical nanosized SiC particles on Si_3N_4 matrix using continuum based mesoscale cohesive finite element method (CFEM) as well as explicit atomistic based molecular dynamics (MD) simulations. The researchers demonstrated that the second–phase particles have two important effects. If the second–phase particles are present in front of the crack tip, they weaken the microstructure because of the stress concentration caused by them; however, if they are present near grain boundaries (GBs), they cause the crack bridging effect, with an increase in the strength of the microstructure. In addition, their analyses also pointed out that the strengthening of the nanocomposite by placing second-phase particles along grain boundaries is only possible for a selective few second-phase particle sizes, with interparticle spacing being another important factor. Moreover, the researchers showed that the temperature dependent strengthening or softening in this nanocomposite material systems is a function of GB/nanodomain wall thickness, particle placement, grain/nanodomain size, and temperature.

Walker et al. (2011) exploited spark plasma sintering to fabricate silicon nitride–graphene nanocomposites. With homogeneously dispersed graphene sheets having thickness of 2 nm or lower ($\approx$ 3–4 carbon atomic layers), the nanocomposite exhibited remarkable mechanical characteristics. In particular, a silicon nitride nanocomposite containing 1.5 vol% graphene inclusions shows $\approx 235\%$ increase in the fracture toughness (from $\approx$ 2.8 to $\approx$ 6.6 MPa$\sqrt{\mathrm{m}}$), when compared with monolithic Si_3N_4 material. From a micromechanical viewpoint, toughening of the nanocomposite occurs through crack deflection, crack bridging by graphene sheets, their pull–out and necking.

Pavia and Curtin (2011, 2013) studied the effect of interface in the nanocomposite made of carbon nanotube reinforced in a diamond carbon matrix using explicit atomistic or MD simulations. They investigated how annular crack in matrix impinging on interface behaves as a function of the degree of interface strength and interface sliding

resistance which is controlled by the density of C interstitial atoms. Under all interface conditions studied, incident matrix cracks do not penetrate into the nanotube. Under increased loading, "weak" interfaces fail in shear followed by interfacial sliding, leading to "tough" materials. "Strong" interfaces do not debond, and instead the CNT fails, leading to a "brittle" low-toughness material. In addition, they showed that the transition between "weak" and "strong" interfaces, and hence "tough" and "brittle" composite behavior, is not governed by the interface and nanofiber fracture energies, as predicted by the He–Hutchinson analysis (He and Hutchinson, 1989a,b). On the contrary, the researchers showed that the transition is determined by their fracture strengths (interface shear strength and nanofiber tensile strength).

These active researches on the ceramic matrix nanocomposites (CMNC) have considered reinforcements in the form of particles, fibers or nanotubes. Though it has been claimed that composites made with such nanoscale reinforcing materials as nanotubes, graphene and nanofibers would have exceptional properties, results to date have been disappointing compared to the mechanical performance showed by the biological nanocomposite materials (Dzenis, 2008; Launey and Ritchie, 2009; Ji and Gao, 2010).

The applicability and transferability of design strategies found in biological materials to ceramic based composites remain an unresolved question, partly because the deformation and failure mechanisms and the relationships between the structure and properties have not yet been understood. Specifically, the wide parameter space associated with different platelet shapes and orientations has not been explored in the literature. Therefore, studies focusing on ceramic matrix reinforced with staggered nanoplatelets inspired from biological materials have been carried out in this thesis; results obtained from these studies could provide guidelines in improving the mechanical performance of ceramic matrix composites. In the present work, basic strategies of biological materials, such as (i) the staggered arrangements of platelets in the matrix, (ii) nanometer size of constituents, (iii) compliant matrix (though not polymeric as in actual biological materials) and (iv) the modulus ratio (though much smaller compared to the biological composites), are utilized for the development of bio-inspired composites with ceramic constituents. Here, the generic mechanical behavior of bio-inspired ceramic nanocomposites is studied by incorporating the basic mechanical character of ceramics materials (i.e., brittleness) instead of a specific ceramic material. The design

guidelines required for the design of synthetic brittle matrix nanocomposites with superior mechanical properties could be gained from this study.

1.5 Objectives, Approach and Scope of the Work

The objective is to analyze the mechanical behavior of bio-inspired brittle matrix nanocomposites. The objective is also to investigate the differences and similarities in the mechanical behavior of the regularly staggered and stair-wise staggered arrangements of hard platelets reinforced in a soft matrix. Both the constituents, i.e., the matrix and platelets, are considered as brittle in nature. Atomistic simulations are undertaken to find the mechanical behavior of these materials. In order to study the generic principles applicable to all ceramic materials, the constituents are idealized as "model materials" which has a brittle nature. The "model material" is a concept widely used in atomistic simulations where the generic properties common to a large class of materials, such as brittleness or ductility, are incorporated rather than studying the behavior of specific materials.

In this thesis, the mechanical properties at the nanoscale are studied using atomistic simulations. These methods are outlined in greater detail in Chapter 2. Further the basic deformation mechanisms of regularly and stair-wise staggered brittle-matrix nanocomposites are examined in Chapter 3. Here, the results of two-dimensional atomic system are compared with the three dimensional simulation and the results of other nanocomposites available in the literature. Using MD methodology, mechanical behavior of atomic systems can only be studied at very high strain rates. Therefore, the effect of strain rate is analyzed in Chapter 4 and an optimum strain-rate is chosen which is used in other simulations carried out in the thesis. Further, the effect of aspect ratio on load transfer and failure mechanisms is investigated in Chapter 5. Thereafter, the interface strength is varied by controlled the interaction parameter between the matrix and platelet atoms and effect of this variation on the overall mechanical behavior of the bio-inspired nanocomposites is studied in Chapter 6. Thereafter, the effect of length scale is analyzed in Chapter 7. Finally in Chapter 8, summary of the thesis and outlook for future directions are discussed.

CHAPTER 2

Simulation Methodology

In the study of mechanical properties of nanoscale structures, the influence of individual atoms needs to be considered. The atomic simulations yield important information about the materials deformation. Further, the deformation mechanisms which cause the high strength and toughness in nanoscale materials can be captured through these atomistic simulations. New information that are unattainable by experimental procedures and unpredictable by continuum theories can be obtained through these simulations. In this chapter, the simulation method used in the thesis is explained. This mainly constitute steps involved in molecular dynamics, measurement of mechanical properties and visualization techniques.

2.1 Introduction

Computational simulations play a major role in elucidating the fundamental materials behavior that are not possible with physical experiments. Nowadays, many researchers consider the computer as a tool to do science, similar to experimentalists using their labs to perform experiments. Therefore, computer simulations have been referred to as "computer experiments" or "computational experiments" (Buehler, 2008). The computational experiments are not only useful in validating theories, but also inspire new experimental methods. Moreover, the computational simulations also inspire formulation of new theoretical frameworks for understanding simulation results. A certain simulation method is chosen based on several factors, such as the length scale of the simulated specimen and the type of information required. Different simulation methods exist to study the mechanical behavior of materials (Raabe, 1998; Tadmor and Miller, 2011). These simulation methods can be categorized such as i) Continuum based methods (Rappaz et al., 2010), such as Finite Element Method–FEM (Zienkiewicz and Taylor, 1989) and Finite Difference Method–FDM (Carnahan et al., 1969), ii) Discrete models, such as Molecular dynamics–MD (Rapaport, 2004) and Random Fuse Models–RFM (de Arcangelis et al., 1985), and iii) Multi-scale simulation methods, which in-

clude hierarchical methods and concurrent methods such as MAAD, and quasicontinuum methods (Miller and Tadmor, 2002; Liu et al., 2004).

In this thesis, the focus is on the mechanical behavior of nanoscale composites where the continuum description of materials is questionable and the atomistic information of the model is often needed. Therefore, we consider atomistic simulations which are also known as molecular dynamics (MD) simulations. The MD simulations are further broadly divided into ab-initio MD and classical MD methods. The ab-initio MD techniques are constructed on the basis of an accurate solution of Schrödinger wave equation which require information about electronic states of individual atoms. There are also some tailored and combined methods, such as tight binding molecular dynamics (TBMD) and density functional theory (DFT) approaches, which require an extreme amount of intensive computation (Lu and Bhattacharya, 2005). These methods yield accurate results. However, due to the large number of calculations involved, the number of atoms that can be simulated in ab-initio MD simulations is limited to a few hundreds of atoms (typically < 1000), which is not large enough to simulate important problems in materials deformation and failure (Buehler, 2008; Tadmor and Miller, 2011). In contrast, the classical MD method uses empirical or semi-empirical interatomic force fields that approximate the inter-atomic force obtained from quantum mechanical calculations. In the classical molecular dynamics simulations, the quantum information of atoms is lost, but large systems with even a few millions of atoms can be simulated using this method (Buehler, 2008; Tadmor and Miller, 2011). This classical MD has been extensively used to investigate the mechanical behavior of nanoscale crystalline materials like nano-wires and nanocrystalline materials (Ashurst and Hoover, 1976; Koh et al., 2005; Park and Zimmerman, 2005; Schiøtz et al., 1999), nanoscale polymeric materials (Tsige and Stevens, 2004), amorphous materials like metallic and polymeric glasses (Maloney and Lemaître, 2004; Rottler and Robbins, 2003) and nanocomposites (Cho and Sun, 2007; Sahu and Anup, 2016). These studies have helped in understanding and expanding our knowledge on the deformation physics of these nanoscale materials. In our study as well, we use classical MD simulations to understand the deformation behavior of nanocomposites.

2.2 Classical Molecular Dynamics

Classical molecular dynamics is the simplest tool for atomistic studies which predicts the motion of a large number of atoms governed by their mutual interaction. Here, the complex structure of an atom is approximated by a point particle and the quantum mechanical interatomic force is approximated by an empirical interatomic force (Buehler, 2008; Rapaport, 2004). Various steps involved in carrying out a general atomistic tensile test simulation using classical molecular dynamics are shown in Fig 2.1. These steps can be grouped into phases such as: 1) Initialisation phase where initial position and velocity of each atom as well as interatomic potentials are specified, 2) Proper simulation settings such as temperature control and pressure control are given, 3) Solution phase: this phase can be further divided into equilibrium phase and production phase. The equilibrium phase is carried out to obtain the stress-free, stable, initial microstructure of the sample. Thereafter, the lower and upper walls are defined in the model. The upper wall is moved in a constant velocity and lower wall is kept fixed. Moreover, a initial velocity gradient is given in the model from lower to upper walls to avoid shock wave generation from the walls. During the production phase, classical MD uses Newton's equations of motion to calculate the position and velocity on each atom at every time-step in a given atomistic geometry. 4) Post-processing phase where the stress and strain at each time-step are calculated using the positions, velocities, and forces of every atom, along with the concepts from statistical mechanics. The stress and strain are further used to find out other mechanical properties. Further, visual analyses are conducted to obtain the deformation mechanisms occurring in the samples. In the following sections, all the steps involved in our simulations are explained in detail.

Though the classical MD simulations have been extensively used in understanding the atomic level mechanisms of materials, they suffer by two main disadvantages. Before going through the detailed explaination of MD simulation methodology used in the thesis, the disadvantages of MD are briefly explained here. 1) MD simulations solves the equation of motion numerically for all atoms to predict their position at time $(t+\Delta t)$, where Δt is the MD time-step. The calculation of position of all atoms is repeated to find out the trajectory of all atoms till the process under investigation is completed; the number of iterations is the number of time-steps. To maintain accuracy, Δt is typically

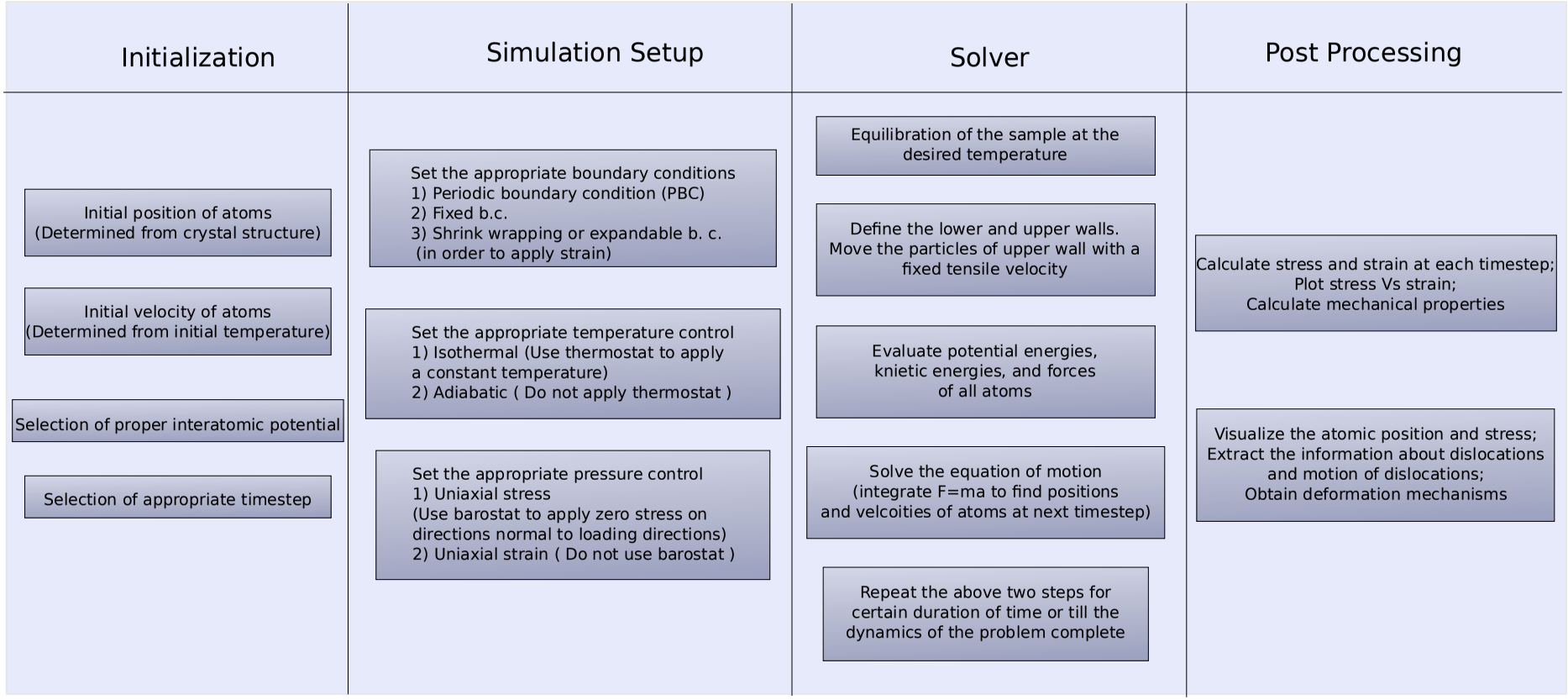

Figure 2.1 Steps involved in the simulation of computational tensile test using classical molecular dynamics.

of the order of one to a few femtoseconds (1 fs = $10^{-15}s$). In atomistic simulation using classical MD, the number of time-steps that can be accomplished within a reasonable CPU time is typically in the range $10^5 - 10^7$, so that the total simulated time is of the order of nanoseconds (1 ns = $10^{-9}s$). 2) Further, the dominant computational task in a MD simulation is to evaluate the forces acting on each atom at each timestep. If we assume the simulated system has a nearly uniform atom density, then each atom interacts with a small, roughly constant number of neighbors. This means the computational effort per timestep scales linearly as N, the number of atoms simulated. Thus on a parallel machine with P processors, the best a parallel algorithm for short-range MD can scale is as N/P. In order to complete the simulation in a reasonable time with the current available computer resource, the total number of atoms to be considered is limited to in the order of nanometers (1 nm = $10^{-9}m$). Thus, the spatial and time scales of the model that can be analyzed in classical MD simulations are in nanoscale. These restrictions lead to much higher strain-rate in MD simulations compared to experiment. Most studies in the literature have used strain-rate in the range of $10^6 - 10^9 s^{-1}$. These values are more than 10 orders of magnitude larger than the typical strain rate of $10^{-4}s^{-1}$ applied to macroscopic tensile specimens in laboratory tests. However, the MD simulations have provided valuable information regarding fundamental mechanisms of materials. Moreover, a separate study has been carried out to investigate the effect of strain rate on the MD simulations (refer Chapter 4) and optimal strain rate is chosen for analyzing structural and material parameters.

2.2.1 Interatomic Potentials and Force Fields

Definition of the atomic interactions by force fields is at the heart of MD methods, as it defines the complete materials behavior. The expression for the potential energy is used to determine the forces and accelerations used in solving Newton's equations of motions. Different types of interatomic potentials exist. They can be categorized into potentials developed for crystalline solids such as metals and ceramicis, and potentials developed for polymeric solids such as organic materials. The potentials for polymeric systems can be grouped into non-reactive potentials (such as CHARMM) and reactive potentials (such as ReaxFF). As our main focus is on the crystalline ceramic materials,

the potentials for crystalline materials are discussed further. The potentials developed for crystalline systems are divided into pair potentials and multi-body potentials. In pair potentials, the total potential energy of the system is expressed as the sum over all pairs of bonds. In multi-body potentials, the strength of the pair wise interactions are modulated dependent on the atomic environment. Examples for pair potentials are the Lennard-Jones (LJ) potential and the Morse function. Examples for popular multi-body potentials are the Tersoff potential and the Stillinger-Weber potential to model covalent interactions, or the embedded atom method (EAM) and modified embedded atom method (MEAM) potentials suitable for metals. In generating model materials with crystalline solids, the typically used "model potential" is the Lennard-Jones (LJ) potential (Abraham, 2001; Abraham et al., 2002b; Buehler et al., 2004; Buehler, 2008) which is discussed further in detail. In contrast, other potentials can be used for studying specific materials behaviour.

LJ potential provides the fundamental description of the generic features of inter-atomic interaction: repulsion at close distances and attraction at large distances of separation. LJ potential has been extensively used in studying the mechanical behavior, fracture and failure of materials. Moreover, LJ potential allows the design of "model materials" to study materials behavior which is applicable to large class of materials (Abraham, 2001; Abraham et al., 2002a,b; Buehler et al., 2003, 2004; Buehler, 2008; Holian et al., 1991). Further, the intent of thesis is to study generic behavior of nanocomposites made up of ceramic constituents. Therefore the LJ potential serves the purpose. Moreover, physical behavior determined by simple pair-potentials like LJ are reported to reproduce results qualitatively very similar to that obtained using computationally costlier potentials such as EAM (Wang et al., 1996; Munilla et al., 2009; Ziegenhain et al., 2009). Therefore, LJ potential is very useful in parametric and sensitivity studies. In the present study, the LJ potential is used together with a two-dimensional (2D) hexagonal lattice which captures the generic brittle behavior of the materials (though 3D fcc lattice with LJ potential is essentially ductile)(Abraham, 1996; Chang et al., 2013). Although 2D models are over-simplification of the real systems, they could reveal the information regarding fundamental mechanisms occurring in the model (Baimova and Dmitriev, 2011; Weingarten and Selinger, 2007). Moreover, the two-dimensional systems are also computationally efficient compared to 3D models. In

2D simulations, atoms in one planar region are considered and the strains perpendicular to the plane are ignored. This assumption is similar to the plane strain condition in 2D continuum models. As the study of variation of mechanical behavior with changes in geometrical parameters, material properties and loading rates is the main objective of our simulation; the 2D models could be very efficient.

In our molecular dynamics simulations, the atoms are represented as classical particles without any bonds among them. Initially, atoms are located in the lattice points of the hexagonal lattice structure. We use a modified LJ potential to define the force-field between the atoms. The LJ potential is given by Eq (2.1), where σ_{LJ} & ϵ_{LJ} are the LJ parameters. The value of σ_{LJ} controls the lattice parameter and the value of ϵ_{LJ} is directly proportional to the elastic modulus and strength of the LJ solid (Buehler, 2008). A modified LJ potential function used in our simulations is shown in Eq (2.2) (Ziegenhain et al., 2009). The modified LJ potential is created by adding a smooth cut-off function to Eq (2.1) as defined by Voter (1993) with $m = 20$. This cut-off function makes the values of potential energy and its derivative (inter-atomic force) to approach zero smoothly at the cut-off radius. The cut-off radius is chosen from Holian et al. (1991) in order to make the results consistent with the other results in literature.

$$\phi_{LJ}(r) = 4\epsilon_{LJ}\left[\left(\frac{\sigma_{LJ}}{r}\right)^{12} - \left(\frac{\sigma_{LJ}}{r}\right)^{6}\right] \tag{2.1}$$

$$\phi(r) = \phi_{LJ}(r) - \phi_{LJ}(r_{cut}) + \phi'_{LJ}(r_{cut})\frac{r_{cut}}{m}\left[1 - \left(\frac{r}{r_{cut}}\right)^{m}\right] \tag{2.2}$$

2.2.2 Reduced LJ Units

In all the simulations, LJ units are used; this unit system is sometimes also referred to as dimensionless or reduced units. In the LJ unit systems, lengths are scaled by σ_{LJ}, energies are scaled by ϵ_{LJ}, masses are scaled by the mass of an atom (m_a), and Boltzmann constant (K_b) is kept as unity (Rapaport, 2004; LAMMPS Documentation, 2015). Once certain units are altered, other units must be altered correspondingly to make the algebraic expressions of physical laws look invariant. For example, $K = mv^2/2$ in the SI system, and it should still hold in the LJ unit system. This can only be achieved if the derived time (τ) unit satisfies; $\epsilon_{LJ} = m_a\sigma_{LJ}^2/\tau^2$ OR $\tau = \sqrt{m_a\sigma_{LJ}^2/\epsilon_{LJ}}$. Thus in LJ units,

time should be scaled by $\sqrt{m_a \sigma_{LJ}^2 / \epsilon_{LJ}}$ to obtain reduced time in LJ unit. Moreover, to have some rough idea about our MD inputs and results in SI unit systems, we assume the following typical values: $\sigma_{LJ} = 10^{-10}$m, $\epsilon_{LJ} = 10^{-21}$J, and $m_a = 10^{-25}$Kg; this leads to reduced time equivalent to 1 picosecond (1ps = 10^{-12}s). Further, MD timestep of 0.001 (in reduced time) and a strain rate of 10^{-5} (in strain per reduced time) are used in our computational tenslie test simulations; these are equivalent to approximately 1fs and $10^7 s^{-1}$ respectively in SI units. These dimensionless LJ units simplify the numerical calculation by converting all the numerical values close to unity from extremely small values associated with the atomic scale. Use of dimensionless units also serves the purpose of generating the "model material" which means that a single potential can describe a whole class of materials. In order to obtain the generic mechanical behavior of the nanocomposite model, the different mechanical behavior of the constituents, such as platelets (stiff, brittle and strong) and matrix (compliant, brittle and weak), are incorporated by varying the parameter (ϵ_{LJ}) which controls the stiffness and strength. However, the lattice parameter (σ_{LJ}) is kept equal to unity for both constituents in order to maintain the stable equilibrium structure. Typical values of LJ parameters used for different constituents are shown in Table 2.1. The mechanical properties of constituents calculated using MD simulations are also given in the table (calculation of mechanical properties from MD simulations are explained in the next section).

LJ parameters	Modulus	Strength	Failure strain	Tensile Toughness
Platelet ($\sigma_{LJ} = 1$,$\epsilon_{LJ} = 1$)	$E_p = 66$ $G_p = 24.8$	$\sigma^p_{crit} = 4.3$ $\tau^p_{crit} = 1.5$	$\varepsilon^p_{crit} = 0.12$ $\gamma^p_{crit} = 0.06$	0.372
Matrix ($\sigma_{LJ} = 1$,$\epsilon_{LJ} = 0.1$)	$E_m = 6.6$ $G_m = 2.48$	$\sigma^m_{crit} = 0.43$ $\tau^m_{crit} = 0.15$	$\varepsilon^m_{crit} = 0.12$ $\gamma^m_{crit} = 0.06$	0.0374
Interface ($\sigma_{LJ} = 1$,$\epsilon_{LJ} = 0.1$)	$E_i = 6.6$ $G_i = 2.48$	$\sigma^i_{crit} = 0.43$ $\tau^i_{crit} = 0.15$	$\varepsilon^i_{crit} = 0.12$ $\gamma^i_{crit} = 0.06$	0.0374

Table 2.1 The different LJ parameters assigned to different constituents, and the mechanical properties of different constituents calculated using MD simulations for 2D LJ solid are listed. All the quantities are expressed in dimensionless (reduced), LJ units.

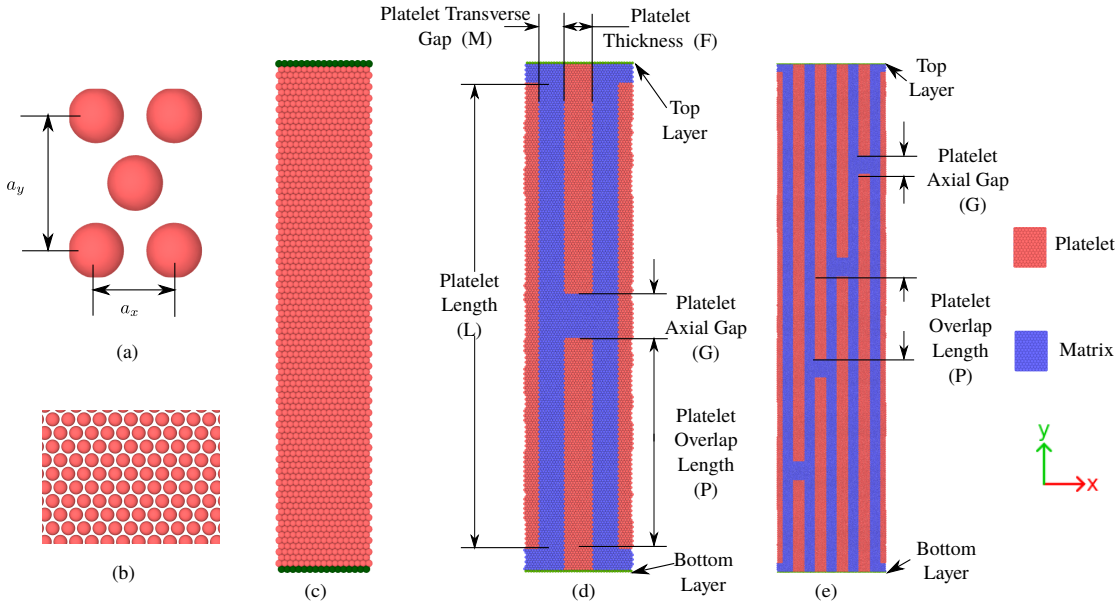

Figure 2.2 Details of the simulated model. (a) unit cell of 2D hexagonal lattice (b) 2D hexagonal lattice structure, (c) homogeneous solid, (d) RVE of regularly staggered model (RSM, sometimes referred to as N2-SSM), and (e) RVE of stair-wise staggered model (SSM, sometimes referred to as N5-SSM).

2.2.3 Atomistic Geometry

The property of material is included in the model through interatomic potential as explained in the previous section. This section explains the all-atom geometry of the model. The unit cell of the 2D hexagonal lattice structure used to create the atomistic geometry is shown in Fig 2.2a. This unit cell of the hexagonal lattice is of rectangular shape with 2 lattice points, one atom at the center of the lattice and one-fourth of an atom at each corner. Further, the unit cell is defined by the translation vectors $\vec{a_x} = \sqrt[6]{2}\,\sigma_{LJ}\,\vec{i}$ and $\vec{a_y} = \sqrt{3}\sqrt[6]{2}\,\sigma_{LJ}\,\vec{j}$, where $\vec{i}$ and $\vec{j}$ refers to the unit vectors in the X and Y directions. The length of these vectors corresponds to the equilibrium lattice constants for the defined LJ potential. The hexagonal lattice structure is shown in Fig 2.2b. Moreover, the homogeneous model is shown in Fig 2.2c. Here, the unreinforced uniform material which is made up of only one type of atoms is referred to as a homogeneous material. Further, using this hexagonal lattice structure, the staggered models of nanocomposites are built and shown in Fig 2.2d & Fig 2.2e, which are regularly staggered model (RSM) and stair-wise staggered model (SSM) respectively. It is to be noted here that the purpose of the thesis is to analyze the mechanical behavior of RSM and SSM models which

are inspired from the biological nanocomposite materials. In these models, the platelet thickness (F) has 10 atoms and similarly, the platelet transverse gap or matrix thickness (M) has 10 unit cells in X direction ($F = M = 10a_x$ which is equal to $10\sqrt[6]{2}\sigma_{LJ}$). The platelet axial gap is built with 10 unit cells in Y direction ($G = 10a_y$ which is equal to $10\sqrt{3}\sqrt[6]{2}\sigma_{LJ}$). Further, the platelet length (L) is kept as 100 unit cells for RSM and 260 unit cells for SSM models. However, the platelet length is varied during the study of the effect of aspect ratio ($AR = L/F$) of platelets which is done in Chapter 5. Similarly, the total number of atoms is scaled proportionately during the study of length scale effect carried out in Chapter 7. Further, the platelet overlap length (P) depends on the platelet length (L) and axial gap (G) as shown in the Eq (2.3),

$$P = \frac{L - (N_p - 1) \times G}{N_p} \tag{2.3}$$

so that the platelet arrangement periodically repeat in X directions after N_p number of platelets ($N_p = 2$ for regularly staggered model and $N_p = 5$ for stair-wise staggered model). Moreover, one row of atoms at both the bottom and top of the nanocomposite model are used to apply uni-axial strain. These atoms are named bottom and top layer. Computational uniaxial tensile tests are performed on these atomistic geometries; in the following section, steps involved in computational experiments are discussed in detail.

2.2.4 Computational Experiment

In order to investigate the mechanical behavior of nanocomposite models, computational uniaxial tensile tests are performed. In all the simulations, strain is applied along the length of the platelets (here it is vertical or Y-direction) and the stresses normal to the loading directions (here it is horizontal or X-direction) are maintained zero. Further, shrink-wrapped boundary condition is maintained in the Y-direction, which means that vertical length of the simulation box is permitted to shrink or expand; therefore, the tensile test can be done in the vertical direction. Moreover, periodic boundary condition is maintained in the X-direction. Before applying uniaxial tensile stress in the system, the model is equilibrated at constant temperature (T) of 0.0001 (in reduced units) to get stress-free initial structure. NVT ensemble is used in the equilibration phase of the simulation. During uniaxial tensile loading simulation, a constant strain-rate ($\dot{\varepsilon}_{yy}$) is

applied to the model by setting a constant value of y-velocity to the atoms in top layer (V_{yy}) and y-velocity of zero to the atoms in bottom layer of the model. The velocities of atoms at the boundaries are different from the internal atoms, which could induce a shock. In order to avoid this shock wave generation from the boundary, an initial linear velocity gradient is established from the lower layer to upper layer (Abraham et al., 1997; Horstemeyer et al., 2003). Ideally, the strain-rate (SR) given in MD simulations should be low enough to be close to that of the practical situation. However, this may lead to a very high computational cost. Therefore, a separate study is done to analyze the influence of strain-rate on the model nanocomposite and an optimal strain rate of 10^{-5} is chosen for our further analysis which is separately discussed in Chapter 4. During tensile loading, Berendsen thermostat (Berendsen et al., 1984) is used to keep the temperature at a constant value of 0.0001 and Berendsen barostat (Berendsen et al., 1984) is used to maintain a zero stress normal to the loading direction. Thus, isothermal uniaxial tensile stress condition which is required for simulating the tensile test is established computationally. After the initial positions and velocities of atoms in the model are given as input, the resulting trajectories of atoms are calculated based on Newton's equations of motion for every time-step (Δt) of 0.001 in reduced time unit (this is approximately equivalent to 1 fs in SI unit, refer Section 2.2.2). A constant strain-rate ($\dot{\varepsilon}_{yy} = 10^{-5}$ in reduced units; this is approximately equal to $10^{7} s^{-1}$ in SI unit, refer Section 2.2.2) is applied until the model completely breaks into two pieces. To understand the mechanical behavior, the mechanical properties such as stiffness, strength and toughness are calculated and the variations of these mechanical properties are explored. In the next section, the way in which the mechanical properties are obtained from MD simulations is explained.

2.3 Mechanical Behavior of Atomistic Systems

The typical mechanical behavior of atomistic solids subjected to uniaxial tensile test simulations can be understood from stress-strain diagram as well as the visual analysis of deformation mechanisms. The applied strain (ε_{yy}) at each time-step is given by Eq (2.4). At every time-step, the value of stress is calculated using the interatomic force term of virial formula (Zhou, 2003), shown in Eq (2.5), where $F_y^{\alpha\beta}$ is the y-component

of force acting between atom α and atom β, and $r_y^{\alpha\beta}$ is the y-component of distance between atom α and atom β. The values for α and β run through every atom in the model.

$$\varepsilon_{yy} = \dot{\varepsilon_{yy}}\Delta t = \frac{V_{yy}\Delta t}{L_0} \tag{2.4}$$

$$\sigma_{yy} = \frac{1}{2}\frac{1}{V}\sum_{\alpha}^{N_a}\sum_{\beta\neq\alpha}^{N_a} F_y^{\alpha\beta} r_y^{\alpha\beta} \tag{2.5}$$

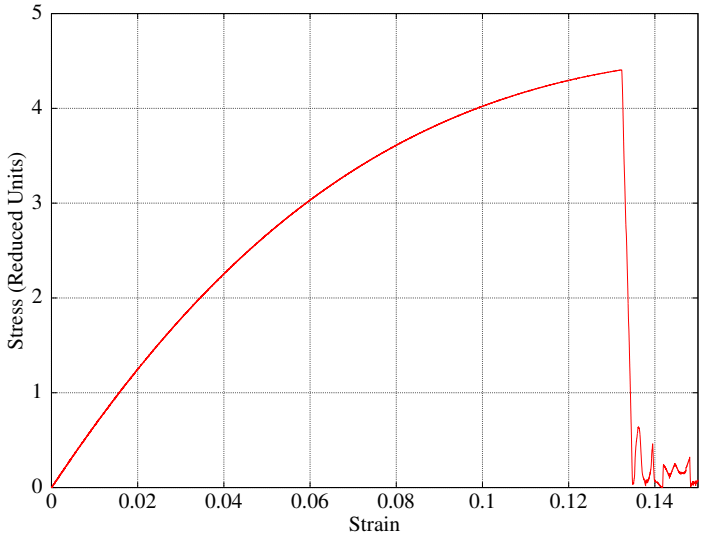

Figure 2.3 Stress-strain diagram obtained from MD simulation for the homogeneous 2D LJ solid under uniaxial tensile test ($\sigma_{LJ} = 1$ and $\epsilon_{LJ} = 1$).

The stress-strain diagrams for homogeneous LJ solid and a typical nanocomposite LJ solid are shown in the Figs 2.3 and 2.4. The homogeneous model shows a non-linear stress-strain relation and matches with the results available in literature (Buehler, 2008) which indicates the validity of our MD simulation procedures. Whereas, nanocomposite model initially shows a linear stress-strain relationship and later fluctuates. Similar trend is also found in the biomorphic 3D nanocomposite models studied by Broedling et al. (2008).

2.3.1 Calculation of Mechanical Properties

The calculation of typical mechanical properties is explained here with the aid of Fig 2.5. The Young's modulus is the slope of the stress-strain diagram at the origin. Critical

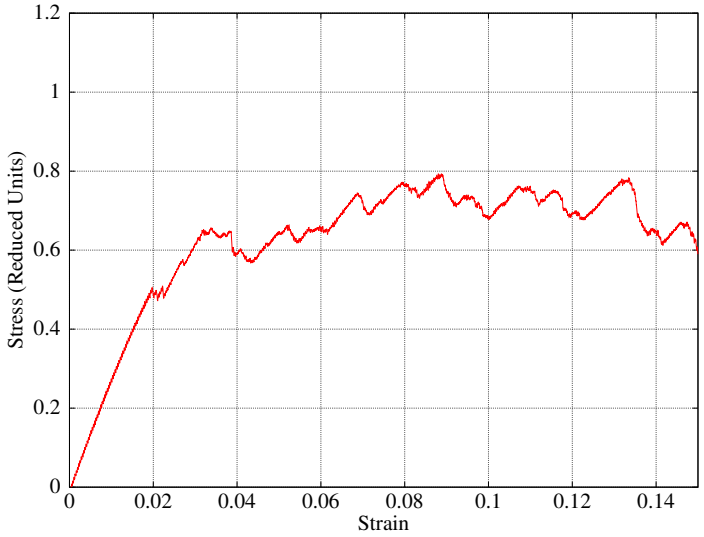

Figure 2.4 Stress-strain diagram obtained from MD simulations for a typical nanocomposite model under uniaxial tensile test (RSM model).

stress is taken as the maximum stress observed during the tensile test.

Further, the yield and flow stresses widely used in characterizing the mechanical properties of materials are explained briefly. The yield stress is defined differently by different authors in the literature depending on materials stress-strain behavior; such as upper yield stress, lower yield stress and offset yield stress. In our MD simulations, the yield stress is taken as stress at which first dislocation nucleates from the platelet tips (as discussed in the visual analysis of deformation behaviour in the following chapters); this corresponds to the first drop in the stress observed in the stress-strain diagram.

Flow stress is generally defined as the stress at which the material undergoes flow i.e., strain increases at a constant stress. In MD simulations, the flow stress is defined as the stress required for a significant amount of dislocation activities to occur in the model (Schiøtz et al., 1999; Schiøtz and Jacobsen, 2003; Broedling et al., 2008; Li et al., 2010); it is calculated as the average value of stress in the strain range of 8% to 10% of plateau region of the stress-strain curve. This strain range is chosen because the visual analyses of deformation behavior of our models (discussed in the following chapters) show occurrence of significant amount of dislocation activities in this strain range. However, considerable care should be taken in identifying the strain range; because, proper strain range needs be chosen such that the flow behavior is indeed observed on the chosen strains.

Toughness of the nanocomposite models is calculated from the area under the stress-

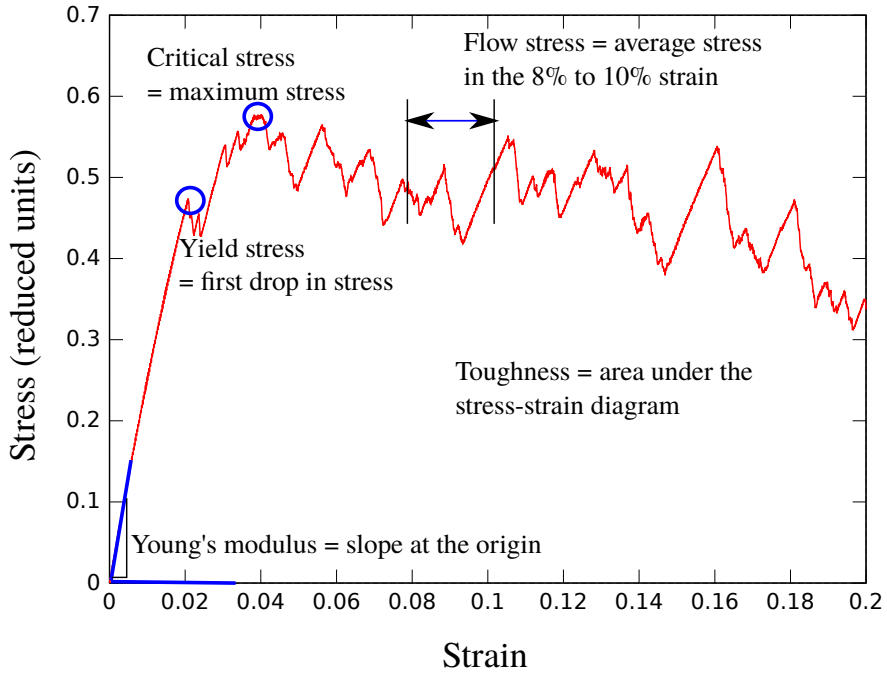

Figure 2.5 Calculation of mechanical properties from a typical stress-stain diagram of a nanocomposite.

strain diagram. It is to be noted here that the area under the stress-strain diagram is often taken as a measure of toughness of materials and is known as “tensile toughness” (Meyers and Chawla, 2009). Though this is a qualitative method to calculate the toughness of a material, it is a popularly used parameter to study materials behavior. In contrast, new quantitative methods, developed based on fracture mechanics, accurately measure the toughness of materials; many parameters are developed to study toughness of material quantitatively, such as critical stress intensity factors (K), critical crack extension force (G), critical crack tip opening displacements (CTOD) and so on (Anderson, 1995; Meyers and Chawla, 2009). In this thesis, the toughness is taken as the area under the stress-strain diagram up to the strain of 20%. As the value of tensile toughness itself is a qualitative measure of toughness of materials, by taking the area of stress-strain diagram up to the strain value of 20%; a huge amount of computational time can be saved in the MD simulation. Further, valuable insights about the behavior of materials can be obtained using the tensile toughness of materials, similar to that of impact toughness, which is still in practice to study the toughness of nuclear materials (Meyers and Chawla, 2009).

Before beginning the study of the overall mechanical behavior of the nanocomposite models, the material properties of constituents need to be calculated. The mechan-

ical properties of constituents are required in order to analytically predict the overall nanocomposite mechanical properties. Homogeneous constituent material is subjected to uni-axial tensile test and mechanical properties are calculated as explained previously. Table 2.1 shows the calculated mechanical properties for all the constituents. These values are consistent with the available data in the previous studies of 2D LJ solids (Abraham et al., 1997; Abraham, 1996) as well as theoretical predictions using the *"atomistic elasticity"* concepts (Buehler, 2008). From the theory of *"atomistic elasticity"*, the LJ parameters and the modulii of the 2D hexagonal LJ solid is related by Eq (2.6). These relations lead to the value of 66 and 24.8 (in reduced units) for Young's modulus and shear modulus for LJ parameters values of $\sigma_{LJ} = \epsilon_{LJ} = 1$ (Buehler, 2008). The MD results agree with the values predicted by atomistic elasticity, which indicates the validity of our MD methods. From the Table 2.1, it is seen that the modulus and strength of the LJ solids are directly proportional to the ϵ_{LJ} value of the material while the failure strains remain a constant. Thus, the platelet has higher stiffness and strength compared to the matrix, while the failure strain is the same for both the constituents.

$$E = \frac{2}{\sqrt{3}}k \qquad G = \frac{\sqrt{3}}{4}k \qquad \text{where } k = \frac{72}{\sqrt[3]{2}}\frac{\epsilon_{LJ}}{\sigma_{LJ}^2} \tag{2.6}$$

2.3.2 Visualization

In this section, the visualization of the resulting atomic data is explained. The raw data from MD simulations are positions, velocities, energies, forces, pressure and temperature at every time-step for each atom. From this huge amount of data, the calculation of equivalent continuum mechanical properties is explained previously. However, it is also useful to analyze the evolution of defects in the crystal structures. Understanding the evolution of crystal defects is an essential requirement for interpreting the simulated atomic scale processes, so that scientific insights into the physical system can be obtained (Buehler, 2008; Stukowski, 2010).

To visualize the lattice defects, several methods are available. However, the centrosymmetry parameter (CSP) is a common tool used for visualization of defects in simple crystals. According to Kelchner et al. (1998), the centrosymmetry parameter for

each atom of an hexagonal crystal structure is defined as:

$$CSP = \sum_{i=1,3} |\vec{R_i} + \vec{R_{i+3}}|^2 \tag{2.7}$$

where $\vec{R_i}$ and $\vec{R_{i+3}}$ are the vectors corresponding to the three pairs of opposite nearest neighbors in the hexagonal lattice system considered. In this method, the atoms with CSP values greater than 0.01 are considered as a defect.

Thus, both the mechanical properties calculated from stress-strain diagrams and the visual analysis of deformation mechanisms are used to completely understand the mechanical behavior of these nanocomposite materials. Specifically, the method outlined in this section is used to study the influence of various loading-rates, geometrical parameters, and material parameters on the overall mechanical properties of bio-inspired nanocomposites.

2.4 Summary of Tools Used

Open source MD software, LAMMPS (Plimpton, 1995), is used to model and solve the equations of motion of atoms. MD simulations are carried out in a high performance cluster with 10 dual-quad-core processors. And, in order to visualize the atomic crystal structures and defects generated in them, Open source visualization tool (OVITO) (Stukowski, 2010) is used. The work is completely accomplished with the following tools which are freely available, i.e., open source software.

1. Molecular Dynamic Simulator: LAMMPS
2. Visualization tool: OVITO
3. Dislocation Extraction Algorithm: dxa.ovito.org

Further, in this work, other free software packages such as GNU Octave and Inkscape are used for the creation of graphs and schematic illustrations.

CHAPTER 3

Basic Deformation Mechanisms

Biological materials with nanostructure of regularly staggered or stair-wise staggered arrangements of hard nano-sized platelets reinforced in a soft matrix have superior mechanical properties. Applications of these arrangements of platelets in ceramic matrix could enhance the toughness of ceramic matrix nanocomposites. Molecular dynamics simulations are performed to study the basic mechanical performance of the regularly staggered model (RSM) and stair-wise staggered model (SSM). RSM shows better flow behavior compared to SSM due to the symmetrical crack propagation along the interface in RSM. Though higher stiffness and strength are obtained for SSM, rapid crack propagation reduces the toughness. Arresting this crack propagation could lead to superior mechanical properties in SSMs.

3.1 Introduction

Platelet reinforced unidirectional nanocomposites, inspired from the nanostructure of biological materials such as nacre and bone (Anup et al., 2010), have potential applications in fabricating advanced synthetic ceramic composites (Sakhavand and Shahsavari, 2015). In order to study the ceramic matrix nanocomposites, models are developed in this thesis, which were discussed in Chapter 1 and Chapter 2. The main deformation mechanisms responsible for plasticity and toughness in the bio-inspired generic brittle-matrix nanocomposite models are analyzed in this chapter.

In general deformation in crystalline materials at room temperature can be divided into elastic and plastic deformation (Dieter, 1988; Meyers and Chawla, 2009). Materials undergo deformation when external loads are applied to it. If the material comes back to its original size and shape when it is unloaded, the deformation is said to be elastic. If the material does not come back to its original size and shape, it has undergone plastic deformation. Moreover, the mechanisms responsible for the plastic deformation in crystalline materials belong to two categories: (i) partial and full dislocations, (i.e.,

slip) and (ii) deformation twinning (Dieter, 1988; Meyers and Chawla, 2009). It is well known that grain boundaries, surfaces, and heterophase interfaces are potential sources for dislocations (Mara and Beyerlein, 2014). For coarse-grained crystals, the grain interiors also contain plenty of sources as well as copious room for them to operate. For nanocrystalline (NC) and ultrafine-grained (UFG) bulk materials, conventional lattice slip is hampered by large amounts of grain boundaries(GBs) or interfaces, in which case plastic flow often occurs through alternative deformation modes mediated by GBs (Yamakov et al., 2002; a.G. Frøseth et al., 2004; Koch et al., 2007; Greer and De Hosson, 2011). However, little work has been done regarding the deformation mechanisms in ceramic-ceramic nanocomposite materials.

A few nanocomposite systems that were investigated previously are discussed here. Ahmad et al. (2010) experimentally studied the homogeneously dispersed carbon nanotubes reinforced alumina (Al_2O_3/CNT) fabricated by hot-pressing. A significant improvement of 94% in fracture toughness at 4 vol.% CNT concentration has been obtained, which slightly decreased to 66% when CNT content was increased to 10 vol.%. It is believed that both the conventional fracture toughening mechanisms (pull-out and crack bridging) and CNT energy dissipation mechanism via elastic deformation played significant roles in the overall toughness of these nanocomposites. Ward et al. (2006) analyzed plastic deformation mechanism of Al-Si nanocomposite using MD simulations and they found that the onset of non-linearity in the stress-strain curves correlates with the generation of dislocations or grain boundary motion, and both dislocation and grain boundary mechanisms are suppressed due to the inclusion of Si particle in Al grains. They further demonstrated that with higher Si content the Al deformation is constrained further and the Al/Si interface deformations are more distributed, with an associated increase in the nanocomposite elastic modulus and yield stress with increasing Si content. By analyzing failure mechanisms of these nanocomposites, they found that the nanocomposites fail primarily along the Al/Si interface and failure strength remains the same as that of all-Al nanograin polycrystals. They suggested that the control of the interfaces through material modification may thus be one route by which Al/Si nanocomposite properties could be enhanced even further.

Momeni (2014) studied the ZnO nanowires reinforced nanocomposites using multiscale approach. Their simulation results disclosed that nanowires with a larger aspect

ratio and a smaller diameter can carry a larger portion of applied stress and are preferable in designing high-performance nanocomposites. Qi and Cheng (2004) studied Ag-Ni nanocomposites using MD simulations and found that introduction of a second phase reduces grain rotation-induced grain growth and leads to the initiation of cracks along the Ag-Ni interface, thus decreasing the fracture strain relative to single-phase nanocrystals, consistent with general expectations.

Moreover, the strengthening and the flow behavior in traditional composites are generally derived from direct and indirect sources. Direct contributions to strength are those that can be specifically attributed to the presence of the reinforcement during deformation, e.g., through the interaction of dislocations with the reinforcing particles. Indirect contributions to strengthening are derived from the microstructural changes within the matrix of the composite that evolve due to the presence of the reinforcement during its evolution and development, for example, due to grain refinement and reinforcement-derived interstitial solid-solution strengthening (Kampe et al., 1994). Mechanics-based approaches that independently incorporate volume fraction or size, the concepts of shear coupling and load transfer length, or rule-of-mixture (ROM)-based approaches are available to study the behavior of composites. Similarly, matrix-based models, that is, models whose predicted strength increases are a consequence of structural changes in the matrix only (as modified by the presence of the reinforcement), represent a fundamental means to examine and understand strengthening in discontinuously reinforced composites. Prominent among the matrix models is the oft-referenced Orowan (dislocation looping) strengthening mechanism (Kampe et al., 1994; Aikin, 1997). However, as applied to microstructures that constitute many particulate-reinforced composites, this model frequently largely underestimates actual magnitudes of strengthening, primarily as a consequence of the particulate being too large, i.e., too distantly spaced, to lead to significant strengthening by this means. Performance underestimates are also conceivable if other concurrent or superimposed strengthening mechanisms, either purposely or inadvertently active, are ignored in the analyses. However, the motivation to develop discontinuously reinforced ceramic-ceramic composites has suffered from a general shortage of meaningful and systematic studies and from the consequent shortage of well-developed and broadly applicable models of strengthening.

Understanding the mechanisms controlling mechanical properties will allow more

intelligent decisions to be made when tailoring a composite system for a specific application (Aikin, 1997). Therefore, it is the intent of this chapter to understand the deformation mechanisms of bio-inspired, discontinuously reinforced, RSM and SSM nanocomposite models, in doing so to contribute to the general understanding of stiffening, strengthening and toughening in these composites. MD simulations, which has been extensively used in studying atomistic plastic deformation mechanisms (Zhang et al., 2016a; Pei et al., 2015), is used to investigate the deformation behavior of nanocomposites.

Details of the computational methods used in the present study were explained Chapter 2. The results of our analysis and discussion with other results from literature are done in Section 3.3. The main conclusions are presented in Section 3.4.

3.2 Simulation Methodology

The simulated geometry is shown in Fig 3.1. Regularly staggered model is shown in

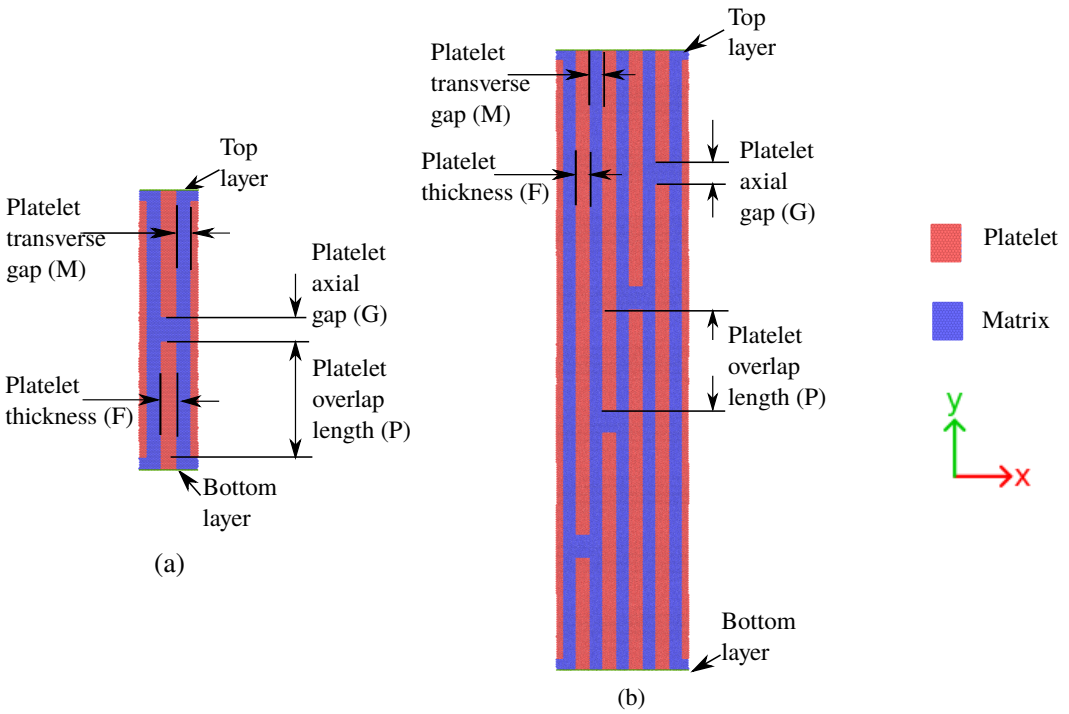

Figure 3.1 Details of the model considered for MD simulations: (a) regularly staggered model (RSM), and (b) stair-wise staggered model (SSM). All the four characteristic dimensions such as platelet thickness, overlap length, platelet axial and transverse gaps are kept same for both the models shown.

Fig 3.1a and stair-wise staggered model is shown in Fig 3.1b. These two models mimic the biological nanocomposite structure, in order to develop ceramic matrix nanocomposites. The platelet thickness, platelet transverse and axial gaps as well as platelet overlap lengths are kept the same in both the models. The models are subjected to uniaxial tension by applying a constant strain rate of 10^{-6} (in reduced units) under isothermal-isobaric conditions. In order to mimic the uniaxial tensile test, stresses normal to the loading directions are maintained zero and a constant temperature of 0.0001 is maintained throughout the tensile test. This low temperature is used to focus our attention on the influence of structural features rather than on the effect of temperature, which has been used in other MD simulations as well (Zhang and Ghosh, 2013; Sainath and Choudhary, 2015). Further modeling and other details were explained in Section 2.2. All simulations were carried out using parallel molecular dynamics code LAMMPS (Plimpton, 1995). The open visualization tool (OVITO) is used to visualize MD data and generate snapshots (Stukowski, 2010).

3.3 Results and Discussion

The stress strain diagrams obtained using MD simulations are shown in Fig 3.2. In order to find the mechanical behavior of constituent materials, homogeneous models of constituent's materials also studied. In Fig 3.2, the stress-strain diagrams of homogeneous matrix and platelet are shown. The homogeneous matrix model shows continuous increase of stress with strain and undergoes brittle failure. The homogeneous hard platelet also has similar stress-strain behavior, but the stiffness and strength are ten times that of the matrix. As the homogeneous models are defect-free, the dislocations are not generated during tensile test and the models undergo rapid fracture at the maximum stress. Therefore, homogeneous model has a smooth stress-strain curve.

The RSM and SSM models show mechanical behavior completely different from the above described homogeneous models (Refer Fig 3.2). Though these nanocomposite models are made up of the brittle constituents, the stress-strain diagrams show a post-peak flow behavior (where stress remains approximately a constant value) which is very similar to the ductile materials. The stress-strain diagrams of these composite materials also show fluctuations beyond the peak stress. In these models, the tips of the

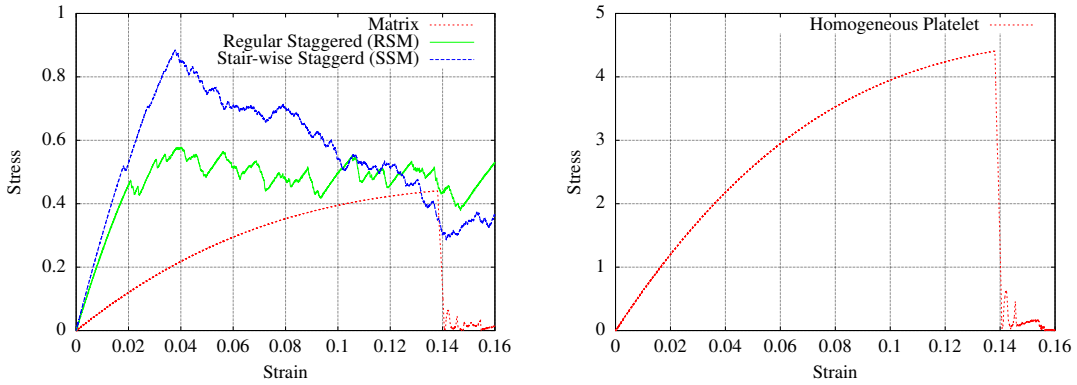

(a) (b)

Figure 3.2 (a) Stress-strain diagram for the homogeneous matrix, RSM, and SSM models. (b) Stress-strain diagram of homogeneous platelet. The hard platelet has a stress-strain diagram similar to that of matrix and undergoes brittle failure, but the values of stiffness and strength are ten times that of the matrix.

platelets act as a source for generation of dislocations (Refer Fig 3.3). The interactions of the dislocations generated in the matrix phase as well as the intermittent pullout of platelets during tensile test causes the ups and downs in the stress-strain diagram (See the following discussion on analysis of deformation mechanisms).

The RSM model shows uniform flow behavior beyond the peak stress, i.e., ups and downs of stress about a constant value. In contrast, the SSM model shows continuous decreasing of stress with strain after reaching the maximum stress. The reason for this behavior is analyzed in the following. Fig 3.3 show the deformation mechanisms observed for RSM and SSM models. As the matrix is softer than the platelet, the major deformation mechanisms occur only in the matrix region. The atoms with defects are captured by centrosymmetric parameter. Fig 3.3a(i) and Fig 3.3b(i) show the complete undeformed nanocomposite of RSM and SSM models, where both the platelet and matrix are observed. Whereas, Fig 3.3a(ii) and Fig 3.3b(ii) show the complete undeformed nanocomposite structures after the removal of defect-free atoms of matrix. There are no defects in the undeformed configuration and hence, the matrix phase is not observed. The subsequent snapshots show specific deformation mechanisms observed for the RSM and SSM models. In the case of RSM model, Fig 3.3a(iii) shows the nucleation of dislocations at platelet tips, Fig 3.3a(iv) shows movement of dislocations towards interface, Fig 3.3a(v) shows the arrest of dislocations at the interface,

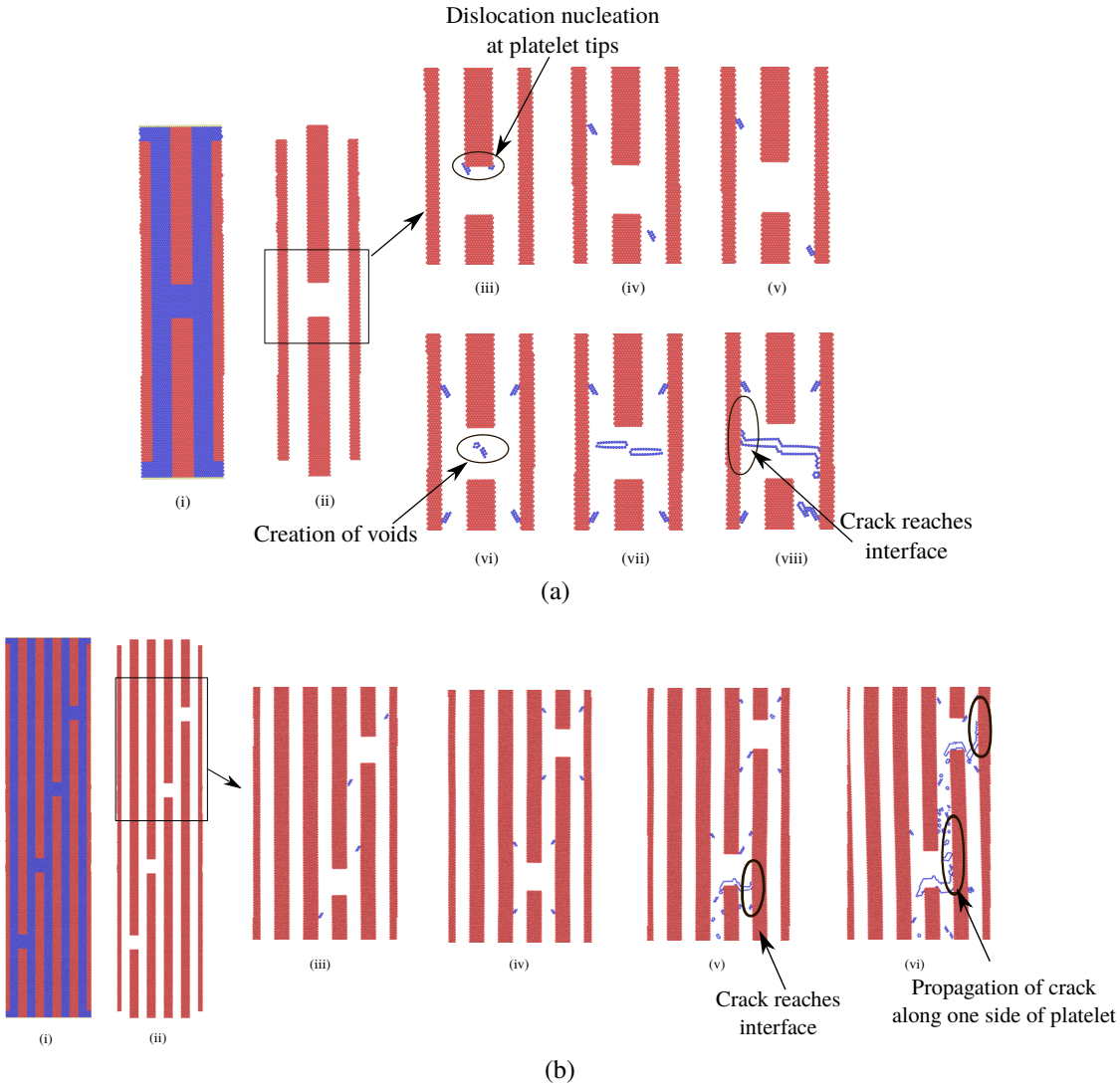

Figure 3.3 Typical deformation processes of (a) RSM and (b) SSM models. The atoms of matrix which does not have defects are removed for clarity. Cracks propagate along the interface in both sides of the platelet in RSM model. In contrast, crack propagation in one side of the platelet is more rapid compared to other side in SSM model. More details about each snapshot are described in the text.

Fig 3.3a(vi) shows the creations of voids at the matrix, Fig 3.3a(vii) shows the creation of cracks from the voids and extension of cracks, and Fig 3.3a(viii) shows the arrest of cracks at the interface and subsequent crack growth along the interface on both sides of the platelet. Once the matrix has failed, the pullout of platelet occurs, through the interfacial sliding. In SSM model, Fig 3.3b(iii) and Fig 3.3b(vi) show the initial deformation mechanisms which are similar to that of RSM such as nucleation of dislocations at platelet tips and arrest of dislocations. Fig 3.3b(v) shows the creation of cracks on one side of the platelet. Fig 3.3b(vi) shows the growth of interfacial crack on one side of the platelet.

In both the models, dislocations nucleate at the platelet tips and move towards the interface of the adjacent platelets as the strain increases. Once the dislocations are arrested by the interface, the voids and cracks are generated at the axial gap region (the vertical gap between the ends of the platelets, see Fig 3.1). Thereafter, the crack grows and reaches the platelet-matrix interface. Further application of strain causes the crack to grow along the interface. Pullout of platelets and interfacial sliding occur thereafter. The main difference in the deformation mechanisms between the RSM and SSM models is in the growth of the interfacial crack. The RSM model shows the interfacial crack growing on both sides of the platelet (See Fig 3.3a(viii)). However, the SSM model shows rapid crack growth only in one side of the model (See Fig 3.3b(vi)). The RSM model is symmetric and the SSM model is asymmetric which may cause difference in the stress distribution between the two sides of the platelets in the SSM models. This could be the reason for the symmetric crack propagation in RSM model and rapid crack growth in only one side in the case of SSM model. This phenomenon is further analyzed by measuring the change in overlap length (the region where adjacent platelets overlap on each other, see Fig 3.1) with applied strain and is shown in Fig 3.4a. Here, the SSM model shows a rapid decrease in the overlap length with strain due to fast interfacial crack growth. In the case of RSM model, the overlap decreases at a much slower rate. Moreover, the variation of strain undergone by the platelets for the overall applied strain on the nanocomposite model is shown in Fig 3.4b. Platelet strain reaches a maximum value very rapidly, followed by a drastic drop for SSM model. Whereas, a smooth increase and drop in platelet strain is observed for RSM model. This shows that when the crack grows, the overlap length begins to decrease and the platelets begin to

unstrain. This fact can be understood from comparing the Figs 3.4a and 3.4b.

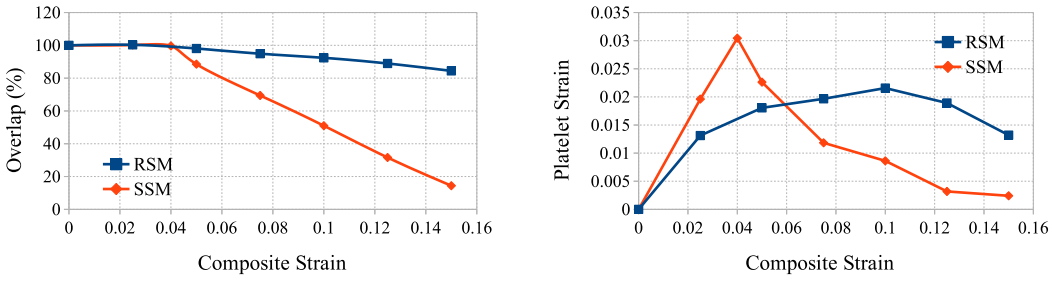

(a) (b)

Figure 3.4 The percent change in the average overlap length with applied composite overall strain is shown in subplot (a). As the crack grows faster in the SSM model, the overlap region reduces rapidly. The change in the platelet strain with applied composite overall strain is shown in subplot (b). Unloading of the platelets beyond the peak loading is consistent with the reduction in platelet overlap length.

Anup et al. (2008) studied the deformation behavior of RSM models using continuous damage random threshold fuse model (CDRFM). They found that the matrix failure as opposed to the platelet breakage provides better toughness in these models. The present study of MD simulation on RSM and SSM models also shows the similar phenomenon that through matrix failure the nanocomposite attains the higher toughness values. It is also to be noted here that in study of effect of aspect ratio (length to thickness ratio) of platelets carried out in Chapter 5, this type of deformation mode (i.e., matrix failure) causes high toughness in the nanocomposite models, when the aspect ratio of platelets is lower than critical aspect ratio. Zhang et al. (2010) studied analytically various platelets arrangements in uniaxial composites and showed that the regularly staggered and stair-wise staggered models could achieve an optimum combination of superior mechanical properties. Moreover, they showed that the stair-wise staggered model can achieve higher stiffness and strength for higher aspect ratios. We also show in Chapter 5 using MD simulations that the stair-wise staggered models possess high stiffness and strength for higher values of aspect ratio (length to thickness ratio of platelets). However, the regularly staggered model showed higher toughness for these aspect ratios. Though the stiffness and strength of the SSM models could be improved by changing the structural and/or material parameters, toughness enhancement could not be achieved by varying these parameters (Zhang et al., 2010). The low

toughness of the stair-wise staggered model is a huge impediment in using them for high performance advanced nanocomposites. Our study shows that the lower toughness of SSM model is mainly due to the crack propagation in overlap region. Therefore, providing crack arresting mechanisms in this region could enhance the toughness of these nanocomposites.

Comparison with 3D model

In order to understand the effect of dimensionality on the deformation processes, a 3D model of the regularly staggered arrangement is studied and compared with the corresponding 2D model. The FCC crystal structure is used in the 3D simulation. However, all the geometric parameters (shown in Fig 3.1) are maintained same as that of 2D model. Similarly, the LJ interatomic potential and the LJ parameters for platelets, matrix, and interface are maintained same as that of the 2D model. Moreover, the same strain-rate is applied in 3D model as well. The typical plastic deformation processes observed in 3D model is shown in the Fig 3.5. For better understanding of the deformation processes, the defects generated in the matrix only are shown. The dislocations are extracted using Dislocation Extraction Algorithm (DXA) (Stukowski et al., 2012).

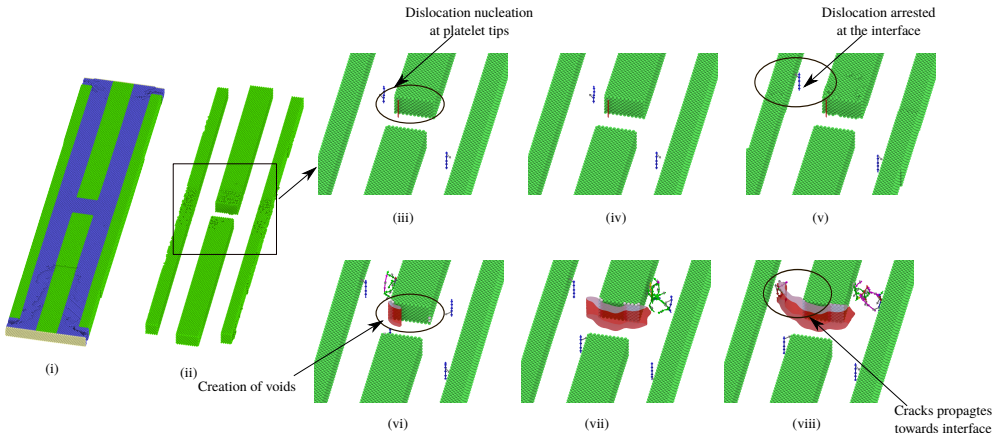

Figure 3.5 Typical deformation processes in a 3D model of RSM model. The atoms of matrix which does not have defects are not shown for clarity. In this figure, blue lines indicate edge dislocations, and red color indicates crack surface.

In the deformation behavior of 2D model which is shown in the Fig 3.3a, the defects are generated from the platelet tips and are seen moving through the matrix. Thereafter, the defects are arrested by the matrix-platelet interface. Following the arrest of the

movement of the defects, the cracks are generated in the platelet-to-platelet gap region. Further, the pull-out of the platelets from the matrix occurs. Whereas, in the 3D model, perfect edge dislocations are generated from the platelet tips and move through the matrix (see Fig 3.5). The dislocations are observed as straight lines rather than as dislocation loops, because periodic boundary condition is maintained in the thickness direction. Similar to that observed in 2D model, the dislocations are arrested at the interface. Further, at higher strains, the interactions of dislocations are observed. Thereafter, the creation of cracks and the pull-out of platelets occur similar to that observed in the 2D model. This suggests that the 2D model could capture the essential deformation processes occurring in the 3D model.

3.4 Conclusion

Atomistic simulations are used to capture various plastic deformation mechanisms occurring in the bio-inspired nanocomposite models, RSM and SSM. For same overlap and axial gap lengths, RSM model shows better flow behavior and toughness, whereas the SSM model could attain higher Young's modulus and strength. Moreover, the rapid crack growth in the overlap region of the SSM model causes the reduced flow behavior and lower toughness. This rapid crack growth could be mainly due to its asymmetric geometry. By providing cracks arresting mechanisms in the overlap regions, a better combination of stiffness, strength, and toughness could be possible in the SSM models. This will be considered in future studies.

Molecular dynamics simulations only require atomistic information such as atomic positions and interatomic forces and could able to predict various plastic deformation mechanisms occurring in the model. It shows the advantage of molecular dynamics simulations over finite element analysis. Moreover, these nanocomposite materials show a large amount of plastic deformation for large strain levels, though the nanocomposites are made up of brittle constituents. Therefore, nanocomposite materials made up of brittle materials like ceramics could lead to a good amount of ductility. These studies enhance our knowledge in the deformation mechanisms of bio-inspired, uniaxial brittle matrix nanocomposites. Our work in this chapter would lay the ground work for more computational and physical experiments.

CHAPTER 4

Effect of Strain-rate

Nanocomposite models are subjected to a wide range of strain rates under isothermal and adiabatic tensile loadings as well as shock wave loadings. The variation of mechanical behavior with different strain rates are investigated along with the visual analysis of the trajectories of the atoms. Our results show the existence of three strain rate regimes and two critical strain rates in all these analyses. The critical strain rates for adiabatic condition are found to be one order of magnitude higher than the isothermal loading condition. These findings are compared with the other molecular dynamics results available for nanowires and nanocrystalline materials. Moreover, from the MD simulations of nanocomposites, it is found that the soft phase undergoes various inelastic deformations depending on the applied strain rate. The understanding obtained could be useful in the design of advanced nanocomposite materials.

4.1 Introduction

As mentioned in the introduction, this work is focused on the development of bio-inspired nanocomposite models and on the investigation of their deformation behavior and mechanical properties. The studies are mainly related to the applicability and transferability of the key strategies of biological nanocomposites to non-biological engineering materials, specifically to brittle matrices. The knowledge that can be gained from this analysis could lead to the design of advanced engineering materials. Deformation behavior of nanocomposite materials depends on the microstructural architecture, properties of constituents and interfaces, temperature and strain rate (SR) applied on the model. In this chapter, the focus is on the effects of strain rate on two different architectures (RSM $\&$ SSM). These studies are necessary to understand their suitability for dynamic applications. Moreover, the MD can simulate strain rate higher than $10^6 s^{-1}$. Therefore, strain rate studies are necessary to make sure that the simulation results can actually predict results equivalent to physical experiments and are physically realizable.

Previously, MD simulations have been effectively used to study the influence of strain rates on the mechanical behavior of many nanoscale materials. The focus of many of the studies has been to elucidate the variation of deformation mechanisms associated with different strain rates. The studies by Koh et al. (2005); Koh and Lee (2006a) and Wen et al. (2008) have shown that three distinct deformation mechanisms exist depending on the strain rate, when metallic nanorods are subjected to tensile test simulations: crystalline deformation ($SR < 10^9 s^{-1}$), transition from crystalline to amorphous deformation ($10^9 s^{-1} > SR < 10^{10} s^{-1}$), and amorphous deformation ($SR > 10^{10} s^{-1}$). Ikeda et al. (1999) and Branício and Rino (2000) have observed amorphization-like deformation behavior at higher strain rates ($SR > 10^{10} s^{-1}$) on metallic nanowires. Vo et al. (2008), Vo et al. (2009) and Brandl et al. (2009) studied the effect of strain rate on a nanocrystalline material and concluded that strain rate controls the on-set of plasticity and dislocation activities. They showed that the dislocation activities decrease with increasing strain rate. Smith et al. (2014) studied the strain rate effect on nanocrystalline thin films. They demonstrated that the initial deformation mechanism is dislocation dominated at lower strain rate and twinning dominated at higher strain rate. Further, Pu et al. (2008) proposed the universal rate dependent energy release mechanisms. According to their study, the smaller relaxation time available at high strain rates causes high energy defects to be activated. On the other hand, the larger relaxation time available at low strain rates favors activation of low energy defects. Moreover, many studies have shown an increase in the yield and flow stress with strain rate (Tang and Marian, 2014; Brandl et al., 2009).

However, scant open literature is available on the effect of strain rate on the mechanical behavior of nanocomposites. Therefore, there is a need to study how the nanocomposites behave under varying strain rates. Moreover, as the aim of the thesis is to explore the mechanical behavior of bio-inspired RSM and SSM nanocomposite models, the effect of strain rate in these nanocomposite models are analyzed. However, the results are applicable to generic brittle matrix nanocomposites. This knowledge obtained from this study would be useful in the design of the advanced nanocomposite materials.

In addition to the exploration of deformation behavior over wide range of strain rates under isothermal uniaxial tensile loadings, the influence of adiabatic uniaxial tensile loadings as well as shock wave loadings are also studied. The adiabatic condition

is used to understand the mechanical response due to the effect of strain rate, when temperature is allowed to increase in the models (Koh and Lee, 2006b). Moreover, the uniaxial strain condition (strains other than loading direction are zero) which exists in the shock wave experiments, which are rarely studied (Luo et al., 2006) is also investigated in this chapter. Details of the computational methods used in the present study are similar to that explained in the Chapter 2. The results of our analyses and comparisons with other results from literature are discussed in Section 4.3. The main conclusions are presented in Section 4.4.

4.2 Model and Simulation Setup

The effect of strain rate in the bio-inspired brittle matrix nanocomposite models, RSM and SSM, are analyzed using atomistic simulations. As discussed in Chapter 2, the atomistic geometry is developed using two dimensional Lennard-Jones solid. The basic unit cell, hexagonal lattice structure, homogeneous model and the nanocomposite models are shown in Fig 2.2. The homogeneous model, which is the unreinforced platelet material, is built with 15 atoms in thickness and 50 atoms in length. Nanocomposite models are built with platelets reinforced in the matrix. The platelets are made of 10 atoms in thickness, 100 atoms in length for RSM model and 260 atoms in length for SSM model. The length of axial gap between the platelets is made with 10 atoms (refer Fig 2.2 for the nomenclature of the nanocomposite structure).

We analyze the influence of strain rate on the mechanical properties of model nanocomposites. Strain rate ($\dot{\varepsilon}_{yy}$) is varied from 10^{-6} to 10^{-1} in the unit of strain per unit reduced time. In order to compare our results with that in literature, the values in reduced units are converted into SI units. For that purpose, the assumed LJ parameters for a typical atom are as follows: $\sigma_{LJ} = 10^{-10}\ m$, $\epsilon_{LJ} = 10^{-21}\ J$, and assumed mass of an atom, $m_a = 10^{-25}\ kg$. These typical values lead to the reduced time equivalent of 1 ps (1 picosecond = $10^{-12}\ s$), and the length of simulated model of 20 nm (1 nanometer = $10^{-9}\ m$). The range of strain rates applied in our MD simulations is 10^{-6} to 10^{-1} in reduced units, which is equivalent to $10^{6} s^{-1}$ to $10^{11} s^{-1}$ in SI units based on the properties of a typical atom given above.

In the next section, we initially analyze the effect of strain rate on a 2D homoge-

neous model. Thereafter, the effect of strain rate on nanocomposite models is analyzed. The analysis is carried out through the following steps. 1) Study of the evolution of stress, potential energy (PE), and kinetic energy (KE) of the system with strain for different strain rates, 2) Study of the variation in mechanical properties, such as Young's modulus, strength and toughness, with different strain rates, and 3) Study of the evolution of deformed structure by visual analysis for different strain rates. The combination of the three different approaches should provide a complete characterization of the microscopic dynamics and mechanical behavior of the atomic system. (Note: all quantities are expressed in reduced units by default. If we use SI units, it will be mentioned.)

4.3 Results and Discussion

It seems necessary to understand the influence of strain rate on a homogeneous model, before we begin the study of influence of stain-rate on a heterogeneous nanocomposite model. Therefore, initially we carried out uniaxial tensile tests on homogeneous model

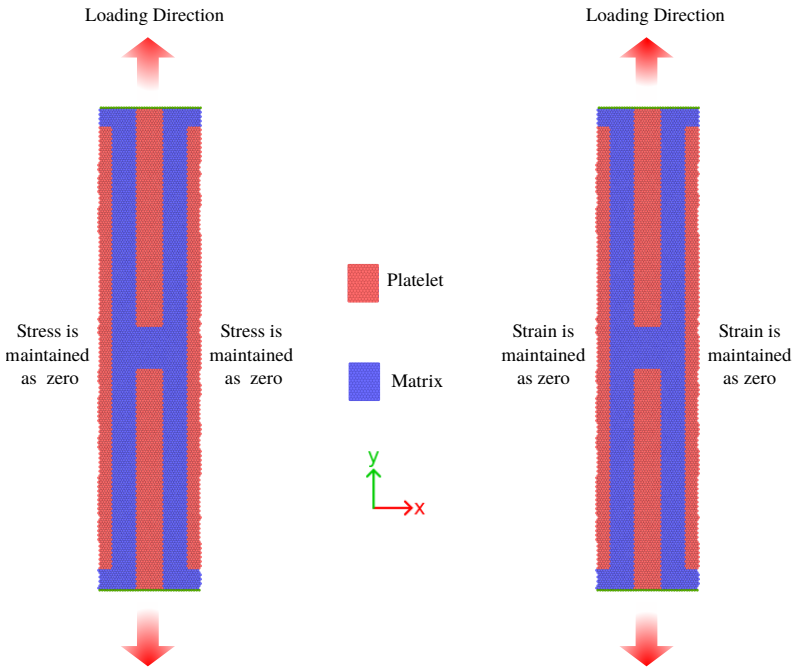

(a) Uniaxial Tensile Stress (b) Uniaxial Tensile Strain

Figure 4.1 State of stress during (a) uniaxial tensile test (uniaxial stress condition) and (b) shock wave loading (uniaxial strain condition).

for various strain rates. Thereafter the effects of strain rate on nanocomposite models are examined. Three types of simulations are considered in the nanocomposite mod-

els. First, isothermal uniaxial tensile test is performed and the variation of mechanical properties is analyzed for different strain rates; the temperature of the models is kept constant during the simulations. Second adiabatic uniaxial tensile test is done; the temperature of the models is allowed to vary. At last, the effects of strain rate during the shock wave loadings are analyzed. During shock wave loadings, the model undergoes uniaxial strain rather than uniaxial stress condition which used to occur during uniaxial tensile tests. Fig 4.1 schematically shows the different state of stress occurring in uniaxial tensile test and shock wave loadings.

4.3.1 Homogeneous Model

In this section, we analyze the mechanical behavior of homogeneous 2D LJ solid subjected to different strain rates. In order to mimic the nanowires in 2D, free and expandable boundary is given in both the X and Y directions. The model is strained in the Y-direction and neither pressure nor temperature control is used in the simulations. However, it is to be noted here that proper pressure control is necessary only if the X-direction is periodic. Moreover, no temperature control is used to study the temperature increase. This section also explains the validation of our MD methods by comparing our results with that of existing literature. Fig 4.2a shows the stress-strain curves for different values of strain rates. The stress-strain diagram is unaffected by the strain rate, except at the strain rate of 10^{-1} where a small deviation is observed. We could also observe that the increasing strain rate is delaying the on-set of failure. The stress-strain diagram matches with the other MD simulations reported in literature (Buehler, 2008). This confirms the validity of the MD methodology used in our simulations.

While the concept of stress in the study of mechanical behavior of atomic systems is well known (Tsai, 1979; Zhou, 2003; Zimmerman et al., 2004), the use of the concept of potential energy (PE) and kinetic energy (KE) in the present study needs a little more explanation. The PE in atomistic simulations refers to the internal energy of the system. In our simulations, the initial undeformed model is equilibrated to attain zero-stress which also corresponds to zero-strain. The PE corresponding to the zero-stress and zero-strain state of the model is also noted down and is referred to as the "zero-strain PE". The strain is increased in the model and the increase in PE (ΔPE) of the model

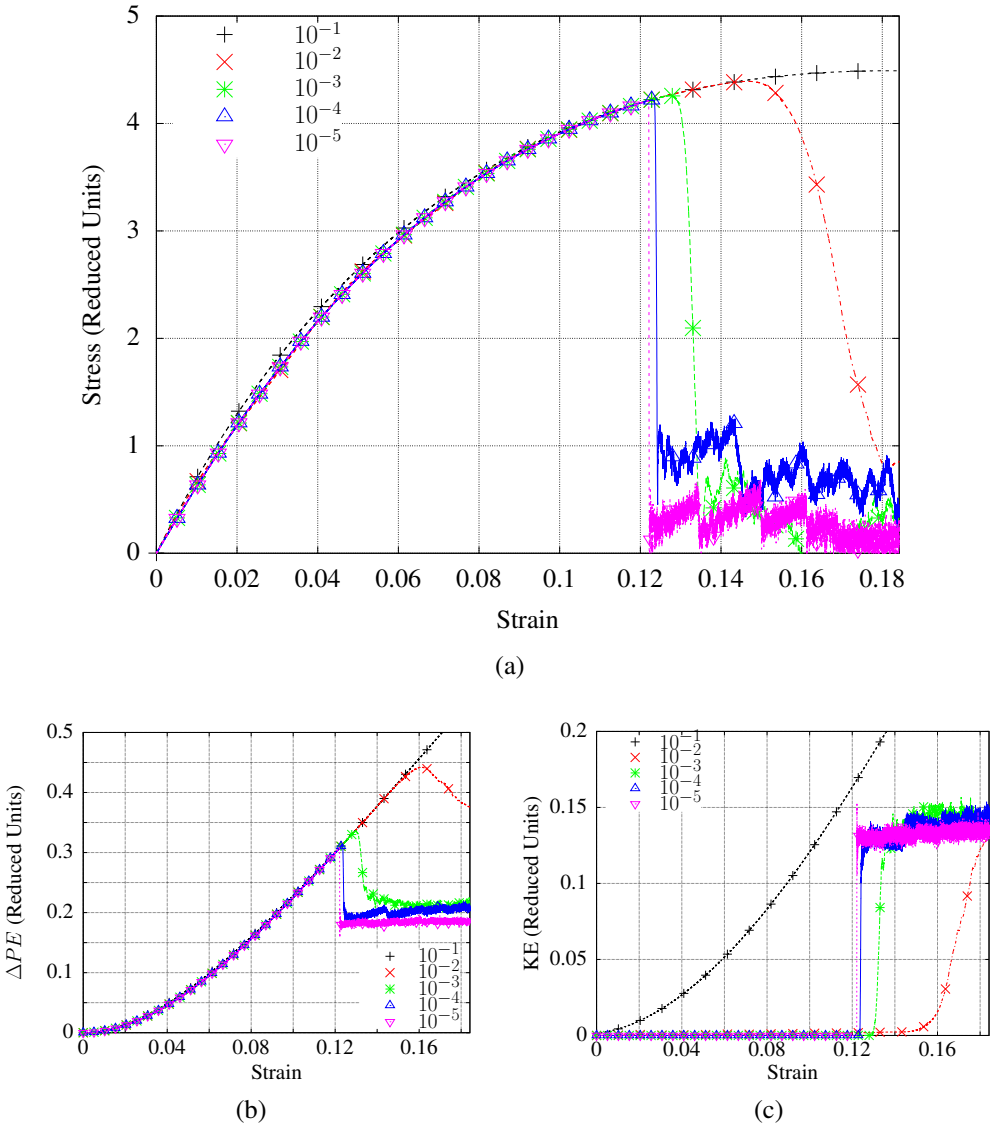

Figure 4.2 Influence of strain rate on homogeneous model: (a) the stress-strain diagram (note: the onset of failure strain increases with strain rate), (b) the variation of potential energy (PE) with strain, and (c) variation of kinetic energy (KE) with strain. The strain rates shown are in reduced units.

from the "zero-strain PE" is also calculated. This ΔPE is a measure of the stored energy inside the material. The ΔPE versus strain is also plotted to understand how the ΔPE varies with strain. The maximum value of ΔPE is taken as a measure of toughness of the material since it expresses the maximum value of energy stored in the material until failure. The KE in the model is calculated after subtracting the component of KE due to the velocity gradient applied on the model. Therefore, as long as the value of KE remains at a constant value of about zero (which is the initially applied temperature on the model) with increase in strain, it implies that the initially defect free crystal continues to undergo defect free deformation. Moreover, the increase in KE in our model could be considered as a measure of defects generated in the model implying plastic work (Rittel et al., 2012; Ruestes et al., 2014).

Figs 4.2b and 4.2c show the variation of PE and KE with strain for different values of strain rates. The PE curves do not change with different strain rates. In contrast, though the KE has constant value close to zero for lower strain rates, a drastic change in KE is observed for the strain rate value of 10^{-1}. This strain rate is close to the vibrational frequency of the model system studied. The vibrational frequency of the LJ system can be calculated as $\nu = (2\pi)^{-1}\sqrt{k/m}$ (m refers to the atomic mass equal to unity in reduced unit and k is stiffness). The stiffness can be calculated as $k = dF/dr|_{r=r_{eq}}$, where r_{eq} is the equilibrium atomic distance and F is interatomic force. Interatomic force can be obtained by differentiating the interatomic potential as $F = -d\phi/dr$, where ϕ is given in Eq (2.1). The equilibrium interatomic distance (r_{eq}) is the distance at which interatomic force becomes zero and can be obtained as $r_{eq} = \sqrt[6]{2} \times \sigma_{LJ}$. The relation between the LJ parameters and the vibrational frequency can be obtained as $\nu = 1.2\sqrt{\epsilon_{LJ}/m\sigma_{LJ}^2}$ (Falk and Langer, 1998). This calculation gives the vibrational frequency for each material used in the simulations as follows; $\nu_{homogeneous} = 1.2$, $\nu_{platelet} = 1.2$ and $\nu_{matrix} = 0.38$, which are near the strain rate value of 0.1. When the strain rate is approaching the vibrational frequency of the system, the system is known to produce high magnitude of oscillation (Sahputra and Echtermeyer, 2013; Cui and Brinson, 2013). The huge increase in KE observed at the SR of 10^{-1} could be due to the applied strain rate approaching closer to the natural frequency of the atomic system.

The mechanical properties such as Young's modulus, critical stress and toughness are calculated from the stress-strain and PE-strain curves (refer Fig 4.2). Fig 4.3 shows

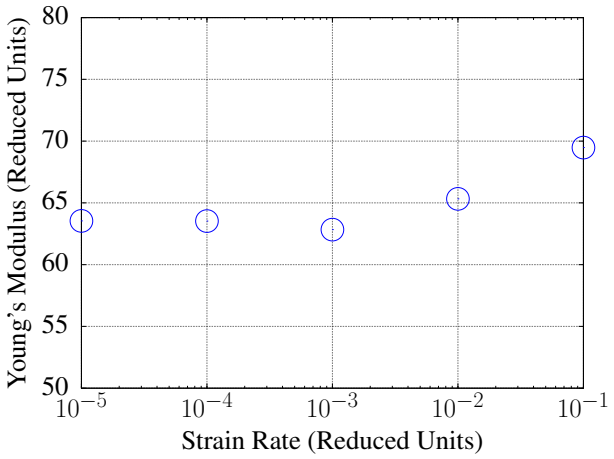

(a)

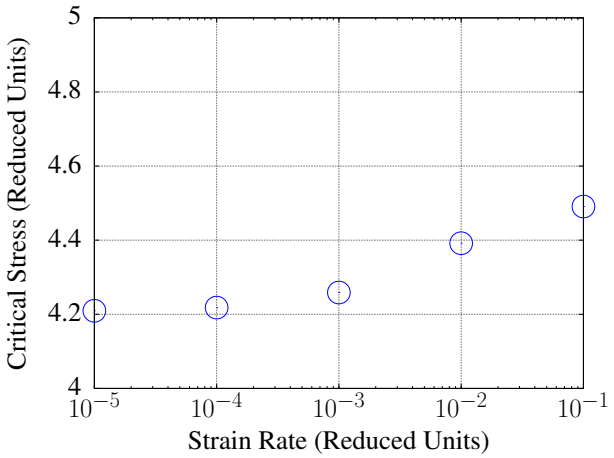

(b)

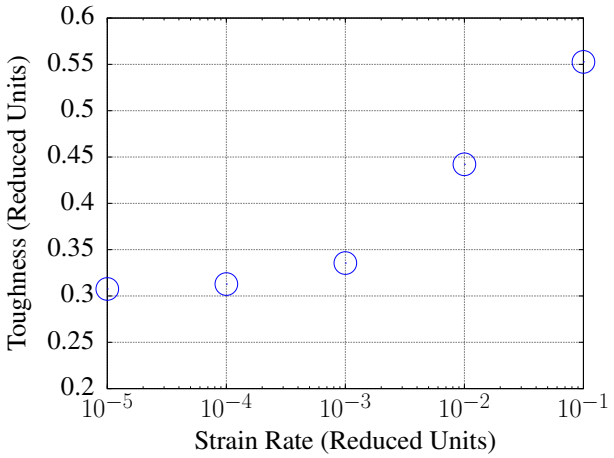

(c)

Figure 4.3 Variation of mechanical properties for different strain rates of the homogeneous 2D LJ solid modal: (a) variation of Young's modulus, (b) variation of critical stress, and (c) variation of toughness

the variation of these mechanical properties with different strain rates. From the figures, it is observed that for strain rates below 10^{-3}, there is no significant change in any of the measured mechanical properties. However, when the strain rate is increased above the value of 10^{-3}, we could observe an increase in the mechanical properties. This increase in the Young's modulus, critical stress and toughness could be due to the non-relaxation of the model as well as the delaying of failure strain (See the discussions in previous paragraphs and Fig 4.2). The non-relaxation of the model refers to the absence of any kind of defects in the model which can be understood from the visual analysis (See Fig 4.4d) discussed in the following paragraphs.

The visual analysis of the trajectories of atoms for different strain rates is carried out in the following. Fig 4.4 shows four subplots of the deformation mechanisms for the strain rates from 10^{-4} to 10^{-1}. In order to capture the lattice defects during deformation, the centrosymmetry parameter (CSP) (Kelchner et al., 1998) is used as mentioned in Chapter 2. When the value of the CSP of an atom is zero, it means that the atom belongs to an ideal crystal structure. Whereas, when the CSP value of an atom is other than zero, it indicates that the atom is part of the crystal structure containing a defect. The atoms forming part of defects are given different colors to visualize them.

For the strain rates of 10^{-4} and 10^{-3} ($\approx 10^{8}$ & $10^{9}s^{-1}$ in SI units), dislocation dominated deformations are observed as shown in Figs 4.4a and 4.4b. Dislocations emerging from the surface, dislocations interacting with each other and formation of voids are observed in these lower strain rates. However, it is emphasized here that these dislocations are observed only for a very small range of strains before the occurrence of the failure (approximately 12% to 13% of strain values). Therefore, these 2D LJ crystals are denoted as brittle materials which is similar to that observed by Abraham (1996) and Chang et al. (2013). As the crystalline structure is also observed along with the dislocations, this kind of deformation is referred to as the crystalline deformation in the present study. It is also observed that within these two strain rates, higher the strain rate, higher is the value of strain at which the dislocation activities emerge. Fig 4.4c shows the amorphous deformation occurring at the strain rate value of 10^{-2} ($\approx 10^{10}s^{-1}$ in SI unit). At this strain rate, no dislocation is observed. Fig 4.4d shows the deformation observed at a very high strain rate of 10^{-1} ($\approx 10^{11}s^{-1}$ in SI unit), where the atoms continue to follow crystalline deformation without any defects. Though we have used a simple

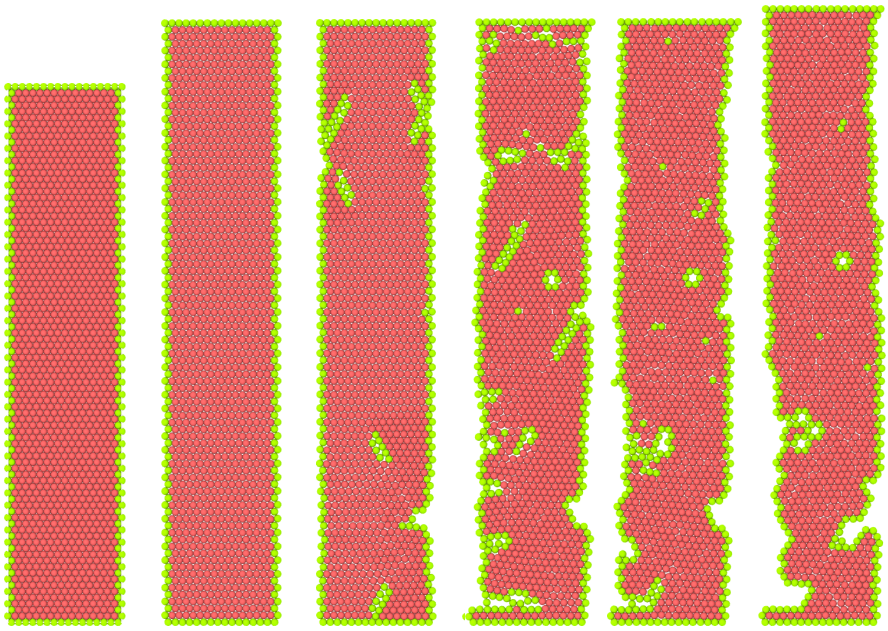

(a) 0.0 (b) 0.1205 (c) 0.121 (d) 0.1215 (e) 0.1220 (f) 0.150

(a) SR of 10^{-4}. Dislocations nucleation from the free surface, and the formation of voids are seen.

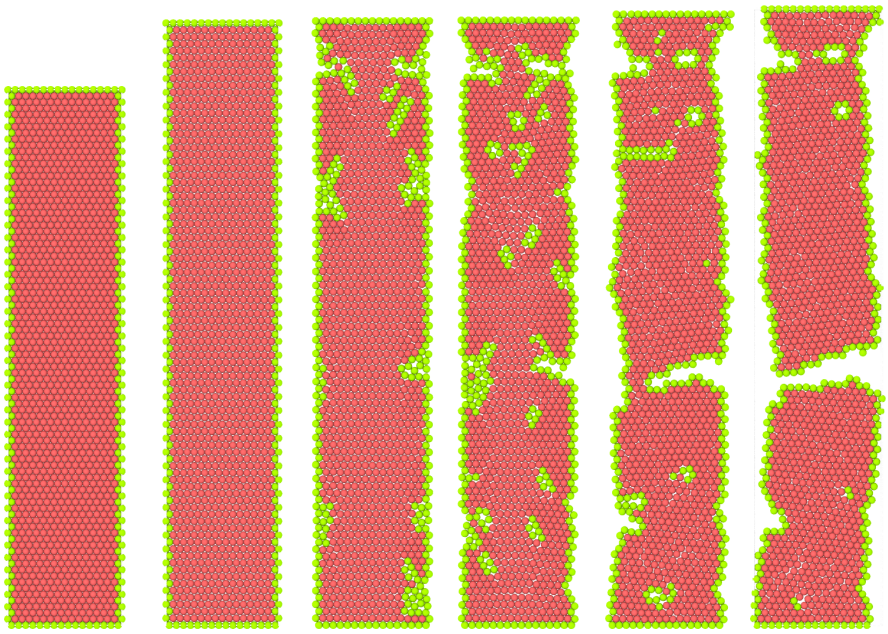

(a) 0.0 (b) 0.125 (c) 0.1285 (d) 0.13 (e) 0.14 (f) 0.150

(b) SR of 10^{-3}. Deformation mechanisms are similar to that of SR of 10^{-4}.

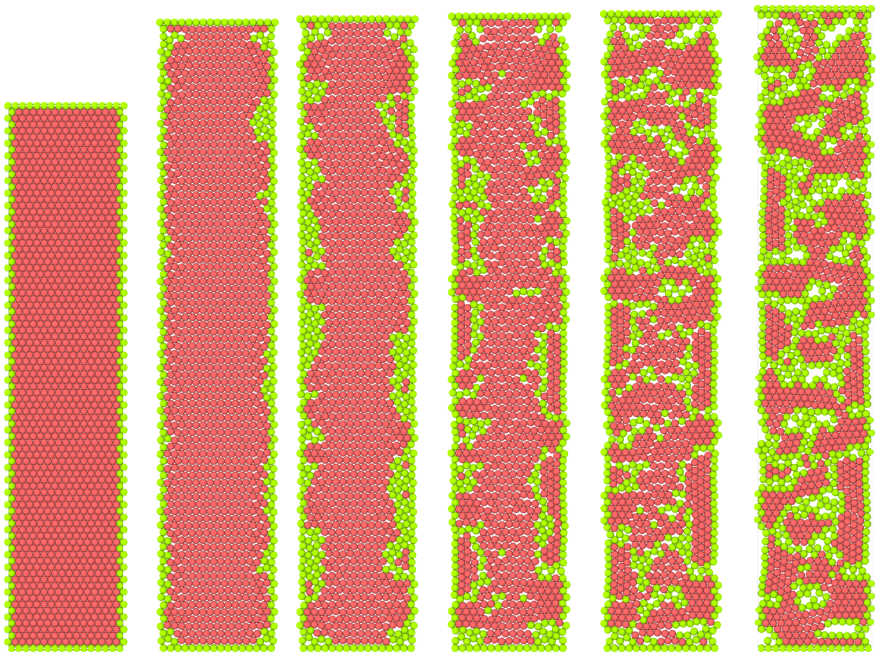

(a) 0.0 (b) 0.155 (c) 0.160 (d) 0.165 (e) 0.170 (f) 0.180

(c) SR of 10^{-2}. Amorphous deformation is seen in the snapshots.

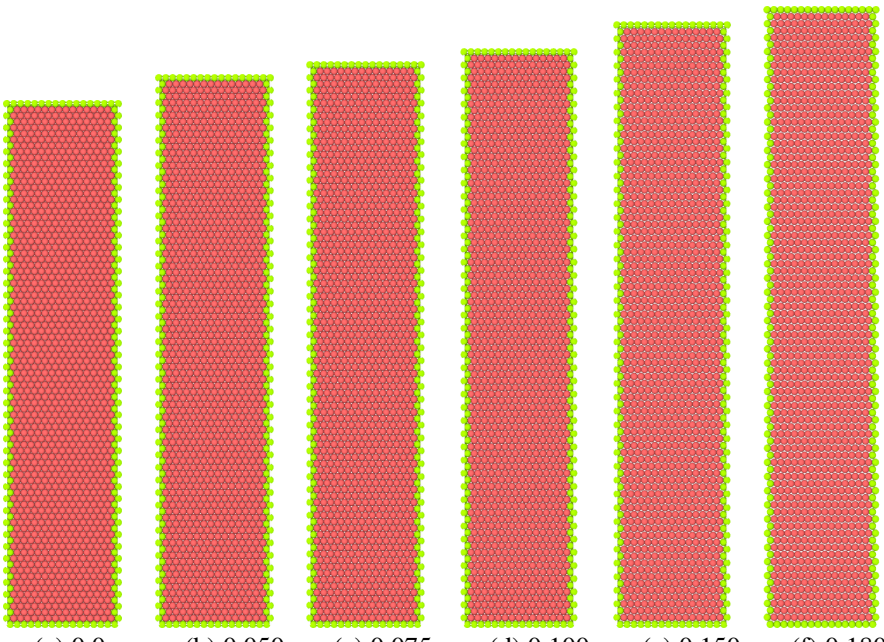

(a) 0.0 (b) 0.050 (c) 0.075 (d) 0.100 (e) 0.150 (f) 0.180

(d) SR of 10^{-1}. No deformation mechanism are observed.

Figure 4.4 Various deformation mechanisms and defect formations for different strain rates of homogeneous 2D LJ solid. The value of strain for each snapshot is given below corresponding snapshot. Atoms which are part of defects are given green color. (a) SR of 10^{-4} ($\approx 10^{8}s^{-1}$ in SI unit), (b) SR of 10^{-3} ($\approx 10^{9}s^{-1}$ in SI unit), (c) SR of 10^{-2} ($\approx 10^{10}s^{-1}$ in SI unit) and (d) SR of 10^{-1} ($\approx 10^{11}s^{-1}$ in SI unit).

2D LJ solid, various deformation mechanisms obtained for different values of strain rate are similar to that of 3D simulations available on literature for nanowires/nanorods (Ikeda et al., 1999; Koh and Lee, 2006b; Wen et al., 2008). However, the plastic deformation mechanisms observed in 3D occurs for large range of strains and result in ductile deformation. We could compare them because 2D LJ solids are simplifications of the 3D homogeneous nanomaterials, such as nanowires and nanorods.

4.3.2 Nanocomposite Model

In the previous section we have showed that the 2D LJ homogeneous hexagonal crystals are indeed brittle materials. In this section the mechanical behavior of bio-inspired brittle matrix nanocomposite models is analyzed.

4.3.2.1 Isothermal uniaxial tensile loadings

In this simulation, uniaxial tensile stress loading is simulated. The uniaxial tensile stress condition implies that the stress is allowed to increase only in the loading direction and zero stress is maintained in all the other directions (see Fig 4.1). Moreover, temperature is maintained at a constant value. For these purposes, Berendsen barostat (Berendsen et al., 1984) is used to maintain the global stresses in the direction normal to the loading direction as zero, and Berendsen thermostat (Berendsen et al., 1984) is used to maintain the temperature at a value of 0.0001. In the following subsections, the effect of strain rate on the mechanical response during the isothermal uniaxial tensile loading condition is explored.

Variation in stress-strain diagram The stress-strain curves obtained for the regularly staggered model (RSM) and stair-wise staggered model (SSM) for different values of strain rates (SR) are shown in Figs 4.6a and 4.6b. The stress-strain curves for SR $\leq 10^{-5}$ ($\approx 10^{7}s^{-1}$ in SI unit) show a predominant zigzag nature. The stress-strain curves for SR $\geq 10^{-2}$ ($\approx 10^{10}s^{-1}$ in SI unit) show a drastic increase in the value of stress which is in contrast to that of decreasing trend seen in stress-strain curves for $10^{-4} \leq SR \leq 10^{-3}$. Whereas, for SR $> 10^{-5}$ and SR $< 10^{-2}$, the stress-strain curves neither has a zigzag nature nor show a drastic increase.

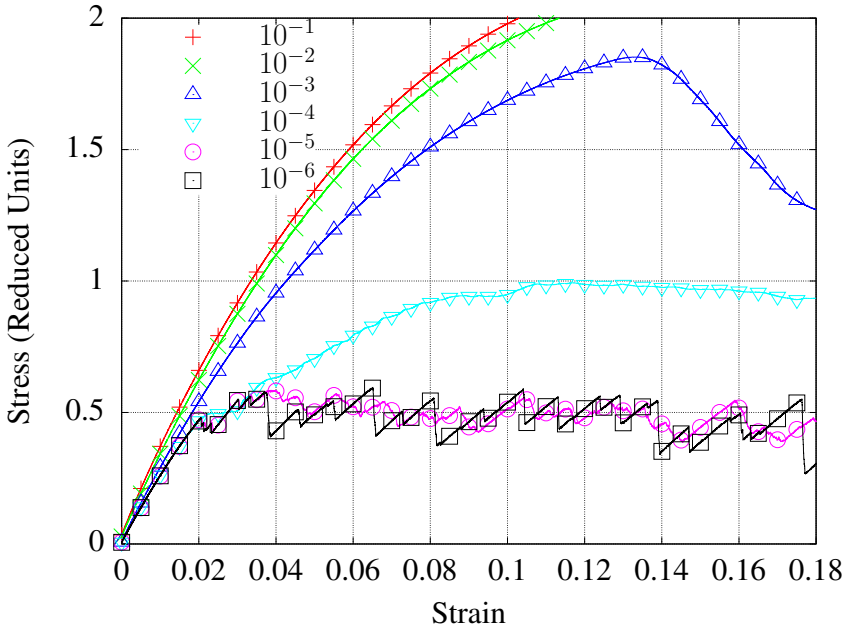

(a)

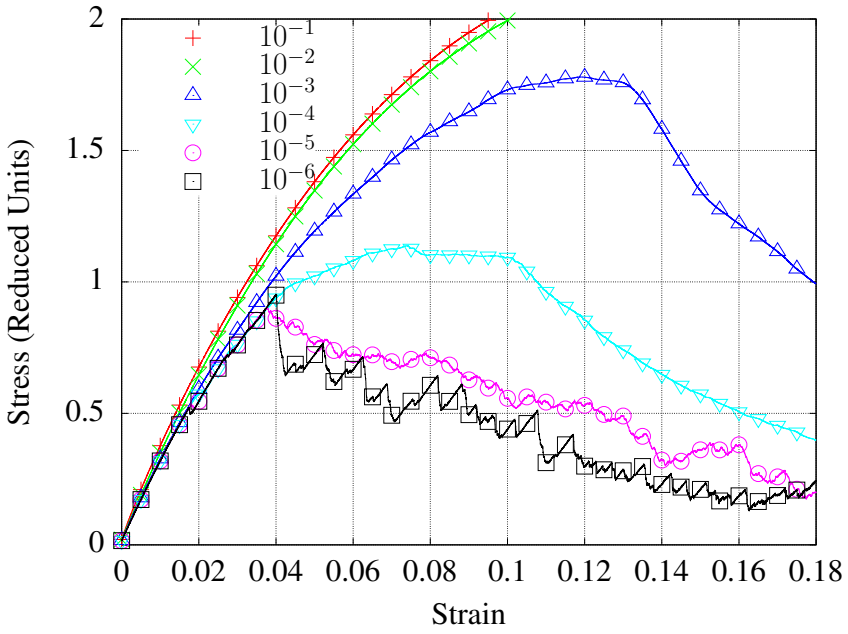

(b)

Figure 4.6 Influence of strain rate in the isothermal uniaxial tensile stress-strain diagram of the (a) RSM and (b) SSM models. The strain rates shown are in reduced units.

We classify the mechanical behavior of the nanocomposite models based on strain rates as follows, i.e.,

1) SR $\leq 10^{-5}$ ($\leq 10^{7}s^{-1}$ in SI unit): The stress-strain diagram shows a zigzag nature. This range of strain rates is referred to as the SR Regime-I.

2) SR $\geq 10^{-2}$ ($\geq 10^{10}s^{-1}$ in SI unit): A drastic increase in the magnitude of stress occurs compared to SR $< 10^{-2}$. These strain rates are referred to as the SR Regime-III.

3) SR of 10^{-4} to 10^{-3} ($10^{7} < SR < 10^{10}$ s^{-1} in SI unit): The variations in stress do not show any characteristics as observed in SR Regime-I or SR Regime-III. This range of strain rates is referred to as the SR Regime-II.

At a certain value of strain, the visual analysis shows the emission of dislocations (the results of visual analysis will be further explained in Section 4.3.2.1). These dislocations, as it causes the relaxation of the stresses in the model, leads to the occurrence of first reduction in the stress level in the stress-strain diagram. The strain value at which the stress starts to decrease (the occurrence of emission of dislocations) is termed in the present study as the "nanoyield strain". The stress corresponds to the nanoyield strain is denoted as "yield stress". Below the nanoyield strain, pure crystalline deformation is observed. Further discussion about the variation in mechanical properties and visual analysis of the deformed structure are done in the following subsections.

Variation in mechanical properties In order to understand the effect of strain rate on the mechanical properties, the percentage changes in the mechanical properties are calculated with respect to that at SR of 10^{-6} which is the lowest strain rate simulated. The expression to calculate this percentage is given in Eq (4.1).

$$\%\ Difference = \frac{Property\ at\ a\ particular\ SR - Property\ at\ SR\ of\ 10^{-6}}{Property\ at\ SR\ of\ 10^{-6}} \times 100 \tag{4.1}$$

Fig 4.7 shows the variations of percentage differences in Young's modulus, Poisson's ratio, flow stress and toughness values for both the models studied. The Poisson's ratio is calculated as ratio of the strain along X-direction to the strain along Y-direction at the beginning of the straining of the model. It is to be noted here that the value of Poisson's ratio at the SR of 10^{-6} is obtained as 0.33 for both the models. When the strain rate is

increased from 10^{-6} to 10^{-5} ($\approx 10^{6}$ to $10^{7}s^{-1}$ in SI unit, in SR Regime-I), no significant change is observed in the Young's modulus and yield stress values of both the models. The value of Poisson's ratio is found to be reduced by an amount of 10% in both the models. Further, the flow stress and toughness values do not change significantly in RSM model. However, when the strain rate is increased from 10^{-6} to 10^{-5} in the SSM model, a 25% increase in the flow stress and toughness is observed.

When the $SR > 10^{-5}$ to $SR < 10^{-2}$ (in SR Regime-II), the Young's modulus and yield stress remain initially unchanged and increase afterwards. The Poisson's ratio shows a monotonically decreasing trend. However, the values of flow stress and toughness increases drastically with strain rate. Therefore, we refer to the strain rate value of 10^{-5} as "lower critical SR" beyond which the trends in variation of mechanical properties is different, and changes in the deformation processes are also observed (explained in Section 4.3.2.1).

For strain rates beyond the value of 10^{-3} ($\geq 10^{8}s^{-1}$ in SI unit, in SR Regime-III), the mechanical properties change in an entirely different way compared to the SR regime II. In this SR regime-III, the increment in the Young's modulus and decrement in the Poisson's ratio are more significant compared to the SR regime I and II. Moreover, the yielding and flow behaviors are neither seen in the stress-strain diagrams (see Section 4.3.2.1) nor observed from the visual analysis that is dealt in Section 4.3.2.1. Therefore, the yield and flow stress are not analyzed in this SR regime. Toughness of the models increases continuously in this strain rate regime-III; however, the increase is less significant compared to SR regime-II. From the visual analysis carried out in the latter section, it is found that this mechanical behavior is primarily due to the debonding and slipping of the platelets in the matrix and there is no nucleation of dislocation. Thus, this variation in mechanical properties and deformation processes are quite different compared to the SR regime II. Therefore, the strain rate value of 10^{-2} is referred to as the "upper critical SR".

Most of the MD studies available in literature on the effects of strain rates have mainly focused on the strain rates from $\approx 10^{7}$ to $10^{9}s^{-1}$ in SI unit (corresponding to 10^{-4} to 10^{-2} in reduced unit, in SR Regime-II). This could be the reason why the conclusion that the mechanical properties, such as Young's modulus, yield stress and flow stress, increase with the strain rates was arrived at by many researchers, for ex-

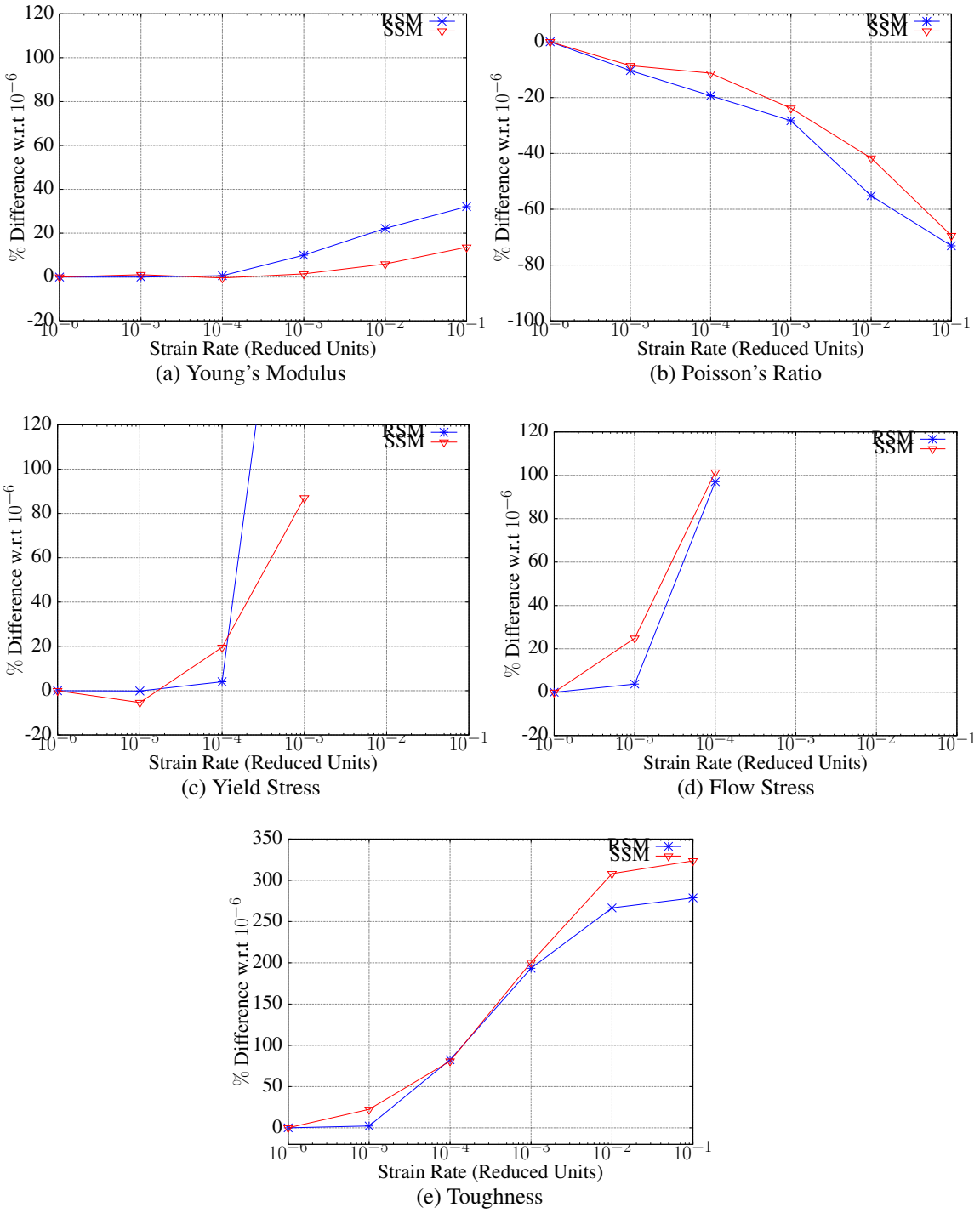

Figure 4.7 Variation of percentage difference in: (a) Young's modulus, (b) Poisson's ratio, (c) yield stress, (d) flow stress and (e) toughness under isothermal uniaxial tensile loading. Note that the yield and flow stress are not plotted for higher strain rates, because there are no yielding and flow behavior observed in the corresponding stress-strain diagrams (refer Fig 4.6a and Fig 4.6b).

ample Huang et al. (2011). In contrast, the present study conducted at many orders of strain rate ($10^6\ s^{-1}$ – $10^{11}\ s^{-1}$) reveal the full spectrum of influence of strain rate on the mechanical properties. MD simulations of Platinum nanowires had shown a 20% reduction in Poisson's ratio, when there is one order of magnitude increase in the strain rate (Koh et al., 2005). Moreover, in their study (Koh et al., 2005), the value of Poisson's ratio at lower strain rates were comparable to the bulk materials, and reduces by a large amount at higher strain rates. MD simulations of our nanocomposite models also predict a similar behavior in the Poisson's Ratio.

A critical strain rate has also been reported for nano-crystalline copper below which the effect of strain rate on the stress-strain curve becomes less pronounced (Schiøtz et al., 1999). This critical strain rate is similar to the lower critical strain rate observed in our MD simulations of nanocomposites. Similar to the present study, the increase in the yield stress with strain rate is found in the MD study on nanocrystalline materials by Vo et al. (2008, 2009). In the study of strain rate effect on single crystal iron, a 35% increase in flow stress is reported (Tang and Marian, 2014). Similarly, the nanocrystalline Al has shown a 14% increase in the yield stress when the strain rate is increased by one order of magnitude (Brandl et al., 2009). Moreover, the drastic increase of mechanical properties for SR $\geq 10^{-2}$ ($\approx 10^{10}\ s^{-1}$, in SI unit) is reported in many MD studies on metallic nanowires (Park and Zimmerman, 2005; Ikeda et al., 1999). The present study also captures the trend of increase in mechanical properties with strain rate. Moreover, the study on nanowires by Wen et al. (2008) has shown the existence of two critical strain rates associated with different deformation mechanisms. In the present study, such deformation mechanisms associated with different strain rates are analyzed in the following subsection.

Visual analysis The visual analysis of deformation processes is carried out in this section. This analysis brings out the fundamental mechanisms underlying the effect of strain rates. We discuss the deformation mechanisms observed at different strain rates for both the RSM and SSM models. The lattice defects during deformation are captured using the centrosymmetry parameter (CSP), as explained in Section 4.3.1. When the value of the CSP of an atom is other than zero, it indicates a defect. Figs 4.8 to 4.11 show different deformation processes occurring at different strain rates of 10^{-5}, 10^{-4} and

10^{-2} for the RSM model. These are representative strain rates chosen for each of the SR regimes discussed previously. For the SSM model (refer Fig 2.2), similar deformation processes are observed for the same values of strain rates. In all the figures shown, blue color denotes matrix, red color denotes platelet and light green color indicates defects in the crystal structure.

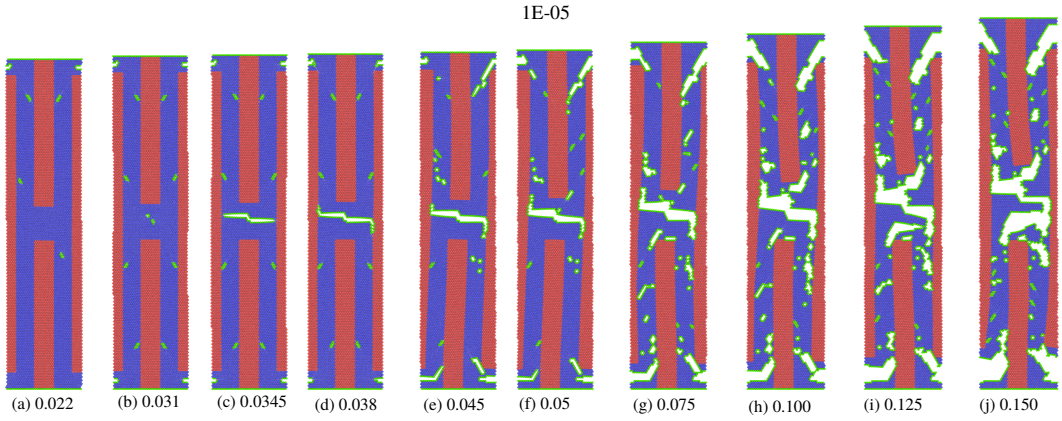

Figure 4.8 Deformation at various values of strain for $\dot{\varepsilon}_{yy} = 10^{-5}$ ($\approx 10^{7}s^{-1}$ in SI unit) for RSM model under isothermal uniaxial tensile loading. Color coding of atoms is as follows: atoms of matrix and platelets are given blue and red colors respectively, and the atoms which are part of defects are given green color. Note: though various defects are observed, amorphous region is not observed at any value of strain.

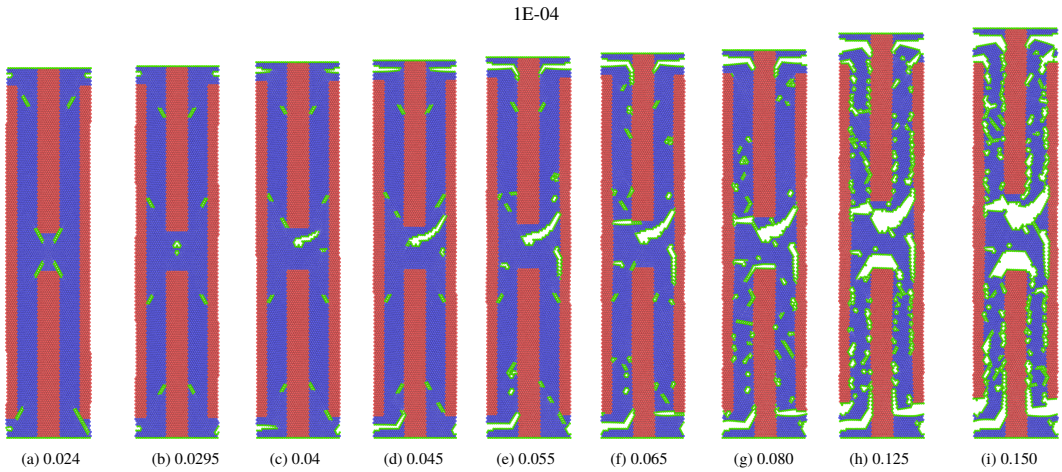

Figure 4.9 Deformation at various values of strain for $\dot{\varepsilon}_{yy} = 10^{-4}$ ($\approx 10^{8}s^{-1}$ in SI unit) for RSM model under isothermal uniaxial tensile loading. Note: for strains > 0.08, a small amorphous region is observed.

We can observe from the Fig 4.8 that defects, such as dislocations and voids, are observed enormously in the soft constituent, the matrix. In contrast, the hard constituent (the platelet) does not exhibit any defects. The crystalline structure is maintained in the

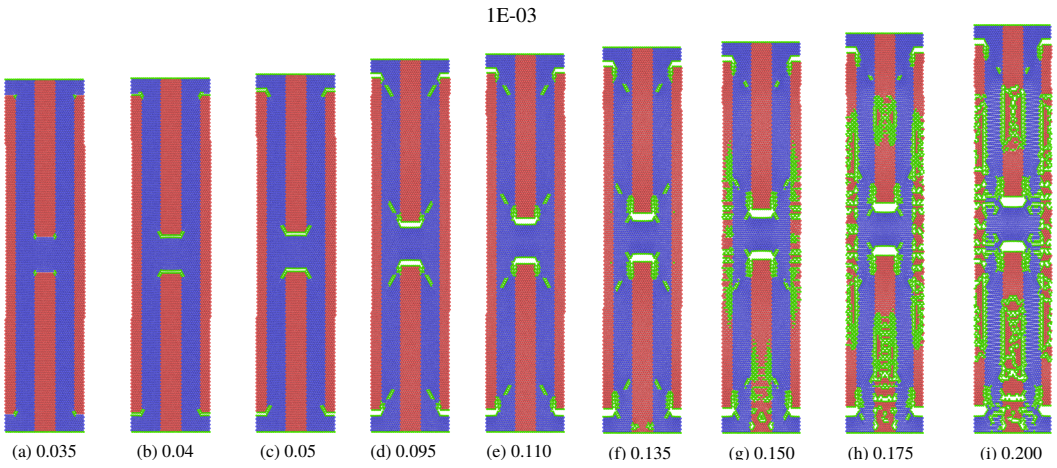

Figure 4.10 Deformation at various values of strain for $\dot{\varepsilon}_{yy} = 10^{-3}$ ($\approx 10^{9} s^{-1}$ in SI unit) for RSM model under isothermal uniaxial tensile loading. Note: amorphous region increases in the matrix.

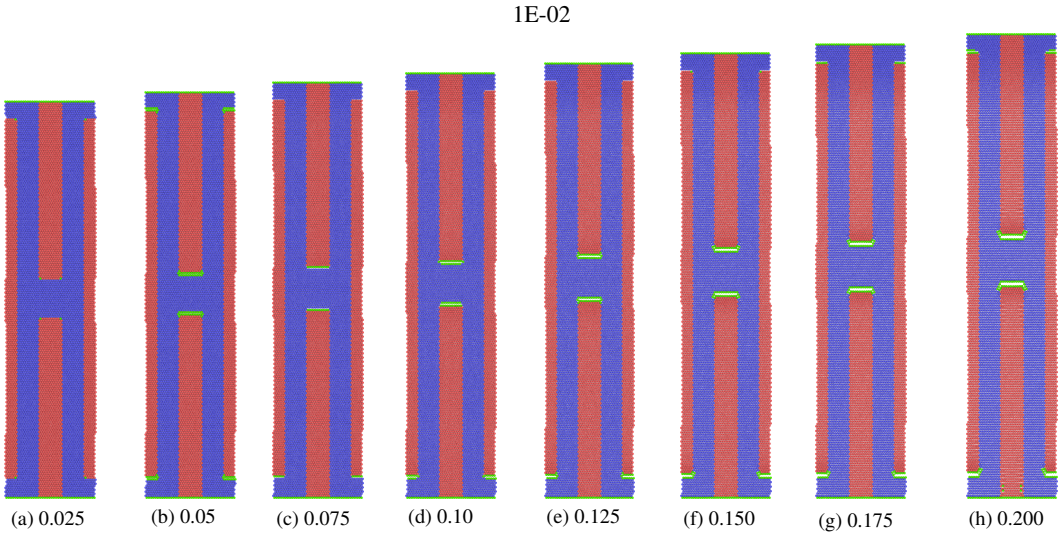

Figure 4.11 Deformation at various values of strain for $\dot{\varepsilon}_{yy} = 10^{-2}$ ($\approx 10^{10} s^{-1}$ in SI unit) for RSM model under isothermal uniaxial tensile loading. Note: no dislocations are emitted; instead, debonding and slipping are observed at the interface.

hard platelet up to the complete failure of the model. Therefore, we focus our attention only to the matrix region. For the strain rate of 10^{-5} ($\approx 10^{7}s^{-1}$ in SI unit), though some dislocations, voids and cracks are observed in the matrix, the matrix maintains its crystalline structure (refer Fig 4.8). However, for higher strain rates of 10^{-4} and 10^{-3} (refer Figs 4.9 and 4.10), the defects similar to that observed in SR Regime I are seen in the matrix initially. However, an amorphous structure is observed in the matrix in the later stages of the deformation.

Deformation processes at a high strain rate of 10^{-2} ($\approx 10^{10}s^{-1}$ in SI unit) is shown Fig 4.11. Contrary to the deformation mechanisms observed at lower strain rates, the emission of dislocations is not observed at this higher strain rate. Moreover, the platelets begin to slip. Previous MD studies at higher strain rates have shown transformation of gold nanowires into single-atom chain (Park and Zimmerman, 2005) and crystalline nanowires into amorphous structure at the SR of $5 \times 10^{10}s^{-1}$ (Ikeda et al., 1999). In contrast, our study on nanocomposite shows slipping of platelets at SR $\geq 10^{-2}$ ($\approx 10^{10}s^{-1}$ in SI unit). We refer to this phenomenon as the debonding and slipping mechanism.

In our simulations, at low strain rates, the low energy defects such as dislocations are activated, which is observed by other researchers as well (Pu et al., 2008). However in our nanocomposite models, the dislocations are observed only in the matrix; this is mainly because matrix requires low energy for the dislocation activities compared to the platelet. At higher strain rates, high energy defects such as amorphization, and debonding and slipping are observed in our models. Branício and Rino (2000) and Ikeda et al. (1999) have observed amorphization-like deformation at higher strain rates. However, in our MD simulations of nanocomposites, only the matrix region undergoes amorphization-like deformation. This could be because the matrix region is loaded more critically than the platelets.

Thus, MD simulations reveal various deformation mechanisms occurring in the nanocomposite materials at different values of strain rates. Although the mechanical properties are higher at higher strain rates, the amorphization of the matrix phase, and the debonding and slipping of the platelets could lead to undesirable material deterioration. Further, the model nanocomposite could maintain a crystalline deformation both in the matrix and the platelets when the strain rate is below the lower critical strain rate as defined above. This type of deformation is more close to practically observed defor-

mation mechanisms. Strain rate in this strain rate regime is used for other analyses in later chapters.

Moreover, from this section, we observe that the different nanostructure arrangements do not play significant role in the change in the deformation processes with strain rate. Therefore in the following subsections, we study the influence of strain rate only for the RSM model for the adiabatic uniaxial tensile loading and adiabatic shock wave loading.

4.3.2.2 Adiabatic uniaxial tensile loadings

Adiabatic uniaxial tensile loading is conducted to investigate the effect of strain rate and consequent increase in the temperature on the mechanical response. Here, the temperature of the system is allowed to change depending on the internal deformation mechanisms. And, the uniaxial tensile stress state is maintained along the platelet length direction during the simulation of tensile loading. For this purpose, Berendsen barostat is used to maintain the global stresses zero in the direction normal to the loading direction. In the following subsections, the effect of strain rate on mechanical response during adiabatic uniaxial tensile loading is examined.

Variation in stress-strain diagram As discussed earlier, the influence of strain rate on the adiabatic uniaxial tensile loadings is analyzed only for RSM model since the nanostructure does not seem to play a significant role in these strain rate studies. Fig 4.12a shows the stress-strain curves obtained for the RSM model for different values of strain rates. Figs 4.12b and 4.12c show the variation of PE and KE for RSM model for different strain rates. The variation of PE and KE for different values of strain rates is similar to that observed for stress-strain curves. Three strain rate regimes are observed which are similar to that observed in the isothermal uniaxial tensile test simulations.

Under adiabatic condition, the strain rate regimes can be classified as follows, i.e.,
1) SR $\leq 10^{-4}$ ($\leq 10^{8} s^{-1}$ in SI unit): The stress-strain diagram shows a zigzag nature. This range of strain rates is referred to as the SR Regime-I.
2) SR $\geq 10^{-1}$ ($\geq 10^{11} s^{-1}$ in SI unit): A drastic increase in the magnitude of stress occurs compared to SR $< 10^{-1}$. This range of strain rates is referred to as the SR

Regime-III.

3) SR of 10^{-3} to 10^{-2} ($10^{8} < SR < 10^{11}$ s^{-1} in SI unit): The variations in stress do not show any characteristics as observed in SR Regime-I or SR Regime III. This range of strain rates is referred to as the SR Regime-II.

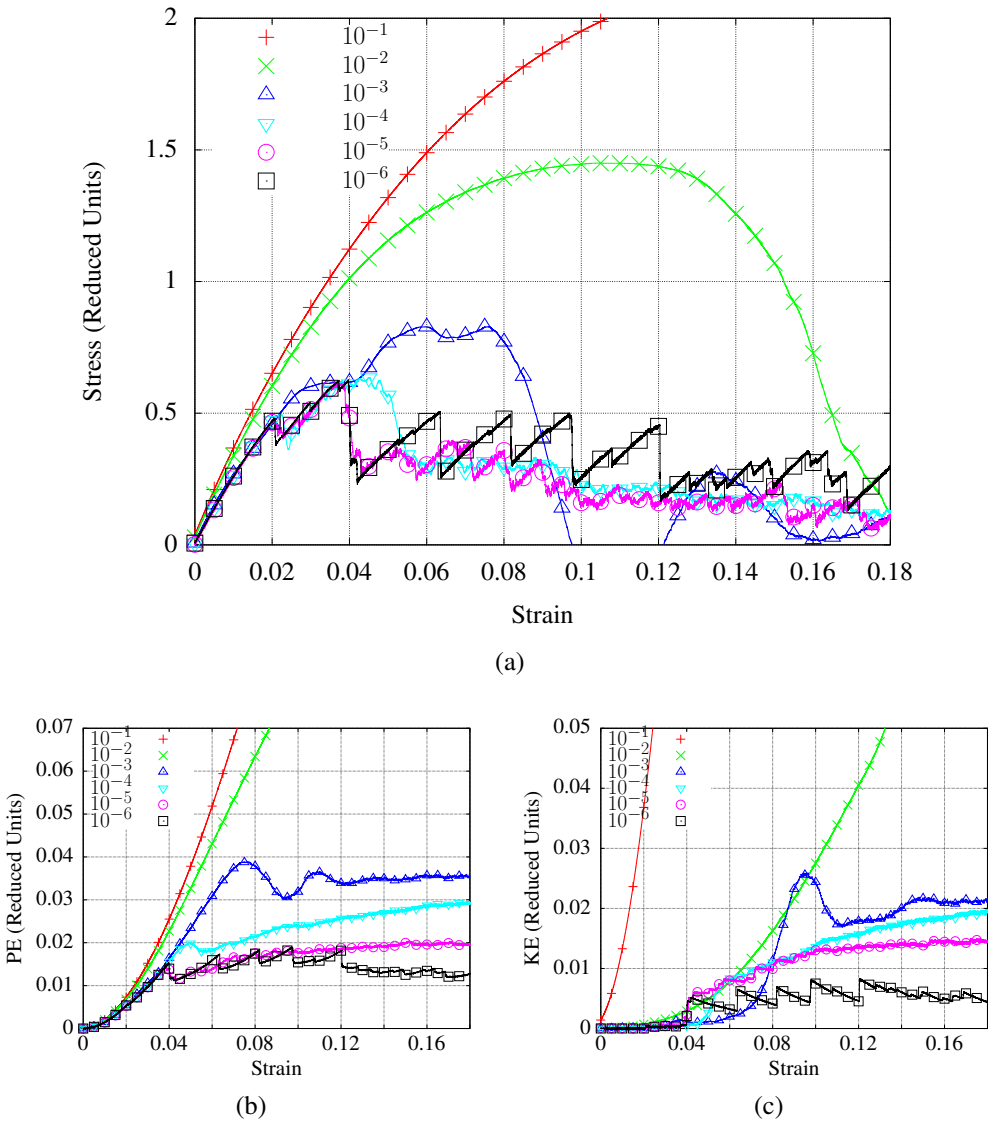

Figure 4.12 Influence of strain rate under adiabatic uniaxial tensile loading on (a) stress-strain diagram, (b) PE-strain diagram, and (c) KE-strain diagram of the RSM model. The strain rates shown are in reduced units.

Compared to the isothermal stress-strain diagram, significant reduction in stress values are observed for the corresponding strain rates under the adiabatic stress-strain diagrams. This could be mainly due to the thermal softening occurring in the model as a result of increase in the temperature of the model. Moreover, it is also to be noted here

that similar to the case of homogeneous model studied in the Section 4.3.1, the KE of the system increases with strain from the zero-strain for SR $\geq 10^{-2}$. This increase in KE is mainly attributed to the applied strain rate is approaching the vibrational frequency of the system i.e., $\nu_{matrix} = 0.38$ (see the discussion in Section 4.3.1).

For deformations at low strain rates ($< 10^{-2}$, including both the SR regime-I and SR regime-II), the KE starts increasing only after a strain around 0.02. At this strain, visual analysis shows the emission of dislocations (the results of visual analysis is explained in Section 4.3.2.2). These dislocations increase the KE. It is also to be noted here that the increase in temperature at the onset of plastic deformation, also known as plastic heating, is a well-known phenomenon observed in the experiments done by Kapoor and Nemat-Nasser (1998) and Rittel et al. (2012). This plastic heating phenomenon is also captured in many MD simulations, such as in Al nanocrystals studied by Munilla et al. (2009) and nanoporous bcc metals by Ruestes et al. (2014). Due to the absence of thermal dissipation in the present MD simulation, the increase in KE during the initiation of plastic deformation due to nucleation of dislocations is captured. Further, the amount non-crystalline deformation (measured as equivalent to the amount of KE evolved) in the SR Regime-II is higher compared to that of the SR Regime-I. From the visual analysis of the deformed structure discussed in Section 4.3.2.2, it is seen that the KE evolution is due to generation of dislocations for SR Regime I and amorphous deformation for SR Regimes II. Further discussion about the visual analysis of the deformed structure is done in the following subsection.

Visual analysis Different deformation processes for the RSM model occurring at different strain rates of 10^{-4}, 10^{-3}, 10^{-2} and 10^{-1} are shown in Figs 4.13 to 4.16 respectively. These strain rates are chosen as a typical example in each of the SR regimes discussed previously. In all the deformation figures, blue color denotes matrix, red color denotes platelet and light green color shows defects in the crystal structure.

The basic deformation processes observed in this analysis is similar to that in the isothermal uniaxial tensile loadings. Defects, such as dislocations and voids, are observed enormously in the soft constituent matrix, and the hard constituent platelets do not exhibit any defects. The crystalline structure is maintained in the hard platelet up to the complete failure of the model. Below the strain rate of 10^{-4}, the matrix maintains

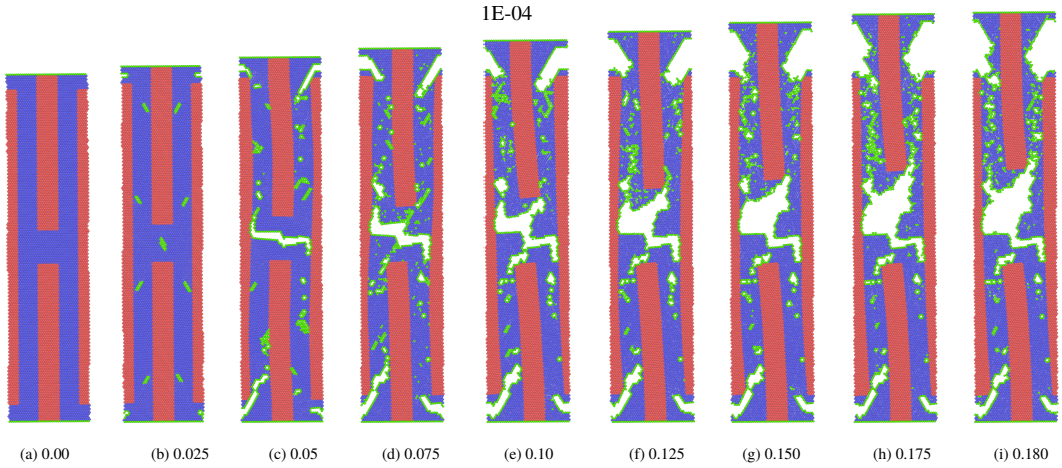

Figure 4.13 Deformation at various values of strain for $\dot{\varepsilon}_{yy} = 10^{-4}$ ($\approx 10^{8} s^{-1}$ in SI unit) for RSM model under adiabatic uniaxial tensile loading. Note: at the strain value of 0.15, a small amount of amorphous region is observed.

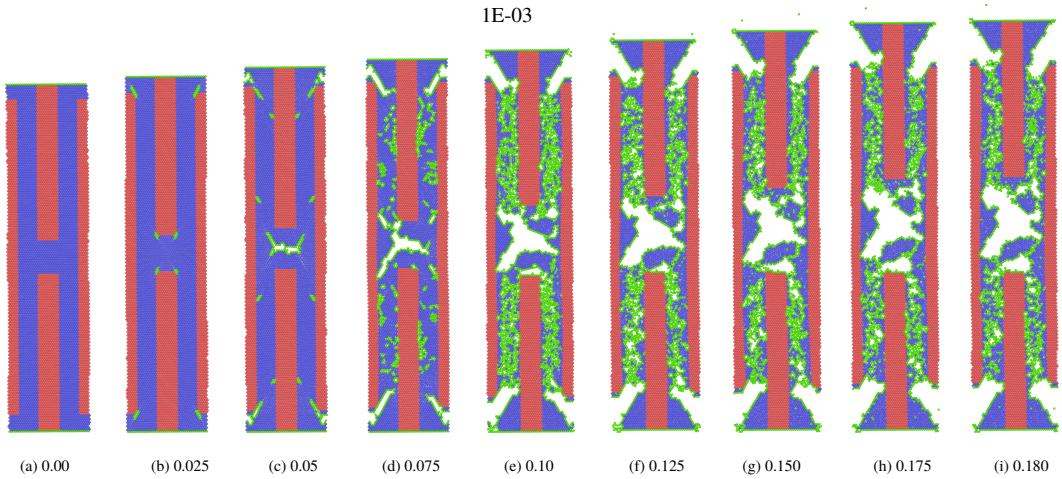

Figure 4.14 Deformation at various values of strain for $\dot{\varepsilon}_{yy} = 10^{-3}$ ($\approx 10^{9} s^{-1}$ in SI unit) for RSM model under adiabatic uniaxial tensile loading. Note: amorphous region increases in the matrix

its crystalline structure along with defects (refer Fig 4.13). However, further increase of the strain rate from 10^{-3} to 10^{-2} (refer Figs 4.14 and 4.15) leads to an amorphous structure in the matrix (refer Fig 4.12c). Moreover, it could lead to the melting of the material. At high strain rates $\geq 10^{-1}$ (refer Fig 4.16), the platelets begin to slip similar to the previous studies.

4.3.2.3 Adiabatic shock wave loadings

During the high rate planar shock wave loadings, the uniaxial strain condition occurs in the model (Luo et al., 2006). The uniaxial strain condition implies that the strain is

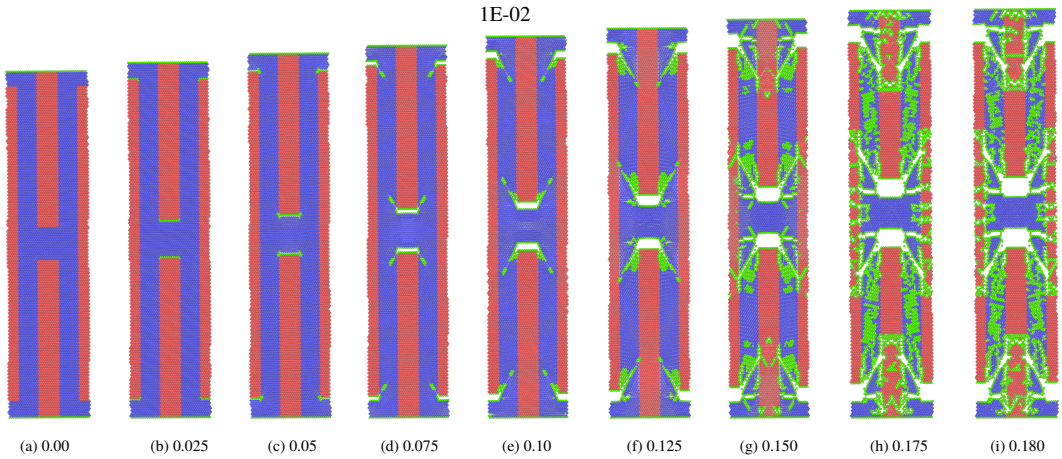

Figure 4.15 Deformation at various values of strain for $\dot{\varepsilon}_{yy} = 10^{-2}$ ($\approx 10^{10} s^{-1}$ in SI unit) for RSM model under adiabatic uniaxial tensile loading. Note: no dislocations are emitted; instead, amorphous structure as well as debonding and slipping are observed

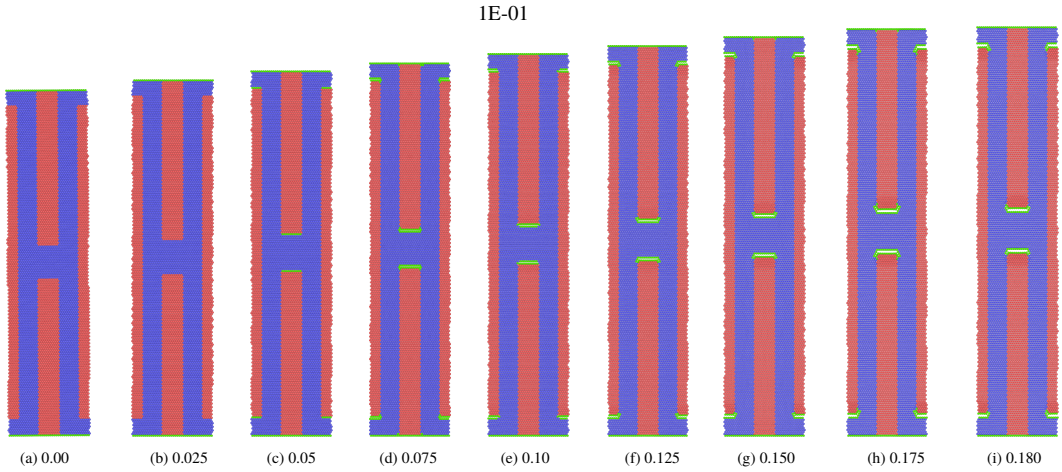

Figure 4.16 Deformation at various values of strain for $\dot{\varepsilon}_{yy} = 10^{-1}$ ($\approx 10^{11} s^{-1}$ in SI unit) for RSM model under adiabatic uniaxial tensile loading. Note: no dislocations are emitted; instead, debonding and slipping are observed

allowed to increase only in the loading direction and zero strain is maintained in all other directions. Moreover, the heat transfer also does not take place with the surrounding. Therefore in this section, temperature of the system is allowed to change depending on the internal deformation mechanisms. This means that no constraints on the state variables of the atomistic system are applied. In the following subsections, the effect of strain rate on MD simulation of the adiabatic shock wave loading condition is explored.

Variation in stress, PE and KE As discussed earlier, the influence of strain rate on the adiabatic shock wave loadings are analyzed only for RSM model since the nanostructure does not seem to play a significant role in these strain rate studies. Fig 4.17a shows the obtained stress-strain curves for the RSM model for different values of strain rates. Figs 4.17b and 4.17c shows the variation of PE and KE for RSM model for different strain rates. The variation of PE and KE for different values of strain rates is similar to that observed for stress-strain curves. Three strain rate regimes are observed which are similar to that observed in the adiabatic uniaxial tensile test simulations.

Visual analysis The basic deformation processes observed in this analysis is similar to that observed in the uniaxial tensile loadings. Defects, such as dislocations and voids, are observed enormously in the soft constituent matrix and the hard constituent platelets do not exhibit any defects. The crystalline structure is maintained in the hard platelet up to the complete failure of the model. Below the strain rate of 10^{-4}, the matrix maintains its crystalline structure along with defects (refer Fig 4.18). However, further increase of the strain rate from 10^{-3} to 10^{-2} (refer Figs 4.19 and 4.20) leads to amorphous structure in the matrix (refer Fig 4.17c). At a high strain rate of 10^{-1} (refer Fig 4.21), the platelets begin to slip similar to the previous studies.

Thus, the influence of strain rate is explored in isothermal and adiabatic tensile loadings as well as under "uniaxial stress" and "uniaxial strain" conditions. The comparison between the isothermal (Section 4.3.2.1) and adiabatic loadings (Section 4.3.2.2) leads to the conclusion that the lower and upper critical strain rates for isothermal loading (10^{-5} and 10^{-2}) are one order of magnitude lower than that of the critical strain rates of adiabatic loading (10^{-4} and 10^{-1}). Further, the comparison of uniaxial stress (Section 4.3.2.2) and uniaxial strain (Section 4.3.2.3) conditions also means that the

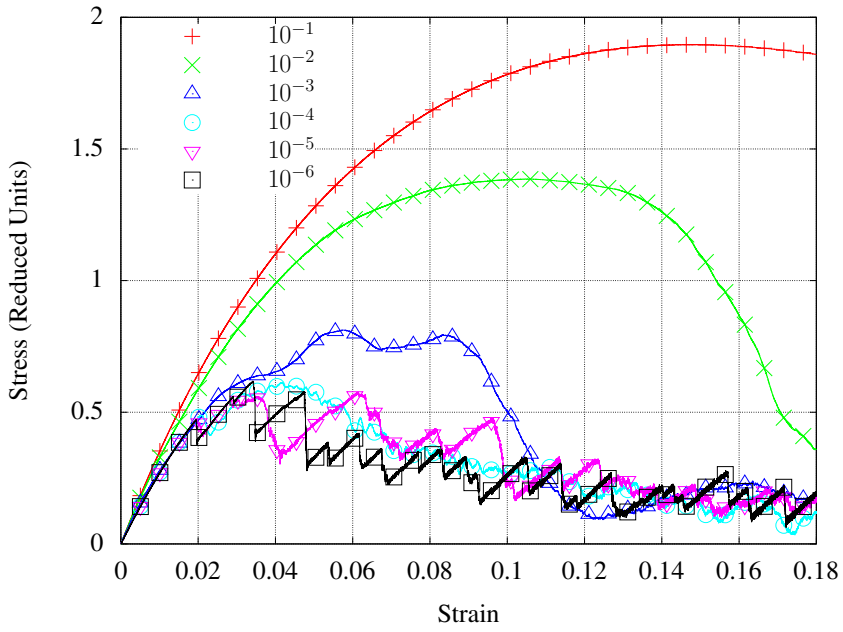

(a)

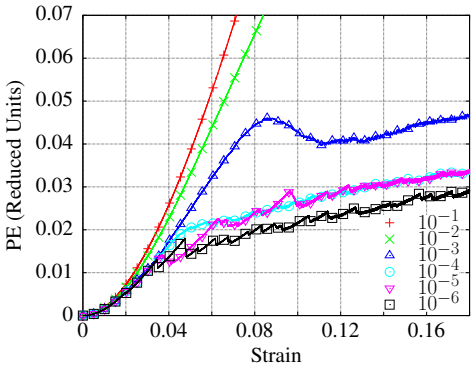

(b)

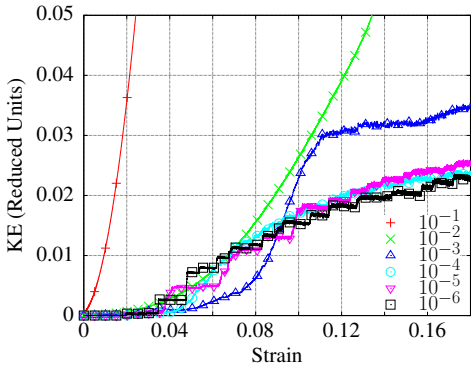

(c)

Figure 4.17 Influence of strain rate under adiabatic shock wave loading on (a) stress-strain diagram, (b) PE-strain diagram and (c) KE-strain diagram of the RSM model nanocomposite. The strain rates shown are in reduced units.

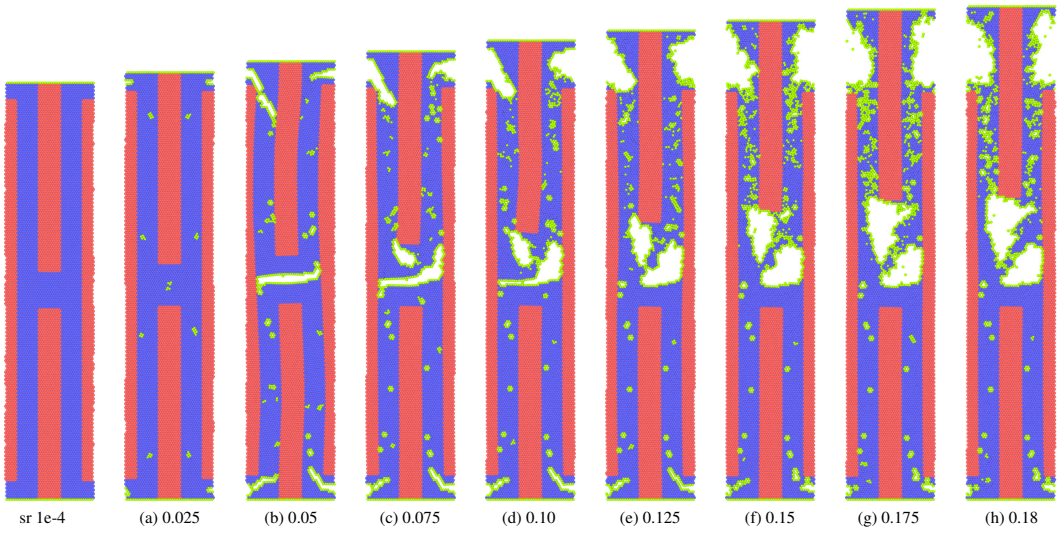

Figure 4.18 Deformation at various values of strain for $\dot{\varepsilon}_{yy} = 10^{-4}$ ($\approx 10^{8} s^{-1}$ in SI unit) for RSM model under adiabatic shock wave loading. Note: at the strain value of 0.15, a small amount of amorphous region is observed.

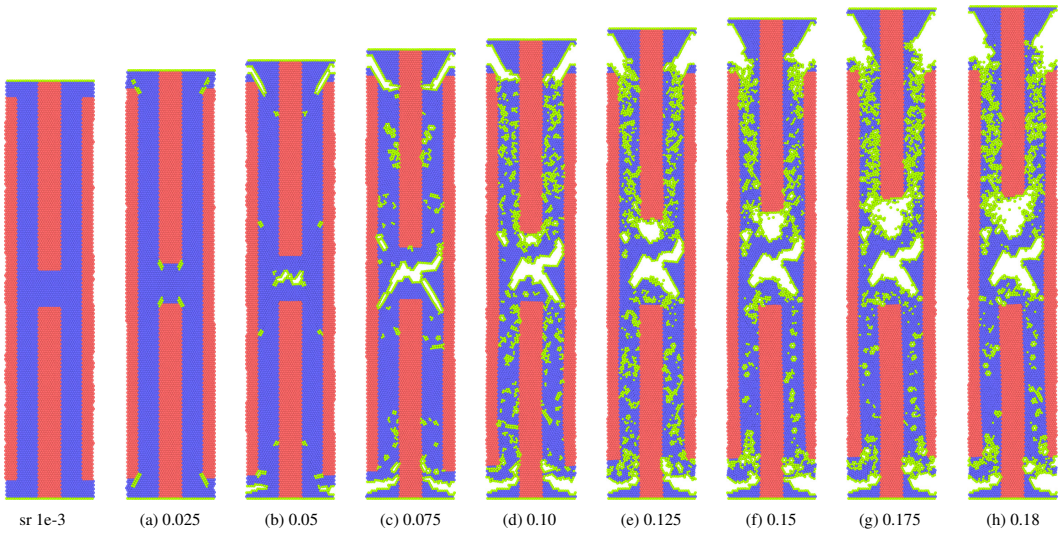

Figure 4.19 Deformation at various values of strain for $\dot{\varepsilon}_{yy} = 10^{-3}$ ($\approx 10^{9} s^{-1}$ in SI unit) for RSM model under adiabatic shock wave loading. Note: amorphous region increases in the matrix

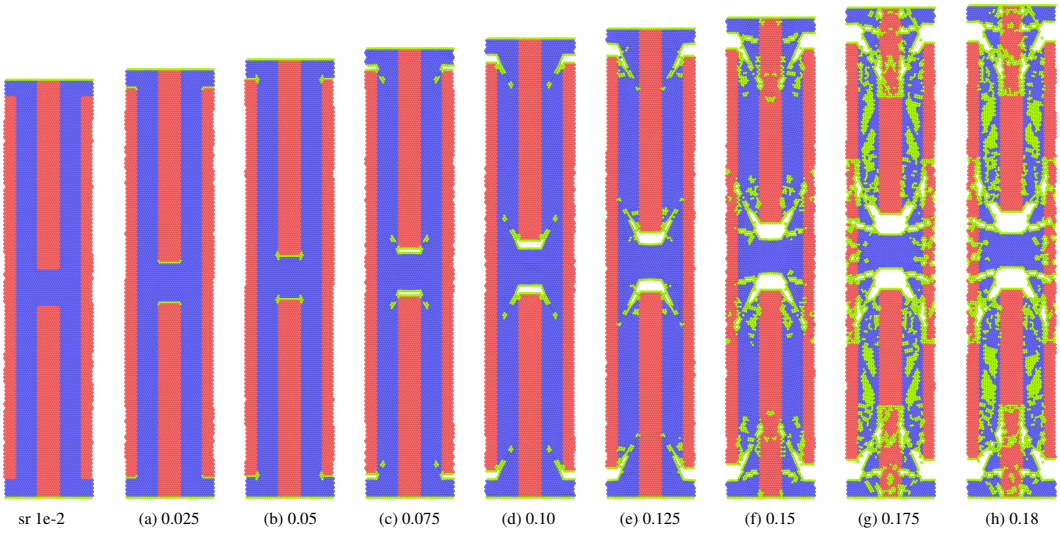

Figure 4.20 Deformation at various values of strain for $\dot{\varepsilon}_{yy} = 10^{-2}$ ($\approx 10^{10} s^{-1}$ in SI unit) for RSM model under adiabatic shock wave loading. Note: no dislocations are emitted; instead, amorphous structure as well as debonding and slipping are observed.

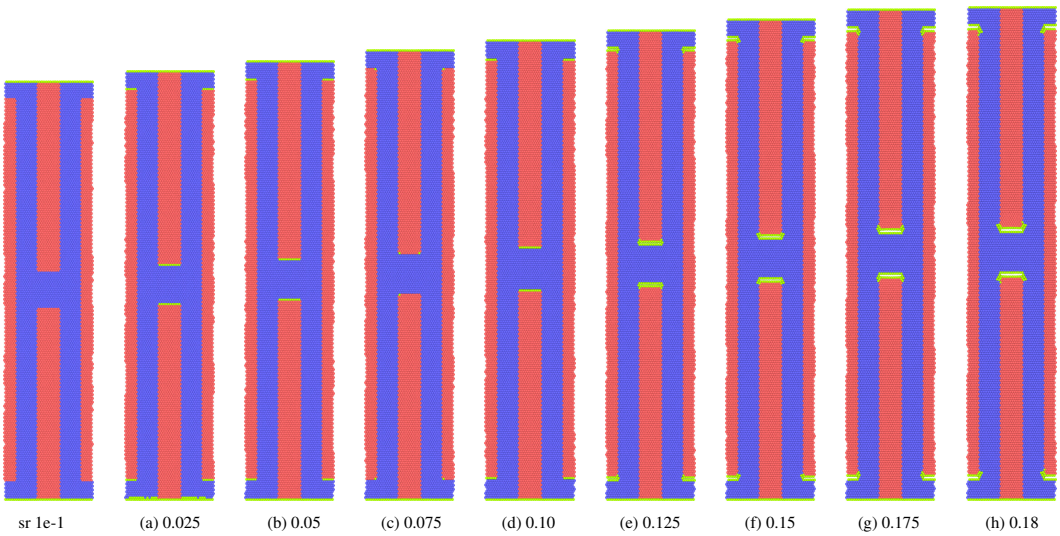

Figure 4.21 Deformation at various values of strain for $\dot{\varepsilon}_{yy} = 10^{-1}$ ($\approx 10^{11} s^{-1}$ in SI unit) for RSM model under adiabatic shock wave loading. Note: no dislocations are emitted; instead, debonding and slipping are observed

comparison is between analyses with and without the consideration of Poisson effect. Therefore, by comparing the Section 4.3.2.2 and Section 4.3.2.3, we observe that the Poisson effect does not play significant role in the study of the influence of strain rate. However, the two critical strain rates and three strain rate regimes are observed in all the cases studied.

4.3.3 Comparison between Homogeneous and Nanocomposites

In this section, we compare the mechanical behavior of homogeneous and nanocomposite models when subjected to different strain rates. In the homogeneous model, no significant deviation is observed in the stress-strain curves with strain rate. However, in the nanocomposites, there exist significant differences between stress-strain curves for different values of strain rate. The homogeneous model shows different deformation mechanisms for different strain rates. These include dislocation dominated, amorphous, and non-relaxing mechanisms associated with the plasticity of the homogeneous model.

In contrast, for the nanocomposites, plasticity occurs mainly in the soft phase; moreover, a range of entirely different deformation mechanisms are observed: (i) dislocation dominated, (ii) amorphous, and (iii) debonding and slipping mechanisms. Further, from the comparison between the different nanostructures of the nanocomposites such as RSM and SSM models, we find that the nature of structural arrangement does not affect the deformation mechanism. This suggests that the deformation mechanisms may remain unaffected by the variation in the type of platelet arrangement in the nanocomposite.

We have used two dimensional Lennard-Jones solids with hexagonal crystal structures for building our nanocomposite models. The 2D models are advantageous for carrying out simulations with large number of atoms and for longer duration. Though the 2D models consider only one layer of atoms and the interactions of atoms in the out of plane directions are ignored, the 2D models indeed reproduce basic deformation mechanisms observed in 3D models, which is discussed in Section 3.3 . Moreover, it is also to be noted here that the condition maintained in 2D models is similar to the plane strain condition used in the continuum mechanics theories (Sadd, 2009).

4.4 Conclusion

In this chapter, molecular dynamics is used to carry out computational uniaxial tensile tests at different strain rates on the homogeneous and bio-inspired nanocomposite structures made of 2D LJ crystals. The influence of strain rate on the mechanical behavior of these nanocomposites is studied through (i) the analysis of the variation of stress, potential energy and kinetic energy, (ii) the analysis of the variation of mechanical properties such as Young's modulus, Poisson's ratio, yield stress, flow stress and toughness as well as (iii) the visual analysis of deformation mechanisms. Moreover, the effects of strain rate on the adiabatic loading condition as well as planar shock wave loading condition are also explored. From the results discussed, the following conclusions can be drawn.

For homogeneous model, there is no significant change in the mechanical properties due to different strain rates. However, the homogeneous model exhibit dislocation dominated plastic deformation at lower strain rates, and amorphous and non-relaxing deformations at higher strain rates. These deformation mechanisms are observed only for a very small range of strain close to the failure strain. Therefore, homogeneous 2D LJ solid is considered as a brittle material. Whereas, for nanocomposite models, there exist three strain rate regimes which are separated by two critical strain rates as follows: At lower strain rates (strain rate regime-I), the values of yield stress, flow stress, and toughness increase with strain rates and the occurrence of plasticity is primarily due to the generation of dislocations on the soft constituent. At higher strain rates (strain rate regime-III), the yielding and flow behavior are not observed, but high toughness is observed. This behavior is due to the deformation mechanisms being the debonding and slipping of the platelets. In between these two regimes, a transition region or strain rate regime-II is observed, where the soft phase undergoes amorphous deformation. Further, it is observed that the critical strain rates are increased by one order of magnitude for adiabatic loading compared to isothermal loading under uniaxial stress condition. Similarly, the reduction in critical strain rates is observed for shock wave loadings compared to the isothermal uniaxial tensile tests. We have also shown that the inclusion of Poisson effect does not significantly influence the deformation mechanisms in these nanocomposites.

Moreover, these nanocomposite materials show large amount of plastic deforma-

tion for large strain levels, though the nanocomposites are made of brittle constituents. Therefore, nanocomposites materials made of brittle materials like ceramics could lead to a good amount of ductility and toughness. These studies enhance our knowledge in the deformation mechanisms of bio-inspired nanocomposites and could help in building advanced engineering materials. Moreover, these findings would lay the ground work for more computational and physical experiments on the bio-inspired nanocomposites.

CHAPTER 5

Effect of Aspect Ratio of Platelets

In this chapter, the effect of aspect ratio (AR) of platelets on the overall mechanical behavior of bio-inspired brittle-matrix nanocomposites is investigated. The AR of platelets is varied for both the regularly staggered model (RSM) and stair-wise staggered model (SSM); the resulting variation in Young's modulus, critical stress, flow stress, and toughness as well as variation in deformation mechanisms are analyzed using molecular dynamics (MD) simulations. The results of MD simulations agree closely with the available theories of Young's modulus. Further, the results obtained for the strength of the regularly staggered model agree with the strength theory available in literature. However, the results of the stair-wise staggered model show a significant difference; the reason for this is examined further. We demonstrate the existence of two critical AR's for the stair-wise staggered model: i) a smaller critical AR above which platelet fracture occurs, ii) another higher critical AR above which composite strength remains constant. Further, MD simulations show that the pull-out occurs for platelet AR lower than the critical AR and platelet fractures for a higher AR. The pull-out mechanism acts as a major source of plasticity and energy absorbing mechanism of these nanocomposites. Further, it is found that i) the regularly staggered model is efficient in achieving a combination of high Young's modulus, flow strength and toughness, and ii) the stair-wise staggered model is efficient in achieving high Young's modulus and tensile strength.

5.1 Introduction

The aspect ratio (AR) of platelets plays a major role in achieving superior mechanical properties in platelet-matrix composites. There is a need to choose an optimal AR to achieve a unique combination of superior mechanical properties. Numerous research works have been carried out to understand the influence of aspect ratio of platelets on the overall mechanical properties of these composites. Specifically, the effect of geometrical parameters on the staggered-platelets-matrix composites has been studied

analytically in two ways: 1) Based on the theories developed for short fiber reinforced composites (SFRC) such as shear-lag analysis (SLA) and 2) Based on tension-shear chain (TSC) model (Anup et al., 2007; Dutta et al., 2013; Hsueh, 1994; Jager and Fratzl, 2000; Ji and Gao, 2004; Ji, 2008; Kotha and Guzelsu, 2000; Kotha et al., 2000; Su et al., 2012; Wei et al., 2012; Zhang et al., 2010). These analytical solutions are very powerful for providing the relationship between the overall composite mechanical properties and the geometrical, material properties of constituents. However, these models are based on some restrictive assumptions which lead to a lack of incorporation of actual complex behavior of the constituents, such as inelasticity, anisotropicity and/or viscoelasticity. Moreover, the non-continuum nature of material at the nanoscale is also not taken into consideration.

Often the mechanical properties of composites are calculated by studying stress transfer between a fiber and the matrix. Using the stress transfer analysis, a varying amount of stress that is transferred to the fiber from the matrix at different points in the fiber–matrix interface is calculated. The simplest model, often used to obtain stress distribution of discontinuous fiber reinforced composites, is the Cox's classical shear–lag analysis (H.L.Cox, 1952), which has the following assumptions; (1) the fiber and matrix remain elastic in their mechanical response, (2) the interface between the two components is perfect, and (3) no axial load is transmitted through the fiber ends. It is to be noted that the predictions based on the Cox's model are limited to low volume fraction of fibers and low value of applied strains ($< 0.5\%$) (Robinson and Robinson, 1994). Moreover, the importance of "critical fiber length" concept which describes the length necessary to build up a certain stress level in the fiber is developed from this theory. Thus, the central problem with the load-bearing properties of short fiber composites is the load transfer from the surrounding matrix to the reinforcing fibers (Piggott, 2002; Fu et al., 2009).

Kelly and Tyson (1965) proposed a model with plastic behavior around the fibers by assuming constant shear stress along the interface. Such an assumption of a constant shear stress implies that these interfaces carry their maximum shear stress even at low applied loads. However, for composites, this will hold true only for loads that nearly achieve the composite strength. Hence, this model is well suited for the case of high loads and hence for strength considerations. In contrast, Cox's model is more suitable at

low loads and hence for stiffness considerations (Piggott, 2002; Fu et al., 2009). Later, Cox's model was extended by many researchers to include the planar reinforcements, fiber to fiber interaction, and so on (Padawer and Beecher, 1970; Lusis et al., 1973; Hull and Clyne, 1996; Nairn, 1997). Recently, Kotha and Guzelsu (2000) studied the mechanical properties of the platelet-matrix composites based on this shear-lag analysis method.

On the other hand, a tension shear chain (TSC) model was developed by Jager and Fratzl (2000) and Gao et al. (2003), particularly to analyze biological nanocomposite materials. In the TSC models, it is assumed that the platelets carry only the tensile stress and the tensile stress between the platelets are transferred by means of shear stress in the matrix. Moreover, the tensile stress transfer between the platelets-to-platelets via the matrix in the axial gap region (axial gap region is shown in Fig 2.2) is ignored; this assumption is mainly applicable to biological nanocomposites where the matrix is three orders of magnitude softer than the platelets. Recently, Zhang et al. (2010) and Lei et al. (2013) have analyzed composites with different platelets distributions in the matrix using the TSC model. They showed that the regularly staggered and stair-wise staggered models have optimal mechanical properties compared to other distributions. They found that there exists a critical AR which separates platelet failure from matrix failure. The strength of the composite increases with AR, reaches a maximum at the critical AR and thereafter remains a constant.

The main objective of a theoretical consideration is the derivation of qualitative or quantitative statements concerning the influence of several parameters (e.g., fiber length and fiber volume fraction), and deformation or failure processes on the general behavior of composites. This will help in the suppression of undesirable damage and optimization of composite parameters.

In this chapter, we study the effect of aspect ratio of platelets on the generic mechanical behavior of the regularly staggered and stair-wise staggered nanocomposites. These nanocomposites are inspired from the nanostructure of biological materials such as nacre, tendon and bone (See Fig 1.2). Computational experiments on these models are conducted using MD simulations, as outlined in Chapter 2. Both the constituents are modeled as brittle materials in order to study the generic behavior of bio-inspired ceramic-ceramic nanocomposites. The effect of aspect ratio (AR) of platelets on over-

all Young's modulus, strength, flow strength and toughness of these models are found out. Results of the MD simulations are compared with analytical models based on TSC models as well as shear-lag based models. The significance of critical aspect ratio with regards to mechanical properties and failure mechanisms are discussed.

5.2 Modeling and Simulation Methodology

The effects of platelet AR on both the RSM and SSM nanocompsite models are studied using MD simulations. The atomistic nanocomposite models are built using the two dimensional Lennard-Jones solids with hexagonal crystal structures as discussed in Chapter 2. Both the models are shown in Fig 2.2. The aspect ratio of platelets is varied by increasing the number of lattice unit cells in the length of the platelet, while the number of atoms in all other dimensions remains constant. The number of atoms in platelet thickness (F), platelet transverse gap (M) and axial gap (G) are maintained as 10. Whereas, the number of atoms in the length of the platelets is varied from 30 to 400 in RSM model and 60 to 1300 in SSM model. This variation in the number of atoms corresponds to an AR of 5 to 70 for RSM model and 10 to 150 for SSM model.

Uniaxial tensile tests are performed for both the RSM and SSM models for different values of aspect ratios. A constant temperature of 0.0001 is maintained through out the simulation using Berendsen thermostat (Berendsen et al., 1984). The stresses normal to the loading directions are maintained zero using Berendsen barostat (Berendsen et al., 1984). A strain rate 10^{-5} is applied in model. More details can be found in Section 2.2. The variation in mechanical properties and the deformation mechanisms are analyzed further.

5.3 Results and Discussions

Uniaxial tensile tests using MD simulations provide data on stress at each increment of strain. The various mechanical properties of nanocomposites are calculated as follows. The Young's modulus is calculated as the initial slope of the stress-strain diagram, critical stress as the maximum stress observed, flow stress as the average stress in the strain range of 8 to 10 % of applied strain and toughness as the area under the stress-strain

curve. More details about the calculation of mechanical properties are explained in Section 2.3.1. The variation of Young's modulus, critical stress (strength), flow strength and toughness of the nanocomposite with respect to change in AR is analyzed further.

5.3.1 Young's Modulus

In this subsection, the effect of platelet AR on the overall Young's modulus of the nanocomposite is investigated. Figs 5.1a and 5.1b show the variation of measured Young's modulus values from the MD simulations for regularly staggered (RSM or N2-SSM) and stair-wise staggered (SSM or N5-SSM) models. It is to be noted here that the N2-SSM & N5-SSM refers to the regularly staggered model and the stair-wise staggered model where the number 2 and 5 refers to the number of platelets in the RVE of the RSM and SSM models respectively. Both the models show an increase in the Young's modulus with aspect ratio. At large aspect ratios, the Young's modulus converges to a constant value. The Young's moduli calculated from the present MD simulations agree with the predictions based on the theories developed for short fiber reinforced composites. This further validates the MD simulations methodology used in the thesis.

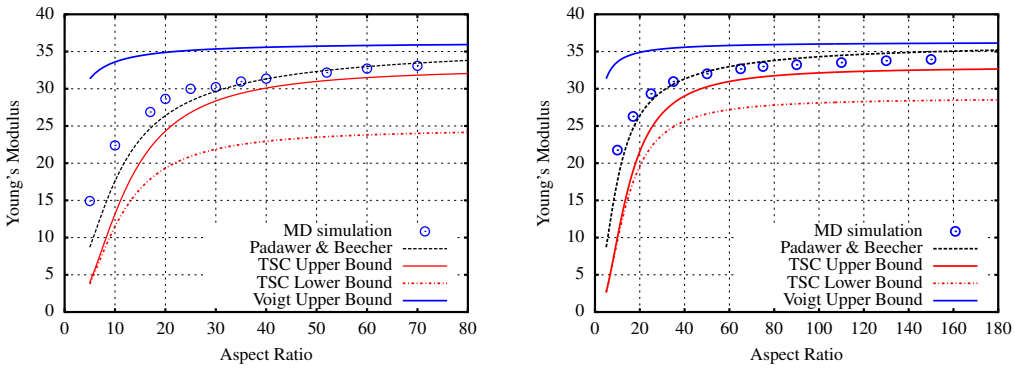

Figure 5.1 Variation of stiffness with aspect ratio for (a) regularly staggered (RSM or N2-SSM) and (b) stair-wise staggered (SSM or N5-SSM) models. The results obtained using MD simulations are compared with analytical theories.

Figs 5.1a and 5.1b show the Young's modulus predicted from Voigt model (Hull and Clyne, 1996), Padawer & Beecher model (Padawer and Beecher, 1970), and lower and upper elastic bounds predicted from TSC model (Lei et al., 2013; Zhang et al.,

2010). Voigt model is developed based on the iso-strain assumption which gives an upper bound of Young's modulus for any composite material (see Figs 5.1a and 5.1b). This model is also known as Rule of Mixtures (ROM) for Young's modulus, and is shown in Eq (5.1) where ϕ refers to the volume fraction of platelet. It is observed from the Figures Figs 5.1a and 5.1b that the both the RSM and SSM models can achieve upper Voigt limit of Young's modulus by increasing the AR of the platelets. The Padawer and Beecher (1970) model is based on shear-lag analysis. In their model, the analytical solution for the Young's modulus of planar-reinforcements in plastic resins was developed by improving the Cox theory, and is shown in Eq (5.2). The present MD results agree with the Padawer and Beecher (1970) model at higher values of AR, but some deviations are found at smaller values of AR. Padawer and Beecher (1970) ignored the interaction between the platelets in their model. This could have caused the deviations at smaller ARs.

$$E_{Voigt} = \phi E_p + (1-\phi)E_m \tag{5.1}$$

$$E_{PB} = \phi E_p \left(1 - \frac{\tanh(u)}{u}\right) + (1-\phi)E_m; \text{ where } u = (AR)\sqrt{\frac{\phi G_m}{(1-\phi)E_p}} \tag{5.2}$$

$$E_{Upper}^{TSC} = \left[\frac{1}{\phi Ep} + \frac{N_p^2(1-\phi)}{(N_p-1)*\phi^2(AR)^2 G_m}\right]^{-1} \tag{5.3}$$

$$E_{Lower}^{TSC} = \left[\frac{N_p(3N_p-4)}{3(N_p-1)^2 E_p \phi} + \frac{N_p^2(1-\phi)}{(N_p-1)*G_m\phi^2(AR)^2}\right]^{-1} \tag{5.4}$$

Recently, Lei et al. (2013) & Zhang et al. (2010) have developed the analytical solutions for the upper and lower bounds for Young's modulus using the TSC model. The upper bound is given by Eq (5.3) and lower bound is given by Eq (5.4). MD results of the present study are also compared with these lower and upper bounds predicted from TSC model, and is shown in Figs 5.1a and 5.1b. It is observed that the upper and lower bound graphs predicted using TSC model are below that of MD results. It is assumed in the TSC model that the tensile load is not carried between the platelet-to-platelet through matrix in the platelet axial gap region (see Fig 2.2 for axial gap region). This could be a valid assumption when the modulus of platelet is two to three orders of magnitude higher than the matrix or when the matrix in the axial gap region has failed. However, in the present study, the modulus ratio, which is defined as the ratio of Young's modulus of the platelet to that of matrix, is only 10 and hence the matrix carries considerable

normal stress through the axial gap region. This could be the reason why the Young's moduli predicted by TSC model show a considerable difference with the MD results.

The values of Young's modulus obtained from MD simulations agree with the theoretical predictions (Padawer and Beecher model and Voigt model); this proves the accuracy of our MD simulation methodology. Moreover, it could be observed that the non-continuum nature of simulation due to nanoscale features of the constituents does not influence the values of Young's moduli; as it agrees with theories developed based on the linear elastic assumption. This could be due to the fact that the Young's modulus is obtained from the response of the material for an infinitesimal change in the geometry. Following the comparison of Young's modulus values of homogeneous and nanocomposite models with analytical solutions, the studies regarding the influence of platelet AR on the strength, flow strength and toughness of the composite as well as the visual analysis of deformation mechanisms are conducted in the following sections.

5.3.2 Strength

In this subsection, the way in which the platelet AR affects the overall strength of the composite is discussed. Figs 5.2a and 5.2b show the MD results of the variation of measured critical stress (strength) with aspect ratio in the case of N2-SSM and N5-SSM models. For both the models, the critical stress increases with the AR up to a certain value; above this particular AR, the critical stress does not change significantly. This AR is referred to as the "critical AR corresponding to critical stress (strength)". The values are found to be $AR_{C_{CS}}^{MD,N2} \approx 35$ & $AR_{C_{CS}}^{MD,N5} \approx 90$ for N2-SSM and N5-SSM models from the Figs 5.2a and 5.2b. The subscript C_{CS} refers to the critical value corresponding to the critical stress and superscript MD indicates that the value is found from molecular dynamics simulations.

Here, the values of critical stress (strength) obtained from MD simulations are compared with the strength theories available in literature. Though a number of theoretical models are available for the prediction of Young's modulus of composites, the strength theories are very limited and are still under development. Recently, Zhang et al. (2010) worked on different patterns of the platelet arrangement in the composite using TSC model. They derived a general equation for the critical aspect ratio of

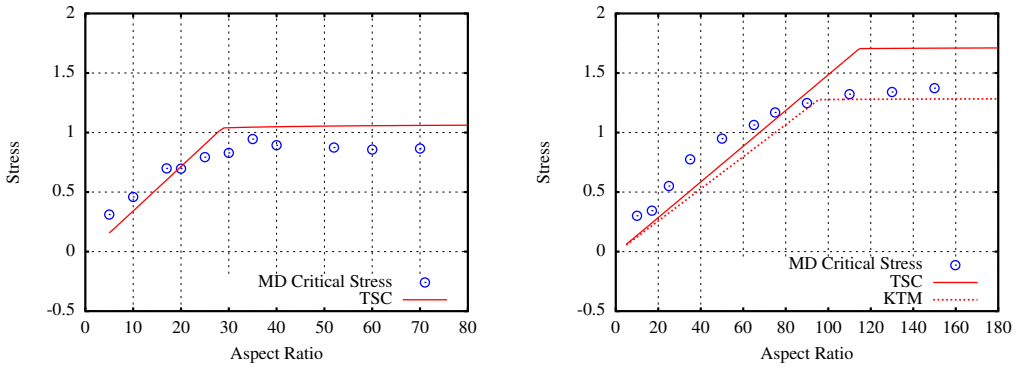

Figure 5.2 Variation of strength with aspect ratio for (a) regularly staggered (RSM or N2-SSM) and (b) stair-wise staggered (SSM or N5-SSM) models. The results obtained using MD simulations are compared with analytical theories.

platelet which separates the matrix failure from the platelet failure. They also showed that above this critical AR, the composite strength does not increase. We refer to this critical value of aspect ratio derived by Zhang et al. (2010) as AR_C^{TSC}. The expression for AR_C^{TSC} is shown in Eq (5.5), where N_p denotes the number of platelets in the unit cell of stair-wise staggered arrangement of platelets. According to the Zhang et al. (2010) model, the critical aspect ratios for N2-SSM & N5-SSM models are 30 and 115 ($AR_C^{TSC,N2} = 30$ & $AR_C^{TSC,N5} = 115$). The critical AR obtained for the N2-SSM model from the MD simulations matches with the critical AR predicted by Zhang et al. (2010). However, a significant deviation is observed for the N5-SSM model ($AR_{C_{CS}}^{MD,N2} \approx 35$ & $AR_{C_{CS}}^{MD,N5} \approx 90$).

$$AR_C^{TSC} = (N_p - 1)\frac{\sigma_{crit}^p}{\tau_{crit}^m} \tag{5.5}$$

$$\sigma_{crit}^{TSC} = \alpha^{TSC}\phi\sigma_{crit}^p \tag{5.6}$$

$$\alpha^{TSC} = \begin{cases} \left(\frac{N_p-1}{N_p}\right)\frac{AR}{AR_C^{TSC}} & \text{if } AR \leq AR_C^{TSC} \\ \left(\frac{N_p-1}{N_p}\right) & \text{if } AR > AR_C^{TSC} \end{cases} \tag{5.7}$$

Zhang et al. (2010) also obtained the expressions for composite strength in terms of the aspect ratio, critical aspect ratio and properties of constituents. This expression is given in Eq (5.6) where the platelet efficiency factor (α^{TSC}) is defined in Eq (5.7). On comparing the composite strength predicted by Zhang et al. (2010) with our MD results

(see Figs 5.2a and 5.2b), it can be observed that the prediction matches closely with the N2-SSM model and significantly deviate for N5-SSM model, here as well.

Thus, the critical AR and composite strength obtained from MD simulations for stair-wise staggered (N5-SSM) model is significantly different from the analytical predictions based on the Zhang et al. (2010). Moreover, from the visual analysis of the deformation processes which is explained in Section 5.3.5, it is found that for the N5-SSM models the platelet failure occurs for AR values of 65 and above, which is much lower than that predicted by Zhang et al. (2010) using Eq (5.5). Here, we examine the reasons for such a difference between MD and analytical results of Zhang et al. (2010). The stress distribution which is assumed by Zhang et al. (2010) is valid within the linear elastic deformation. However, the inelastic deformation occurring in the nanocomposite causes the stress distribution to be significantly different from that assumed by Zhang et al. (2010). The change in stress distribution with increasing strain in the inelastic region is explored and given in Section 5.3.6. Further, a new strength theory is developed and a new critical AR is derived analytically using the stress distribution observed from MD simulations, which is discussed in Section 5.3.7. This approach is similar to that used by Kelly and Tyson (1965). Therefore, we refer to this analysis as Kelly-Tyson Methodology or KTM. From the derivation carried out in Section 5.3.7, we obtain two critical ARs as given in Eqs (5.8) and (5.9). A smaller critical AR ($AR_{C,1}^{KTM}$) separates the platelet failure from the matrix failure. Whereas, a larger critical AR ($AR_{C,2}^{KTM}$) exists up to which the composite strength increases and remains constant thereafter. The composite strength is given by Eq (5.10) and platelet efficiency factor (α^{KTM}) is given in Eq (5.11). MD results are compared with the derived analytical solutions (KTM model) as shown in Fig 5.2b. The prediction of the KTM model is in good agreement with our MD results.

$$AR_{C,1}^{KTM} = \frac{N_p}{2}\frac{\sigma_{crit}^{p}}{\tau_{crit}^{m}} \approx 72 \qquad \text{AR above which platelet failure occurs} \tag{5.8}$$

$$AR_{C,2}^{KTM} = \frac{2N_p}{3}\frac{\sigma_{crit}^{p}}{\tau_{crit}^{m}} \approx 96 \qquad \text{AR above which strength remains constant} \tag{5.9}$$

$$\sigma_{crit}^{KTM} = \alpha^{KTM}\phi\sigma_{crit}^{p} \tag{5.10}$$

$$\alpha^{KTM} = \begin{cases} \left(\frac{N_p-2}{N_p}\right) \frac{(AR)}{(AR)_{C,2}^{KTM}} & \text{if } AR \leq AR_{C,2}^{KTM} \\ \left(\frac{N_p-2}{N_p}\right) & \text{if } AR > AR_{C,2}^{KTM} \end{cases} \tag{5.11}$$

Here, it should also be noted for the case of N2-SSM model that though the predictions of Young's moduli from TSC model do not agree very well with MD results (discussed in Section 5.3.1), the predictions of strength values from TSC model of Zhang et al. (2010) agree closely with MD results of N2-SSM model (compare Figs 5.1a and 5.2a). Here, we explain the reason for the matching of the strength values determined by Zhang et al. (2010) TSC model with N2-SSM MD results. During the ultimate tensile load of the composite, the creation of voids and cracks in the matrix region makes our nanocomposite model similar to the TSC model which has the assumption of tensile loads not transferring between the platelet-to-platelet through axial gap region. Therefore, the prediction by TSC model agrees with MD results of N2-SSM model. However, N5-SSM model shows considerable deviation. This is primarily accounted to the stress redistribution due to the inelastic deformation and asymmetric loading on platelets as discussed in Section 3.3 and in Section 5.3.7. Moreover, on comparing Fig 5.2a and Fig 5.2b, it is also seen that SSM achieves a strength higher than RSM model.

5.3.3 Flow Strength

Figs 5.3a and 5.3b show the variation of the flow stress (flow strength) with aspect ratio. The variation in flow stress is different compared to that of Young's modulus or critical stress. The value of flow stress increases linearly with aspect ratio, reaches a maximum and becomes zero above a particular value of aspect ratio. This aspect ratio is denoted as "critical AR corresponding to flow stress (flow strength)". The values are found to be $AR_{C_{FS}}^{MD,N2} \approx 35$ and $AR_{C_{FS}}^{MD,N5} \approx 60$ for N2-SSM and N5-SSM models from the Figs 5.3a and 5.3b, where subscript C_{FS} refers that the critical value corresponds to the flow stress.

For the prediction of the flow stress of composites, there seems to be no analytical theories available in open literature. Therefore, these values are not compared with any analytical predictions. However, the analysis of the trend in the flow stress val-

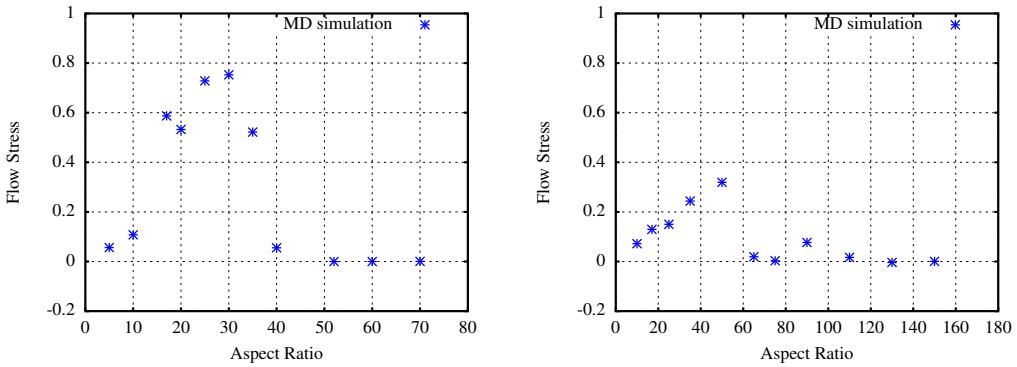

(a) (b)

Figure 5.3 Variation of flow stress with aspect ratio for (a) regularly staggered (RSM or N2-SSM) and (b) stair-wise staggered (SSM or N5-SSM) models. The results are obtained using MD simulations.

ues provides information regarding the toughening mechanisms. The existence of a non-zero flow stress value indicates that the toughening mechanisms are active. In contrast, zero flow stress value indicates absence of toughening mechanisms. The plasticity (flow stress greater than zero) could be due to the toughening mechanisms such as matrix yielding and platelet pull-out. On the other hand, the brittleness (zero flow stress) could be due to platelet breakage. Therefore, we note that the AR which separates platelet breakage from platelet pull-out is the "critical AR corresponding to flow stress" ($AR^{MD}_{C_{FS}}$). The visual analysis explained in Section 5.3.5 confirms these mechanisms.

For both RSM and SSM models, the critical ARs ($AR^{KTM}_{C,1}$) obtained using KTM model, which is shown in Eq (5.8), agree closely with the MD results of critical AR for flow strength ($AR^{MD}_{C_{FS}}$) of the composite. Hence, this critical AR, as it separates platelet failure from matrix failure and platelet pullout, plays a major role in achieving high flow strength in these bio-inspired nanocomposite materials. From the comparison of Figs 5.3a and 5.3b, we observe that the N2-SSM model achieves high flow stress with critical AR value of 35. The SSM model, though it has higher critical AR value of 60, leads to lower flow stress compared to RSM model. This shows the superior performance of RSM (regularly staggered) model with respect to flow strength.

5.3.4 Toughness

In this subsection, the influence of platelet AR on the toughness of the composite models is discussed. Figs 5.4a and 5.4b show the variation of toughness with AR for N2-SSM and N5-SSM models. Both the models show a linear increase in the toughness up to certain AR, which corresponds to $AR_{C_T}^{MD,N2} \approx 35$ & $AR_{C_T}^{MD,N5} \approx 60$ for the N2-SSM and N5-SSM models (subscript C_T refers to the critical value corresponding to the toughness). These are referred to as "the critical AR corresponding to maximum toughness". Above this AR, the toughness decreases for the N2-SSM model and does not change significantly for the N5-SSM model.

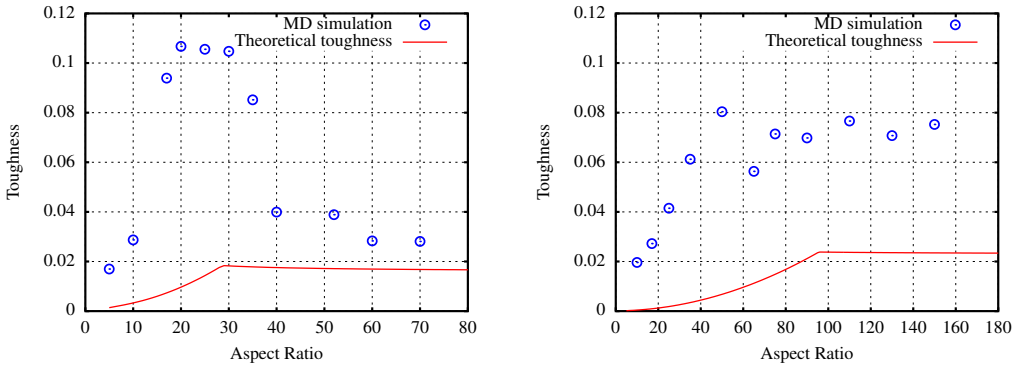

(a) (b)

Figure 5.4 Variation of toughness with aspect ratio for (a) regularly staggered (RSM or N2-SSM) and (b) stair-wise staggered (SSM or N5-SSM) models. The results are obtained using MD simulations and compared with theoretical values.

The "critical AR corresponding to maximum toughness" obtained from MD simulations also agrees closely with the critical AR obtained using Eqs (5.5) and (5.8) for N2-SSM ($AR_C^{TSC,N2} = AR_{C,1}^{KTM,N2} = 30$) and N5-SSM models ($AR_{C,1}^{KTM,N5} = 72$). Further as discussed in the previous subsection, the flow stress is higher for AR values lower than the critical AR and zero for AR values higher than the critical AR. This flow stress behavior is attributed to the occurrence of platelet pullout and platelet breakage based on the deformation mechanisms studied in Section 5.3.5. Therefore, for models with platelets ARs below the critical aspect ratio, the dominant mechanism for toughness is the platelet pullout rather than elastic deformation or strain hardening. Whereas, the toughness obtained for platelet AR above the critical value could be mostly due to the elastic deformation and strain hardening of matrix as the platelet pullout does not

occur. For N5-SSM models, high toughness values are observed for ARs higher than the critical platelet breaking AR. This could be due to the strain hardening occurring in the model due to dislocations. It should also be noted here that though both the constituents are modeled as brittle materials, plasticity and energy absorbing mechanisms are significantly occurring for AR values lower than the $AR_{C,1}^{KTM}$ (which separates platelet failure from matrix failure).

Figs 5.4a and 5.4b also show the theoretical toughness values calculated from the critical stress and Young's modulus of the nanocomposite using the relation, $w = (\sigma_{crit})^2/2E$. It should be noted here that this formula calculates the toughness due to elastic deformation only; moreover, linear elastic deformation is assumed in the calculation. The Young's modulus predicted by Padawer and Beecher (1970) model and critical stress found using TSC model for N2-SSM, and KTM model for N5-SSM, are used to calculate the theoretical toughness values. The values of toughness calculated using analytical expression discussed above do not match with the MD results. This could be due to the fact that the occurrence of various complex energy absorbing mechanisms are not included in the calculation of theoretical toughness. This shows the need for development of sophisticated theoretical models which takes into account non-linear elasticity and inelastic mechanisms such as pull-out.

Finally, we compare the values of toughness obtained for RSM and SSM models (See Figs 5.4a and 5.4b). The toughness achieved in RSM model is higher than that of the SSM model for ARs lower than critical AR. This could be due to the efficient flow behavior and the platelet pull out phenomena in the RSM model. Thus, the present analysis provides valuable suggestions about the significance of aspect ratio in achieving superior toughness.

5.3.5 Deformation Mechanisms

In order to identify the deformation mechanisms occurring in the model, the variation of stress with strain and the visual analysis of the trajectories of atoms in the model are used. Here, we look at the mechanical behavior of two representative cases of RSM model, one for an aspect ratio value of 17 and another for an aspect ratio value of 52. These values of AR correspond to the platelet AR lower and higher than the critical

AR ($AR^{MD}_{C_{FS}} \approx AR^{KTM}_{C,1}$, which separates the platelet failure from the matrix failure for RSM or SSM model). These two cases represent two different regimes of entirely different mechanical behavior as discussed in the previous section.

Fig 5.5 shows the variation of the stress with strain for these two ARs. When the AR is lower than $AR^{MD}_{C_{FS}}$, a repeated stress drop and raise is observed in the stress-strain curve (refer Fig 5.5). Let ϵ_{S_i} refers to the strains at which the drop in stress occurs, where 'i' is the number of such events; for example, ϵ_{S_1} refers to the strain at which first drop in stress occurs. In order to understand this drop in stress values

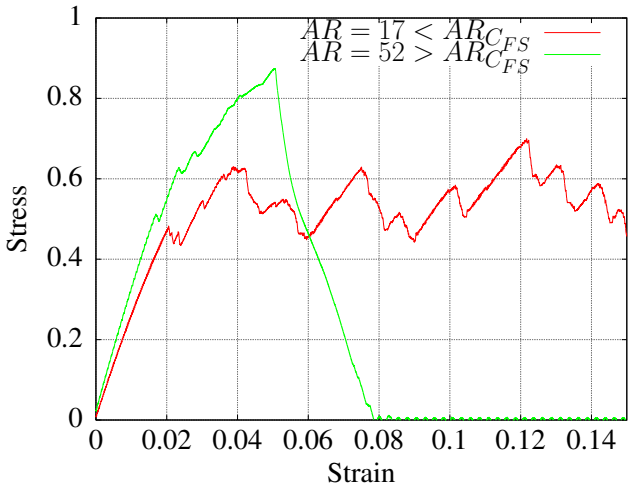

Figure 5.5 Comparison of variation of stress with strain for two typical cases: AR less than and greater than the critical AR for the RSM model.

observed in the stress-strain diagram, the deformation processes corresponding to the AR lower than $AR^{MD}_{C_{FS}}$ is analyzed for both the RSM and SSM models. Figs 5.6 and 5.7 show the deformation plots for N2-SSM with platelet AR value of 17 and N5-SSM model with platelet AR value of 35 for different strains. These AR values are lower than the critical AR ($AR^{MD}_{C_{FS}}$) for respective models. The Fig 5.6b & Fig 5.7b show the deformed structure at the strain value of ϵ_{S_1}, where no defects are seen. This absence of defects indicates that the model is undergoing crystalline deformation until the strain value of ϵ_{S_1}. Figs 5.6 and 5.7 show the deformed geometry for different strain values of the nanocomposite. It is seen that the matrix is undergoing failure through various phenomena (most of them were similar to that already discussed in Section 3.3) such as: 1) the nucleation of dislocations in the matrix near the platelet tips (see Fig 5.6d), 2) the movement of dislocations inside the matrix (see Fig 5.6g), 3) the arrest of dislocation at the interface (see Fig 5.6e and f), 4) the creation of cracks (see Fig 5.6k) and 5) the

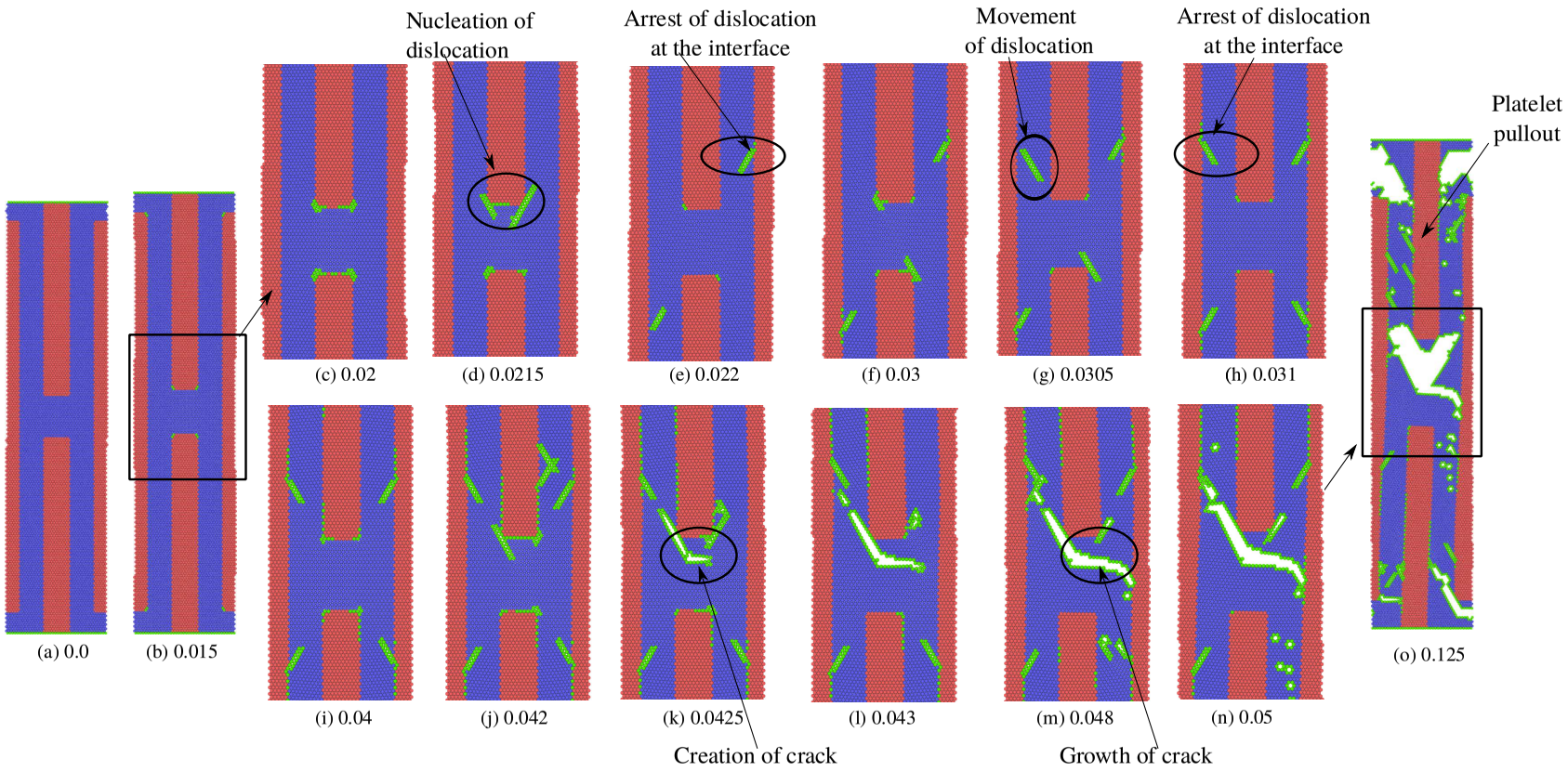

Figure 5.6 Typical deformation process at different strains for RSM model with platelet $AR = 17$. Note the occurrence of matrix failure and hence the platelet pullout. Moreover, the $AR = 17$ is lower than $AR_{C_{FS}}^{MD,N2} = 30$ and $AR_{C,1}^{KTM,N2} = 35$, which are the critical ARs at which transition from matrix failure to platelet breakage occurs.

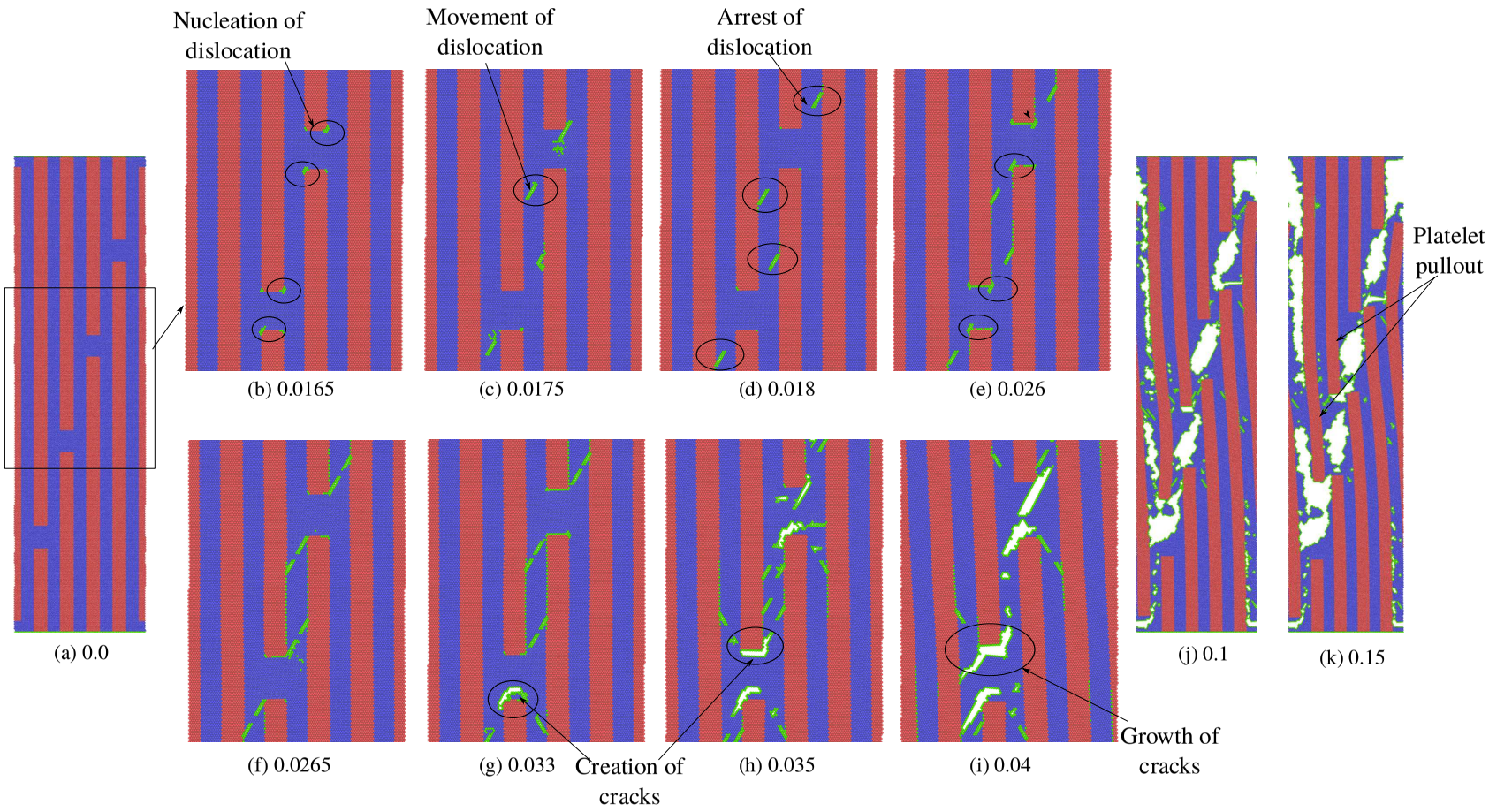

Figure 5.7 Typical deformation process for SSM model with platelet $AR = 35$. Note the occurrence of matrix failure and hence the platelet pullout. Moreover, the $AR = 35$ is lower than $AR_{C_{FS}}^{MD,N5} = 60$ and $AR_{C,1}^{KTM,N5} = 72$, which are the critical ARs at which transition from matrix failure to platelet breakage occurs.

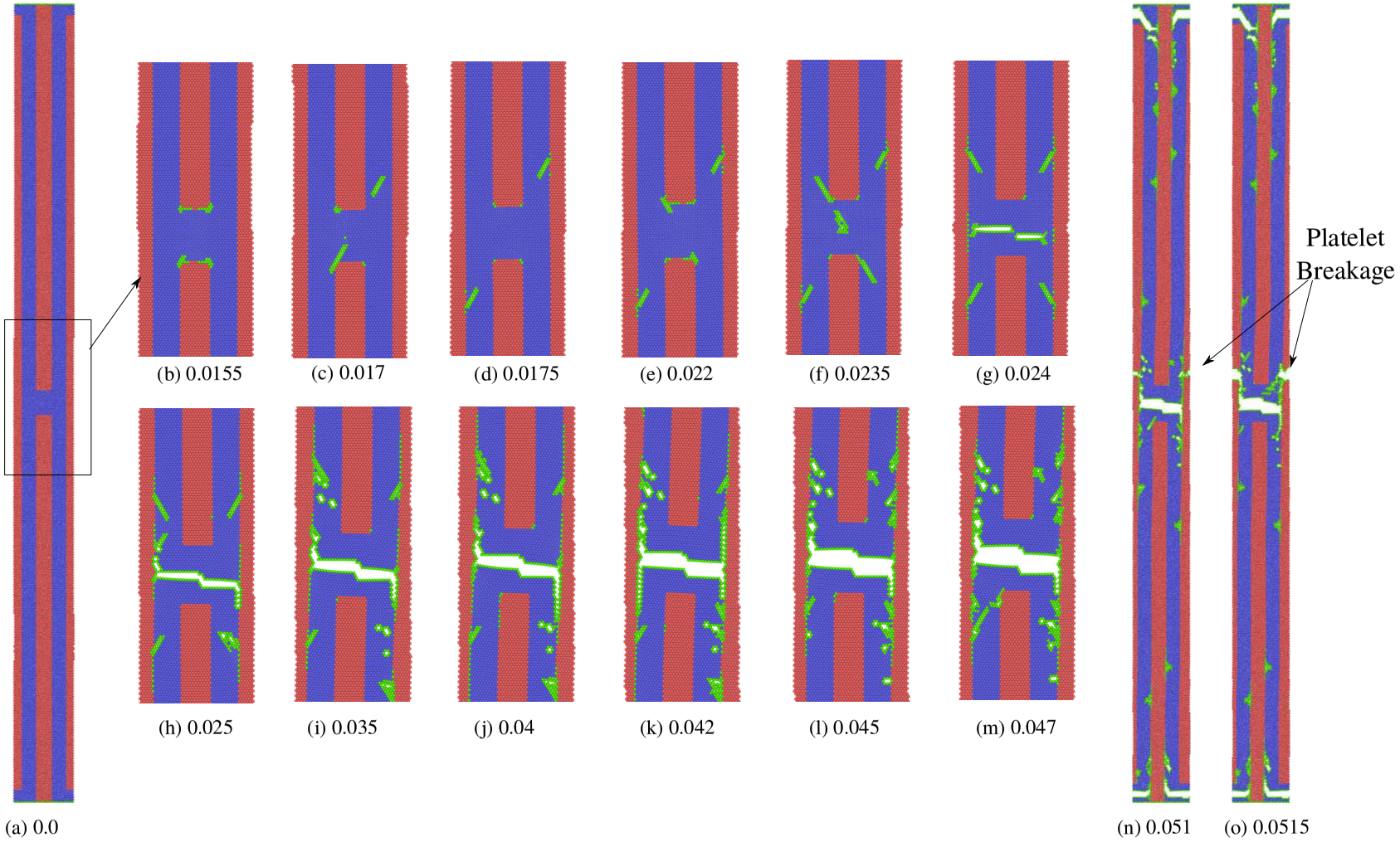

Figure 5.8 Typical deformation process at different strains for RSM model with platelet $AR = 52$. Note that the platelet breakage has occurred. Moreover, the $AR = 52$ is higher than $AR_{C_{FS}}^{MD,N2} = 30$ and $AR_{C,1}^{KTM,N2} = 35$, which are the critical ARs at which transition from matrix failure to platelet breakage occurs.

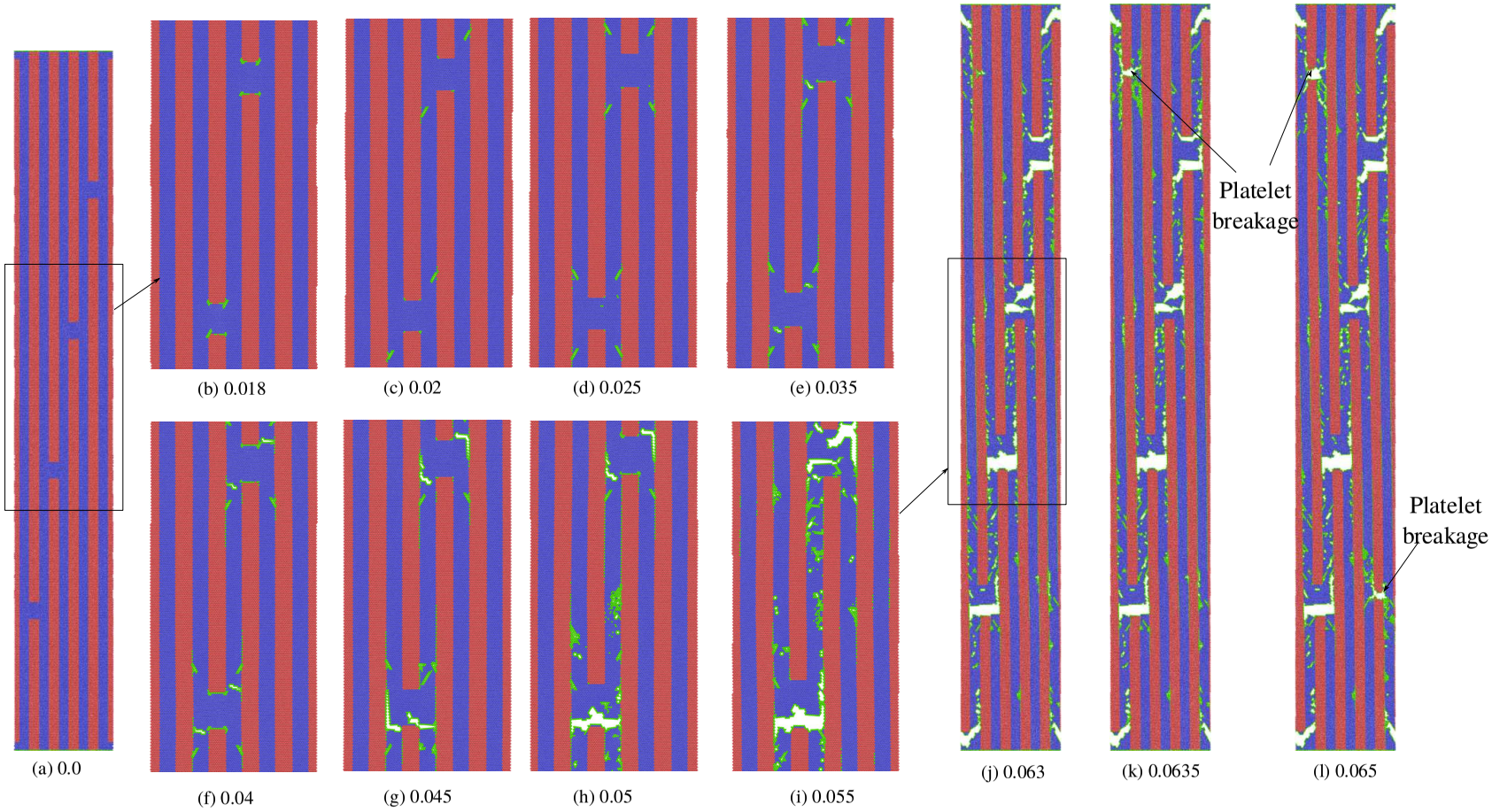

Figure 5.9 Typical deformation process at different strains for SSM model with platelet $AR = 70$. Note that the platelet breakage has occurred. Moreover, the $AR = 70$ which is higher than $AR_{C_{FS}}^{MD,N5} = 60$ and closer to $AR_{C,1}^{KTM,N5} = 72$, which are the critical ARs at which transition from matrix failure to platelet breakage occurs.

growth of cracks (see Fig 5.6m). As the matrix fails, the platelet is pulled out of the composite as shown in Fig 5.6n. This mechanism is referred to as the "platelet pull-out". The creation of voids or cracks relieves the stress in those regions. Therefore, a drop in the stress is observed in the Fig 5.5. Upon further straining, the matrix resists the motion of the platelet and causes stress to build up. Therefore, the value of stress increases again. This is repeated a few times before the complete failure of the matrix.

In contrast, at higher AR, the stress after reaching a maximum, drops suddenly to zero (refer Fig 5.5). Here, the visual analyses of deformation processes for $AR > AR_{C_{FS}}^{MD}$ are done for both the RSM and SSM models. Figs 5.8 and 5.9 show the deformation plots for N2-SSM with platelet $AR = 52$ and N5-SSM model with platelet AR=70 for different strains. The initial deformation behavior is very similar to that observed in lower values of AR as discussed the in previous paragraph. During the initial phase, the nucleation of dislocation at the platelet tips, the interaction of dislocations, and creation of voids in the platelet axial gap region are observed, which are similar for both lower and higher aspect ratios. However, instead of the platelet being pulled out of the matrix as observed in low AR, platelet breakage occurs in the case of higher aspect ratios. This platelet breakage leads to sudden and catastrophic brittle rupture of the nanocomposite.

Thus, the visual analysis described in this section helps to identify the type of failure in the nanocomposite models as well as to reason out the behavior of the stress-strain curves obtained from the MD simulations.

5.3.6 Stress Distribution in SSM

According to the strength theory developed by Zhang et al. (2010), there exists a critical value for the aspect ratio (AR_C^{TSC}, given in Eq (5.5)) of platelets which plays a crucial role in separating the platelet failure from the matrix failure. Further, the composite strength increases linearly with AR of platelets for $AR < AR_C^{TSC}$. When $AR > AR_C^{TSC}$, the composite strength remains a constant. While these predictions based on Zhang et al. (2010) agree with MD simulations for the regularly staggered model, the predictions for the stair-wise staggered model shows significant deviation as discussed in Section 5.3.2. Moreover, it is clear from the critical stress analyses (from Section 5.3.2), flow stress analyses (from Section 5.3.3) and visual analyses (from Sec-

tion 5.3.5) of the MD simulation results that the stair-wise staggered model has two critical aspect ratios: i) a critical aspect ratio of platelets ($AR_{C_{CS}}^{MD,N5} = 90$) up to which the composite strength increases linearly and remains a constant thereafter, ii) another critical aspect ratio of platelets ($AR_{C_{FS}}^{MD,N5} = 60$) exists which separates the platelet failure from the matrix failure. In this section, we explore the physical phenomena which cause the existence of these two critical AR for the stair-wise staggered models. For this purpose, the stress distribution is analyzed at deformations close to the failure of the composite. Based on the understanding gained from this section, an analytical model is developed and strength of the composite is derived in Section 5.3.7.

Figs 5.10 and 5.11 show the variation of stress distribution with increasing strain for $AR = 35 \ \& \ 70$. These two ARs represent cases of matrix failure and platelet failure respectively. In each of the Figs 5.10 and 5.11, subplots a and b show how the shear stress in the matrix and normal stress in the platelet changes with increasing strain. From both the Fig 5.10a and Fig 5.11a, it is observed that the locations of maximum shear stress in the matrix change locations with increase in applied strain; most of them move by a large distance; some of them move relatively smaller. This movement occurs primarily due to the result of various defects occurring at the matrix-platelet interface. Further, from the traditional shear-lag theory, the shear stress in the matrix causes the development of normal stress in the platelet. Therefore, the movement of the location of shear stress in these models lead to the increase in the length of the platelet over which the normal stress acts, which is shown in Fig 5.10b and Fig 5.11b. When the location of maximum shear stresses on both sides of a platelet cross each other (refer Fig 5.10a(v) and Fig 5.11a(iii)), a very high normal stress in the platelet occurs.

Fig 5.12 illustrates schematically the shifting of the location of maximum shear load and the associated increase in the length of platelet over which normal stress acts, which are observed in stair-wise staggered models. Every platelet in the stair-wise staggered model has a left large overlap (LL), left short overlap (LS), right large overlap (RL), and right short overlap (RS) regions as shown in the Fig 5.12. Consider the movement of the location of maximum shear stress on the LL and RL overlap regions. MD simulations have shown that some locations may move more rapidly than the other locations. However, for modeling purposes, we assume that the locations of maximum shear stress on both sides of the platelets move at an equal speed. Normal stress (σ_{overL})

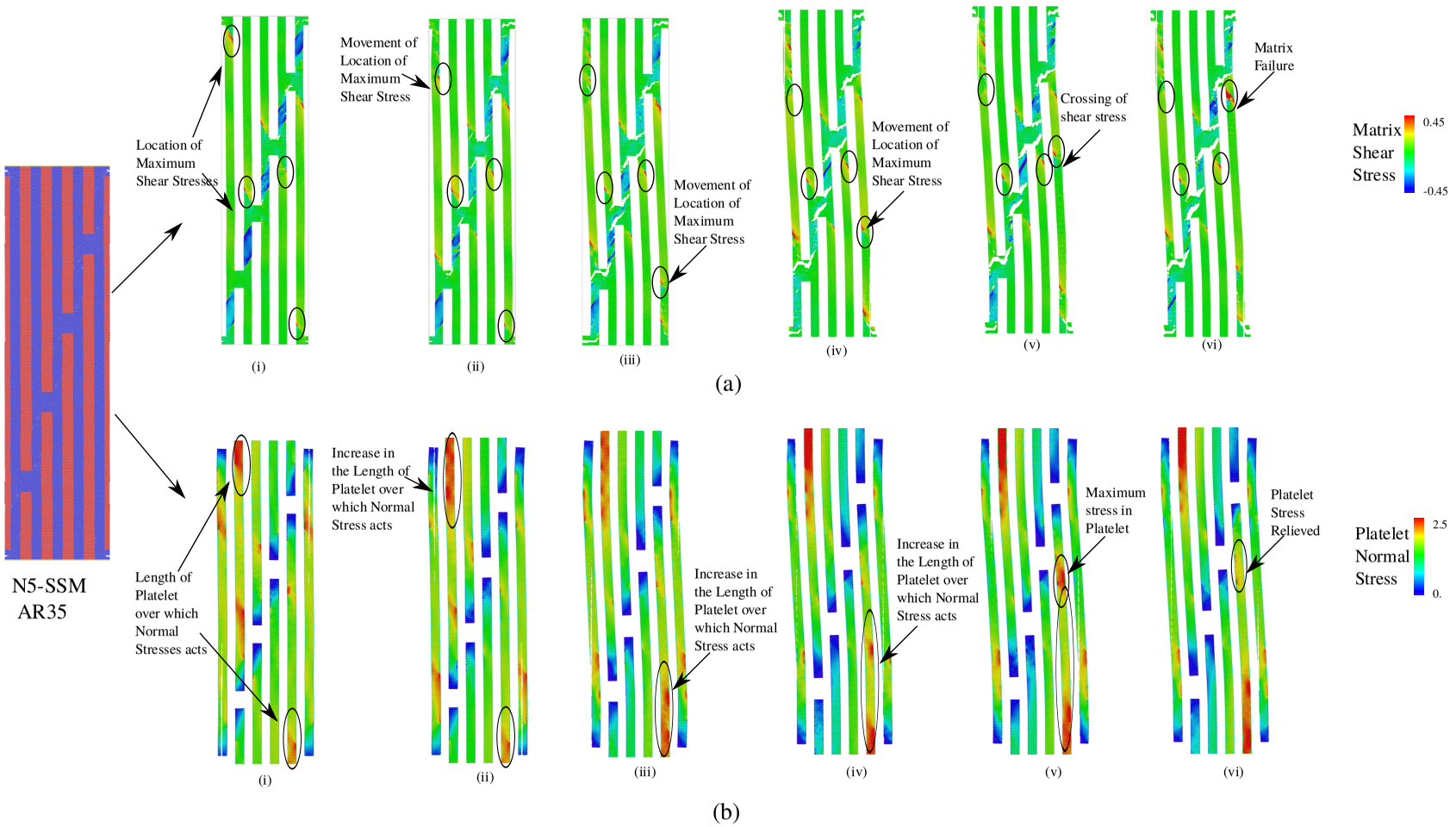

Figure 5.10 Change in stress distribution with increasing strain in SSM model with platelet $AR = 35$, which shows matrix failure and platelet pullout. (a) Shear stress developed in matrix (platelets are removed for clarity). Note here that the location of maximum shear stress changes with increasing strain. (b) Normal stress developed in platelets for different values of strain (matrix region is removed for clarity). Note here that the length of platelet over which normal stress acts increases with strain.

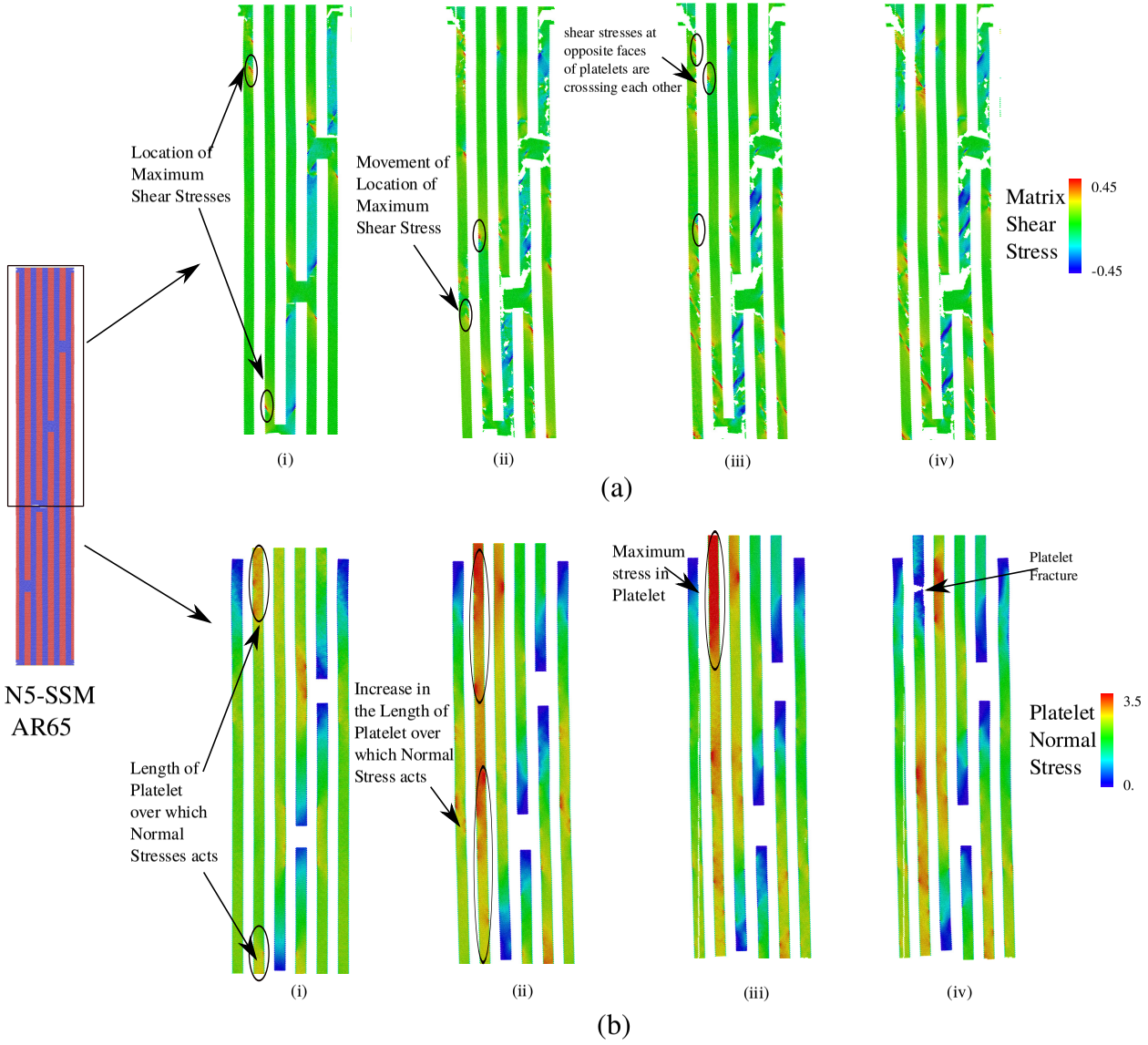

Figure 5.11 Change in stress distribution with increasing strain in SSM model with platelet $AR = 70$, which shows platelet breakage. (a) Shear stress developed in matrix (platelets are removed for clarity). Note here that the location of high shear stress moves with increasing strain (b) Normal stress developed in platelets for different values of strain (matrix region is removed for clarity). Note here that the length of platelet over which normal stress acts increases with strain.

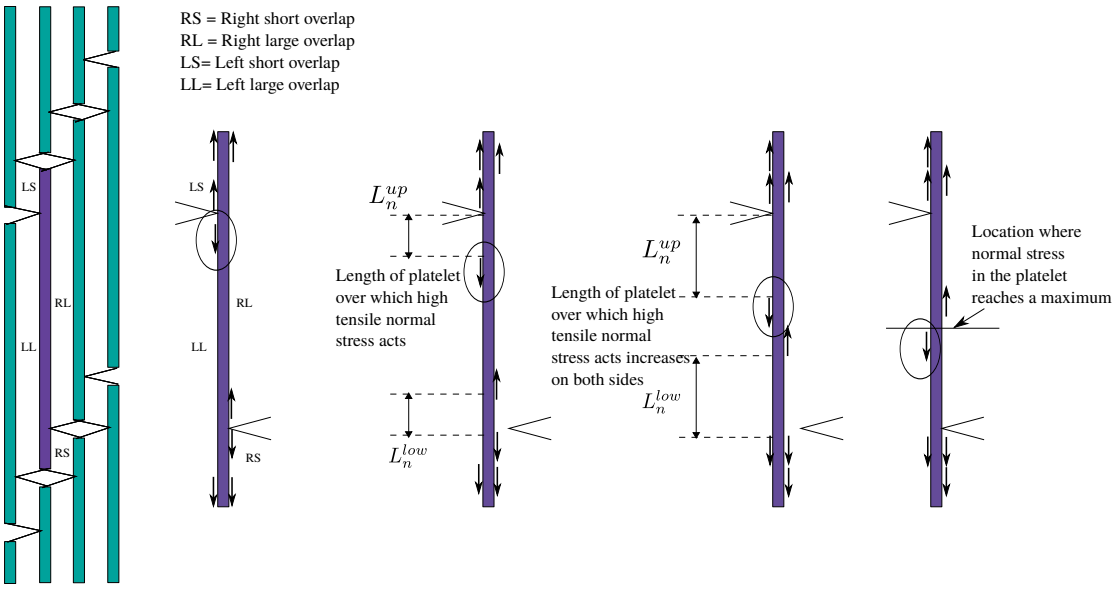

Figure 5.12 Schematic diagram illustrating the typical movement of location of shear stress as well as the associated increase in the length of platelet over which normal stress acts. Ellipses indicate the movement of location of shear stress with increasing strain.

develops in the platelets due to the shear stress in the matrix. Further, the movement of location of maximum shear stress leads to an increase in the length of platelets (L_n^{up}) over which the high tensile normal stress (σ_{overL}) acts. For a given AR of platelet, the length of the platelet over which the normal stress acts can reach a maximum value defined as L_n^{max}. By considering both LL and RL overlap regions, we get $L_n^{max} = L_n^{up}+L_n^{low} \approx \frac{(N-2)L}{N}$ at composite failure (subtracting the length of short overlap regions on both sides of platelets, which has the length of $\frac{L}{N}$, for more details see next section). Further, when the movement of shear loads on both sides of the platelet cross each other, the platelet experiences maximum normal stress (σ_{max}) as shown in the Fig 5.12. The value of σ_{overL} is less than the value of σ_{max}. When the maximum normal stress (σ_{max}) is lower than the platelet strength, inelastic deformation of matrix and platelet pull-out occur. When σ_{max} is higher than the platelet strength, the platelet fractures. At a critical AR ($AR_{C_{FS}}^{MD,N5}$) of platelets, the maximum normal stress in the platelet reaches the platelet strength. Therefore, this $AR_{C_{FS}}^{MD,N5}$ separates the platelet failure from the matrix failure.

Though the platelet breakage occurs for $AR > AR_{C_{FS}}^{MD,N5} = 60$, the increase of composite strength is observed for up to the $AR < AR_{C_{CS}}^{MD,N5} = 90$. The reason for this phenomenon is explained here. From the traditional strength theory of short

fiber-reinforced composites (Kelly and Tyson, 1965), the tensile strength of a composite depends on the average stress in the platelet (averaged over the length) at composite failure. The average stress in a platelet is defined as the sum of the normal stress acting over the length of the platelet divided by the length of the platelet. At composite failure, the length of the platelet (L_n^{max}) over which the normal stress (σ_{overL}) acts reaches a maximum. This value of L_n^{max} increases with the length or AR of the platelet (as the thickness of the platelet is not varied, increasing length is equivalent to increase in the AR). Therefore, the average stress of the platelet at composite failure also increases with AR. This leads to increase in the strength of the composite with AR. This increase in composite strength occurs till the value of σ_{overL} reaches the platelet strength. Therefore, another critical AR ($AR_{C_{CS}}^{MD,N5}$) of platelets exists up to which the composite strength increases. In the Section 5.3.7, the observed physical phenomena is modeled analytically and expression for critical AR and strength of composite is derived.

5.3.7 New Strength Theory for SSM

In this section, we derive the analytical expressions for the critical AR and the strength of composite of the general stair-wise staggered model based on the physical phenomena observed from MD simulations as explained in Section 5.3.6. Fig 5.13a shows the typical arrangement of platelets in a stair-wise staggered model with N platelets. A single platelet undergoing tensile loading by shear of nearby matrix is shown in Fig 5.13b. Further, Fig 5.13c shows the uniform shear load distribution assumed by Zhang et al. (2010). However, the actual shear load distribution observed in the MD simulations is more close to what is shown in Fig 5.13d which is consistent with the traditional shear transfer theories (Barthelat et al., 2013) (according to which the shear load is concentrated on both the ends of the overlap region).

From the force equilibrium equations, we obtain the relation between the shear load acting in upper and lower overlap region as given in Eq (5.12).

$$F^L = F^U \tag{5.12}$$

In terms of average shear stress (τ^U) acting in the platelet, the shear load (F^U) can

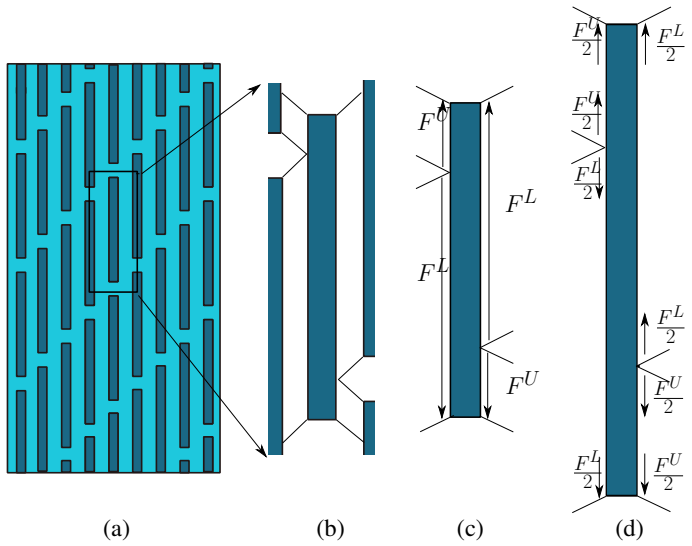

Figure 5.13 Load transfer details for stair-wise staggered model: (a) typical stair-wise staggered model, (b) typical tensile load transfer from platelets to platelets via shear in the matrix, (c) shear loads assumed to act on a platelet by Zhang et al. (2010), and (d) shear load acting on a platelet observed in MD simulations, which is also consistent with theory developed by Barthelat et al. (2013).

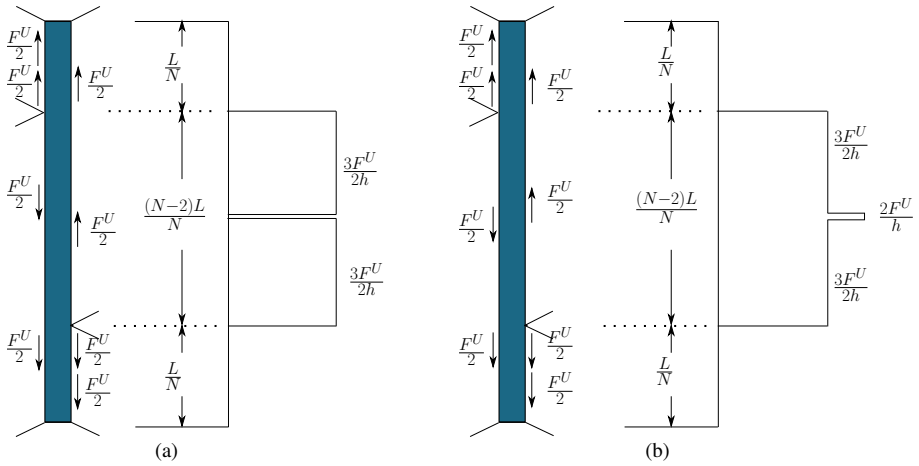

Figure 5.14 Variation of normal stress distribution on a platelet in SSM model which occurs due to the movement of location of maximum shear stress: (a) before the platelet failure and (b) at the platelet failure.

be expressed by Eq (5.13), where L is length of the platelet and N is the number of platelets in the unit cell of stair-wise staggered model.

$$F^U = \frac{\tau^U L}{N} \tag{5.13}$$

Fig 5.14 shows the movement of the location of shear load due to the matrix failure at the interface. The movement of shear load causes the increase in the length of the platelet over which normal stress acts (see Fig 5.14a). Whereas, the crossing of the shear loads acting on the both sides of the platelet causes a very high normal stress in the platelet, which is shown in Fig 5.14b.

Further, (1) the normal stress at any section of platelet over the length of $\frac{(N-2)L}{N}$, (2) maximum normal stress in the platelet and (3) average normal stress in the platelet at composite failure can be calculated by Eq (5.14), Eq (5.15) and Eq (5.16) respectively.

$$\sigma^p_{overL} = \frac{3F^U}{2h} \qquad \text{stress at any section of platelet length of } \frac{(N-2)L}{N} \text{ see Fig 5.14} \tag{5.14}$$

$$\sigma^p_{max} = \frac{2F^U}{h} \qquad \text{maximum stress on the platelet} \tag{5.15}$$

$$\bar{\sigma^p} = \int_{\frac{L}{N}}^{\frac{(N-1)L}{N}} \frac{3F^U}{2Lh} dy \qquad \text{average stress in platelet at composite failure} \tag{5.16}$$

Moreover, using Eq (5.13), the different types of stress acting on the platelet are expressed in terms of matrix shear stress by the following equations.

$$\sigma^p_{overL} = \frac{3}{2}\tau^U \frac{(AR)}{N} \tag{5.17}$$

$$\sigma^p_{max} = 2\tau^U \frac{(AR)}{N} \tag{5.18}$$

$$\bar{\sigma_p} = \frac{3}{2}\tau^U \frac{(AR)}{N}\left(\frac{N-2}{N}\right) \tag{5.19}$$

It is assumed that when the platelet failure occurs, the matrix shear stress is already in its critical value, i.e., its shear strength (τ^m_{crit}). Therefore, the critical AR which separates the platelet breakage from matrix failure is obtained by comparing the maximum normal stress acting on the platelet (given by Eq (5.18)) with the platelet strength (σ^p_{crit}) and is given in Eq (5.20). Moreover, the increase of average normal stress in the platelet can occur until the normal stress, which is acting over the length of $\frac{(N-2)L}{N}$, reaches the platelet strength. Therefore, by comparing the Eq (5.17) with that of platelet strength, the critical AR up to which the increase in composite strength occurs can be calculated and the expression is given in Eq (5.21).

$$(AR)^{KTM}_{C,1} = \frac{N}{2}\frac{\sigma^p_{crit}}{\tau^m_{crit}} \approx 72 \quad \text{in terms of maximum stress acting on platelet} \tag{5.20}$$

$$(AR)^{KTM}_{C,2} = \frac{2N}{3}\frac{\sigma^p_{crit}}{\tau^m_{crit}} \approx 96 \quad \text{in terms of stress acting over platelet length} \tag{5.21}$$

The platelet failure occurs for $AR > 72$. However, the average normal stress in the platelet at composite failure increases for $AR < 96$. This leads to the increase in the composite strength for $AR > 72$. This predicted critical ARs agree with our MD results more accurately.

Further, the strength of the composite can be written as follows by ignoring contribution from the matrix,

$$\sigma^{KTM}_{crit} = \phi\bar{\sigma}_p \tag{5.22}$$

Using Eqs (5.19) and (5.21) in Eq (5.22), we can express the strength of the composite as follows,

$$\sigma^{KTM}_{crit} = \begin{cases} \left(\frac{N-2}{N}\right)\frac{(AR)}{(AR)^{KTM}_{C,2}}\phi\sigma^p_{crit} & \text{if } AR \leq AR^{KTM}_{C,2} \\ \left(\frac{N-2}{N}\right)\phi\sigma^p_{crit} & \text{if } AR > AR^{KTM}_{C,2} \end{cases} \tag{5.23}$$

This equation provides the relationship between the strength of the composite and the aspect ratios of the platelets. This relation is used in the Section 5.3.2 in order to compare with the MD results. These analytical equations show good agreement with the critical stress values predicted by MD results.

5.4 Conclusion

In this chapter, the effect of aspect ratio of platelets on the mechanical behavior of bio-inspired nanocomposite structures is investigated. The influence of the platelet aspect ratio is analyzed for both the regularly staggered and stair-wise staggered models. MD simulations are performed to investigate the nanoscale structural mechanics problems. These MD simulations are useful in discovering new physics or mechanisms as no a priori assumptions are made about the process to be investigated. Moreover, as the intent of the thesis is to develop ceramic-ceramic nanocomposites, both the platelet and matrix are modeled as brittle materials. Therefore, the understanding gained from this study is applicable to all brittle-matrix nanocomposites.

The Young's moduli for the nanocomposites which are predicted from MD simulations for various aspect ratios of platelets agree closely with the available theories of platelet-reinforced composites. This agreement between theory and simulations gives confidence in the MD simulation methodology used in the thesis. Further, based on the stress distribution observed in MD simulations, a new strength theory is developed. The strength of the nanocomposites predicted using the new strength theory matches with MD results. Further, this new theoretical model also accurately predicts the critical AR at which platelet fracture for the stair-wise staggered model occurs.

The important findings from this study are listed below,

- Regularly staggered model even with a low AR can achieve a combination of higher Young's modulus, flow strength and toughness.
- Stair-wise staggered model could achieve a combination of high Young's modulus, and higher tensile strength than the regularly staggered model for larger AR.
- For the regularly staggered model, a single critical aspect ratio exists. This critical AR separates platelet fracture from the matrix failure. The strength of composite reaches a maximum value at this critical AR. However, for the stair-wise staggered model, there exists two critical aspect ratios for each of the cases mentioned above.

- The pull-out of platelet from the matrix is found to be the fundamental mechanism at the nanoscale which causes high flow strength and toughness, even though the constituents are modeled as brittle.

- For stair-wise staggered model, the "critical AR corresponding to maximum toughness" obtained from MD simulation is different from the earlier analytical studies. However, it matches with the critical AR ($AR_{C,1}^{KTM}$) obtained in the new strength theory developed.

- Further, in ceramic-matrix nanocomposites, the matrix failure leads to more ductile kind of failure and platelet failure leads to catastrophic brittle rupture of the composite.

CHAPTER 6

Effect of Interface Strength

In order to examine the transferability of mechanical principles of biological materials to design high-toughness ceramic matrix nanocomposites (CMNC) and to provide design guidelines for CMNCs, effect of platelet aspect ratio on the overall mechanical behavior of regularly staggered model (RSM) and stair-wise staggered model (SSM) were analyzed in the previous chapters. In this chapter, the effect of interface strength is analyzed. The interface plays a key role as an enormous amount of interfacial area exists in the nanocomposite materials. The interface strength or binding energy between the platelet and matrix atoms is varied, and the changes in the mechanical properties and deformation mechanisms are studied using molecular dynamics (MD) simulations. Both the RSM and SSM models show interface decohesion and platelet sliding without any dislocation activities in the matrix for very low interface strengths. At intermediate interface strengths, when the interface strength is lower than matrix strength but closer to that of matrix, both the models show excellent flow stress and toughness due to the combination of the dislocation activities in the matrix and the pullout of platelets. For higher interface strengths where the interface strength is greater than the matrix strength, the RSM continues to show bulk plasticity and pullout, but the SSM undergoes platelet fracture. The understanding gained could be useful in the interface design of bio-inspired nanocomposites.

6.1 Introduction

It is well known that the interface plays a key role in the toughness and failure behavior of the micro-scale ceramic matrix composites (CMC)(Rühle and Evans, 1989; Evans, 1990; Faber, 1997; Kim and Mai, 1998). In these micro-scale CMC's, the interface is designed so that the microcracks generated at the matrix is deflected at the interface. This mechanism aids in avoiding the early failure of fibers by a notch effect and also increases the toughness of composites by allowing graceful failure. For enabling this mechanism of crack deflection at the interface, a weak interface is required. In contrast,

the efficient load transfer between the reinforcement and the matrix necessitates a strong interface. Therefore, it is required that the interface region be strong enough for stress transfer, yet weak enough for considerable crack deflection and interface debonding (Clegg et al., 1990; Suzuki et al., 1994).

Important mechanisms associated with toughening in the brittle matrix composites (such as microscale-CMCs) are the following: 1) crack deflection at the interface, 2) crack- bridging by the reinforcements and 3) fiber pullout on the crack plane (Xia and Li, 2014). Nanoscale-CMCs (nCMC or CMNC) which have much larger interface regions and much stronger nano-sized inclusions could possess enhanced strength and toughness over the microscale counterparts. Such enhancements are possible only if the toughening mechanisms of micro-scale composites are also observed at the nano-scale CMCs (Xia and Li, 2014).

To determine whether the crack propagates along the interface or penetrate the reinforcement, various studies are reported in the literature, such as energy release rate (Nishioka et al., 2003; Hutchinson and Suo, 1992), maximum hoop stress (Yuuki and Xu, 1992), and zero complex stress intensity factor (Akisanya and Fleck, 1992) approaches. However, these approaches are based on continuum mechanics, which makes these methods questionable at nanoscale. Therefore, studies such as MD simulations which takes into account individual atomistic nature of materials are necessary to explore the interface behaviors. Initially, MD simulations were used to study interface behavior for various applications in the fields of biological and chemical engineering (Galema et al., 1994; Sprous et al., 1999). With the expansion of MD methods, the interface behavior using atomistic simulations is studied for engineering and structural mechanics problems as well (Büyüköztürk et al., 2011). Therefore, MD simulations are used for understanding the effect of interface strength on the model brittle matrix nanocomposites.

Moreover, most of the analytical works in composites have assumed a perfect bonding between matrix and inclusions, so that displacements and forces are continuous along the interface (Hull and Clyne, 1996). However, in practice, it is not always necessary. Therefore, variety of interfacial behaviors such as strong interface and weak interface also needs to be considered for a complete understanding of the mechanical behavior of composites. Therefore, in this chapter, the influence of interface strength

on the mechanical response of bio-inspired brittle matrix nanocomposite is studied; the results obtained from this study could aid in the design of advanced ceramic nanocomposites with remarkable combination of mechanical properties. Such different interfaces are implemented when different interface properties are used in the model. Details of the computational methods used in this chapter were explained in Chapter 2. The effect of depth of interfacial interaction and interface strength between the platelet and matrix atoms on the behavior of interface are initially analyzed in Section 6.3.1 in detail. Thereafter, the effect of interface strength on the overall mechanical behavior of nanocomposites is analyzed in Section 6.3.2. Further, the main conclusions are presented in Section 6.4.

6.2 Simulation Methodology

The RSM and SSM models are built using two dimensional hexagonal crystals which is shown in Fig 3.1. Both the RSM and SSM models are built with same number of atoms in platelet axial gap (10), platelet transverse gap (10), platelet thickness (10) and platelet overlap length (50). This leads an AR of 17 in RSM model and 45 for SSM model. Further details about the atomistic geometry can be seen in Section 2.2.3. Moreover, Lennard-Jones (LJ) interatomic potential, which is modified by adding a cut-off function as discussed in Section 2.2.1, is defined between the atoms. Different LJ parameters are used for different constituents: soft matrix has $\sigma^m_{LJ} = 1$ and $\epsilon^m_{LJ} = 0.1$, hard platelets has $\sigma^p_{LJ} = 1$ and $\epsilon^p_{LJ} = 1$. Moreover, the LJ parameters for the interaction between the platelet and matrix atoms are defined as follows: $\sigma^i_{LJ} = 1$ is used to mimic coherent interface and $\epsilon^i_{LJ} = 0.01 - 1$, i.e., ϵ^i_{LJ} is varied from 0.1 times that of matrix strength to 10 times that of matrix strength, in order to study the effect of interface strength on the overall mechanical properties of nanocomposites. Further, the mechanical properties of the constituents can be found in Table 2.1.

Isothermal uniaxial tensile test at a strain-rate of 10^{-5} is performed for different interface strengths. Further, modeling details can be seen in Section 2.2. Moreover, the methods for calculation of typical mechanical properties are shown in Fig 2.5 and discussed in Section 2.3.1. The Young's modulus is the slope of the stress-strain diagram at the origin. Critical stress is taken as the maximum stress observed during the tensile

test. Flow stress is taken as the average value of stress in the strain range of 8% to 10%. Toughness is measured as the area under the stress-strain diagram.

6.3 Results and Discussion

Initially, the behavior of interface for different interaction parameters is studied: (1) different depths up to which interfacial interaction force acts and (2) different interfacial strengths between the matrix and platelet atoms. Different simulation setups used for these two studies and their results are analyzed. Thereafter, the effect of interface strength on the overall mechanical behavior of nanocomposite is studied by performing computational uniaxial tensile tests as mentioned in the previous section. The variation of mechanical properties and deformation mechanisms for different interface strengths are analyzed on both the RSM and RSM models.

6.3.1 Behavior of Interface

Before studying the effect of interface strength on the mechanical behavior of the nanocomposite, the behavior of interface alone has to be understood at first. This is done in the following section. Thereafter, the behavior of nanocomposite is studied.

6.3.1.1 Influence of the Depth of Interfacial Interaction

The interface behavior of the 2D LJ nanocomposite model under consideration can be controlled by the two LJ parameters and the cut-off radius in the LJ interatomic potential function defined between the matrix atoms and platelet atoms; they are σ^i_{LJ}, ϵ^i_{LJ} and $R_{cut-off}$ respectively. The σ^i_{LJ} parameter of the interface is maintained same as that of matrix and platelet in order to maintain coherent interface. The ϵ^i_{LJ} parameter of the interface controls the bond strength of the interface and its effect on the interface behavior is probed in the next section. Moreover, the behavior of interface in the most composites is dependent on the depth of influence of the atoms at the interface with the atoms at the bulk. Therefore, the effect of cut-off radius of interface atoms is initially analyzed in this section.

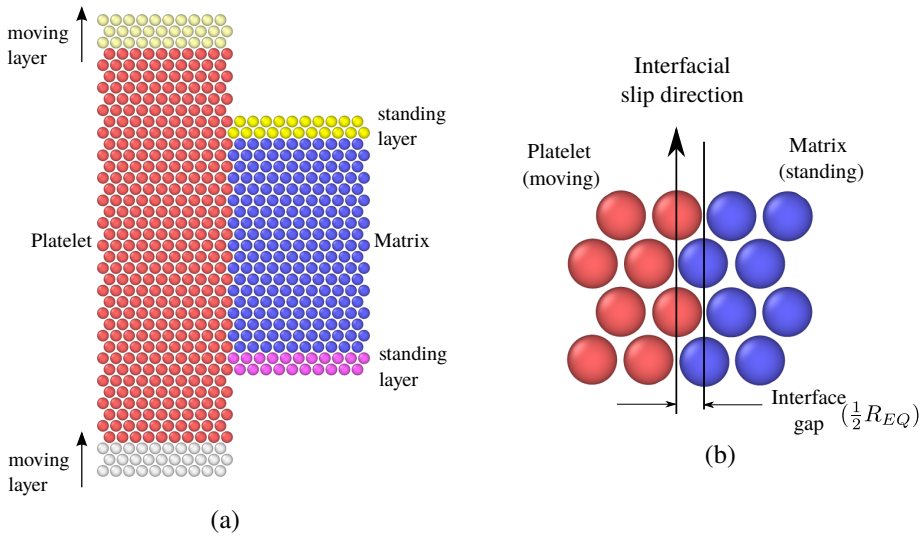

Figure 6.1 (a) Simulation set-up to measure interfacial frictional forces during shear load. (b) Detailed view of the interface region. Note: interface gap is very small, and R_{EQ} is the equilibrium interatomic distance.

To analyze the influence of depth of interface interaction, a separate simulation set-up is developed as shown in the Fig 6.1a which mimics the motion of interface during the uniaxial tensile loading in the nanocomposite model. Platelet is moved by giving a constant velocity of very small value to both the top and bottom moving layers of platelet atoms. Matrix is kept stationary by giving zero velocity for both the top and bottom standing layers of matrix atoms as shown in the Fig 6.1a. Moreover, the zoomed in interface region is also shown in the Fig 6.1b. MD simulations are performed using the simulations set-up shown in Fig 6.1a. The friction force is measured when the platelet atoms slide past the matrix atoms. The variation of friction force, with the movement of platelet atoms which is expressed in terms of the number of lattice unit cells is shown in the Fig 6.2. The value of $R_{cut-off}$ is varied from 1.71 to 2.5 and the variation of friction force for each case is calculated using MD simulation. The $R_{cut-off} = 1.71$ is used in all the simulations carried out in thesis and that value is chosen from Holian et al. (1991) which is minimum cut off distance needed to be chosen to reduce computational power as well as to reproduce the results obtained by others. So the effect of $R_{cut-off}$ is studied for $R_{cut-off} > 1.71$ only. The frictional forces calculated for each case is shown in the Fig 6.2. It can be observed from the figure that the variation of depth up to which interface force acts does not influence the interface behavior in the model system under consideration. Therefore, $R_{cut-off} = 1.71$ is used in all the simulations which is computationally more efficient.

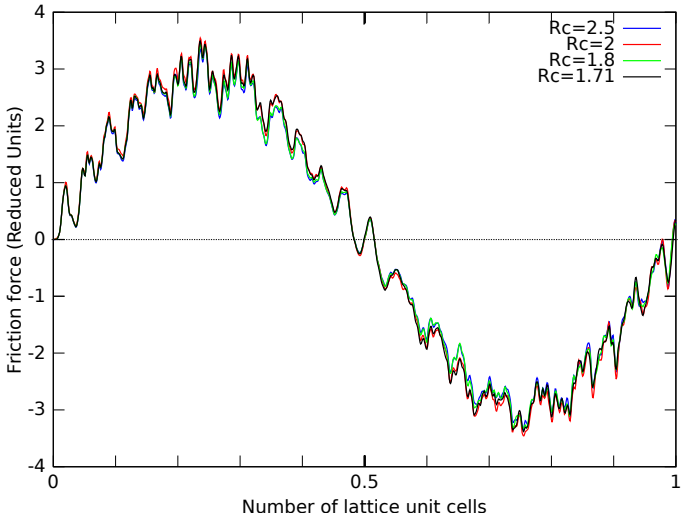

Figure 6.2 Variation of frictional force is shown for different depths up to which the interfacial interaction force acts.

6.3.1.2 Influence of Interface Strength

In this section, how the interface strength influence the platelet-matrix interface slipping behavior is studied. In the model nanocomposite considered, slipping is possible in two directions, one along the interface, and the other at an angle (30°) to the platelet axis. Both the interfacial (between platelet and matrix) and interatomic (between matrix and matrix) slipping directions are shown in Fig 6.1b and Fig 6.3a respectively. It is also to be noted here that the interatomic slipping is the same as that of slipping along horizontal direction as shown in Fig 6.3b; this can be understood by the fact that the rotation of Fig 6.3a by 60° clock-wise (the angle between the interatomic slip direction and the horizontal direction), Fig 6.3b can be obtained.

Interfacial shear strength (IFSS) is the shear stress required for the platelet to slide past the matrix along the interface (Pavia and Curtin, 2011; Frankland et al., 2002). MD simulations are performed to obtain IFSS for different interfacial bond strengths (ϵ^i_{LJ}). The simulation setup used to measure IFSS is shown in the Fig 6.1a, where the platelet atoms are moved and the matrix atoms are kept stationary similar to that used in previous Section 6.3.1.1. The variation of IFSS with ϵ^i_{LJ} is shown in Fig 6.4. IFSS values are not shown for higher ϵ^i_{LJ} values. This is explained in the following. At larger values of ϵ^i_{LJ}, the high value of IFSS causes the platelet atoms to be strongly bonded to the matrix atoms. Moreover, other mechanisms such as slipping of atoms along interatomic directions occur rather than the slipping of platelet atoms along the interface. There-

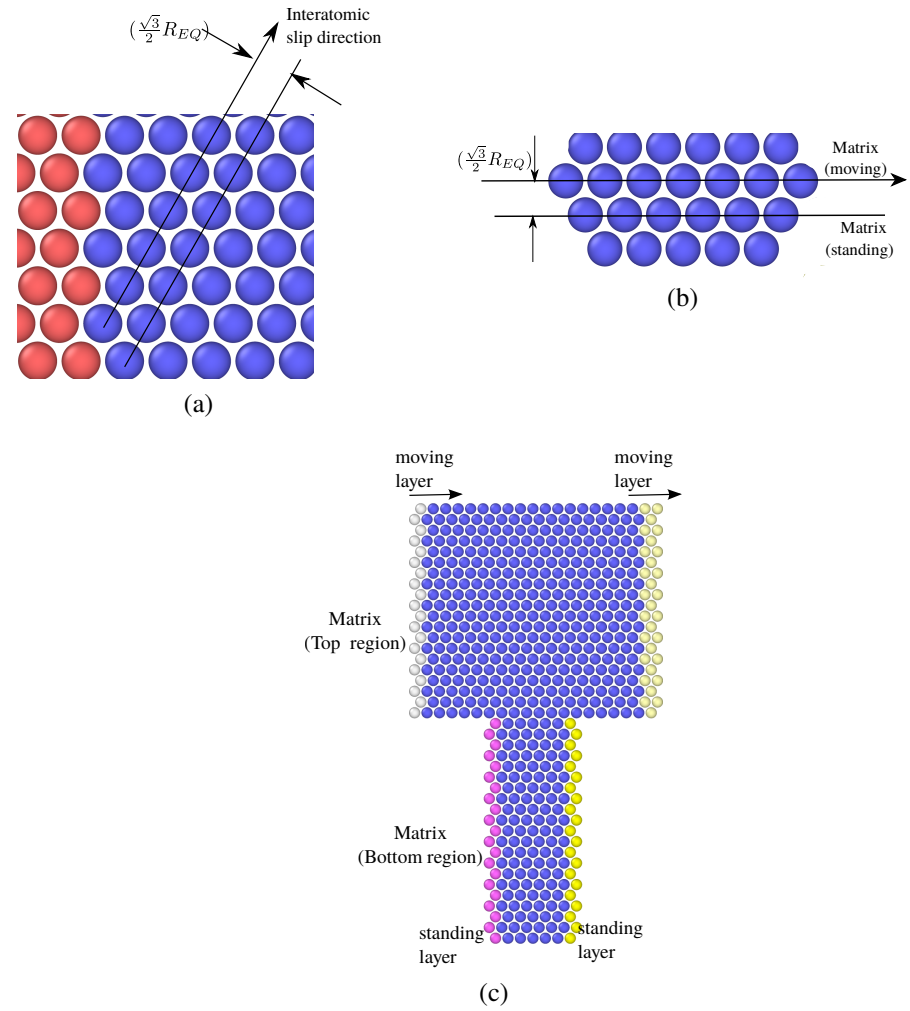

Figure 6.3 (a) Detailed view of the interface region along with interatomic slipping direction. Note: gap between the interatomic slip directions is larger compared to the interface gap in interfacial slip direction which is shown in Fig 6.1b and R_{EQ} is the equilibrium interatomic distance. (b) Slipping direction rotated 60 degree clock-wise. (c) Simulation setup to measure interatomic shear strength (IASS) along interatomic slipping direction.

fore, the IFSS values for higher ϵ^i_{LJ} are obtained by linear extrapolation of the IFSS values obtained for lower ϵ^i_{LJ}.

Here, interatomic shear strength (IASS) is defined as the maximum shear stress required to move the matrix atoms past another row of matrix atoms as shown in Figs 6.3a and 6.3b. MD simulation is performed by moving matrix atoms in top region and keeping the matrix atoms in the bottom region stationary as shown in Fig 6.3c. The moving layers in the top region are moved by giving a constant velocity of very small value. Whereas, the standing layers in bottom region are kept stationary by giving zero velocity (Different layers are shown in the Fig 6.3c). Using MD simulations, the value of

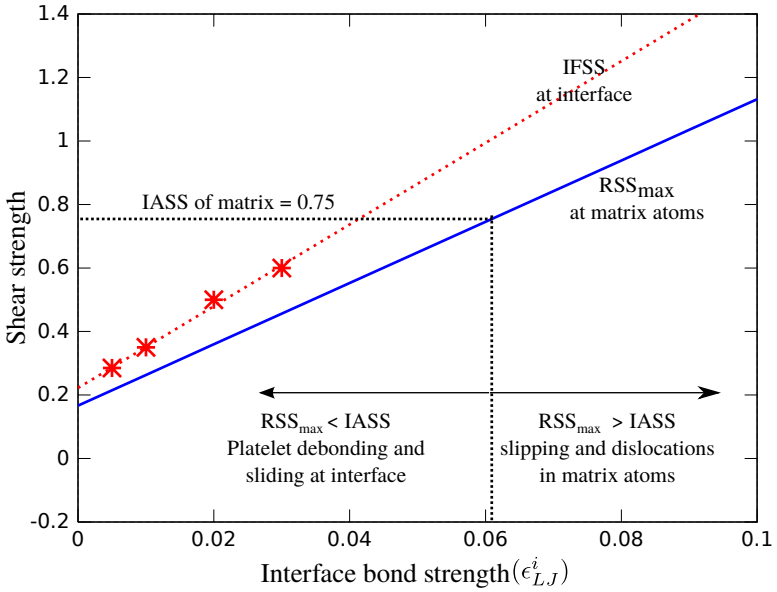

Figure 6.4 Variation of shear strength for different interface strengths is shown. Red dotted line shows the variation of interfacial shear strength. Blue solid line shows the maximum resolved shear stress due to the load applied along the interface.

IASS is obtained as 0.75 for the matrix atoms ($\sigma^m_{LJ} = 1$ & $\epsilon^m_{LJ} = 0.1$) in the present study.

Moreover, the resolved shear stress (RSS) is defined as the shear stress acting on the interatomic slipping direction due to the shear stress applied along the interfacial slipping direction (It is already discussed that the angle between these two directions is 30°). The maximum resolved shear stress (RSS_{max}) acting on the interatomic slipping direction can be expressed as $RSS_{max} = IFSS \times \cos^2(\theta)$, where $\theta = 30°$ (the angle between the interatomic slip direction and the vertical direction). The variation of RSS_{max} with interfacial bond strength (ϵ^i_{LJ}) is shown in the Fig 6.4.

The three parameters, IFSS, IASS, and RSS_{max}, which are defined and discussed in the above three paragraphs, play a significant role in the behavior of interface. From the above discussion it is clear that whenever the $RSS_{max} > IASS$ ($IASS = 0.75$ in the present study, obtained using MD simulations), the slipping of atoms in the interatomic slipping direction should result rather than the debonding or sliding of atoms along the interface; the later mechanism occurs if $RSS_{max} < IASS$. This condition, $RSS_{max} < IASS$, is satisfied when the $\epsilon^i_{LJ} < 0.062$, which can be found using the Fig 6.4; the point at which the RSS_{max} value is equivalent to the IASS value. This value of ϵ^i_{LJ} is

referred to as the critical interface bond strength ($\epsilon_{LJ}^{i,C} = 0.062$).

The value of critical interface bond strength (or sometimes referred as critical interface strength) plays a major role in the deformation behavior of the nanocomposites, which is discussed in the following section.

6.3.2 Behavior of nanocomposites

The effect of interface strength on the mechanical behavior of nanocomposite is studied in this section (It is to be noted here that in this chapter, the value of ϵ_{LJ} which is defined between the matrix and platelets atoms, i.e., ϵ_{LJ}^{i} is also referred to as the interface strength or the interface bond strength). For this purpose, the values for ϵ_{LJ} corresponding to matrix atoms (ϵ_{LJ}^{m}) and platelet atoms (ϵ_{LJ}^{p}) are kept as 0.1 and 1, and the value for interface (ϵ_{LJ}^{i}) is varied from 0.01 to 1. Computational tensile tests are carried out for different interface strengths using molecular dynamics (MD) method outlined in Chapter 2. The variation in the mechanical properties and the deformation mechanisms for various interface strengths are analyzed in the following sections. The simulated geometry of RSM and SSM models are same as that used in the study of basic deformation behavior (See Chapter 3) and the study of effect of strain rate (See Chapter 4). Further, as mentioned in Section 6.2, the same overlap length maintained between RSM and SSM model causes the AR of platelets in SSM model to be larger than the RSM model.

6.3.2.1 Mechanical Properties

Fig 6.5a to Fig 6.5d show the variation of mechanical properties such as Young's modulus, critical stress, flow stress and toughness respectively, for both RSM and SSM models. From Fig 6.5a, it is seen that the Young's modulus of the composite increases with interface strength for both the staggered arrangements. From Fig 6.5b, it can be observed that the critical stress of composite increases with the interface strength until the interface strength equals the matrix strength. Moreover, when the interface strength is greater than the matrix strength, the composite critical stress does not change considerably. From both Fig 6.5a and Fig 6.5b, it can also be seen that the trends in the variation of Young's modulus and strength of nanocomposite are similar for SSM and

RSM models, though the absolute values of Young's modulus and the strength are different. This difference could be due to the difference in aspect ratios of platelets for RSM and SSM models.

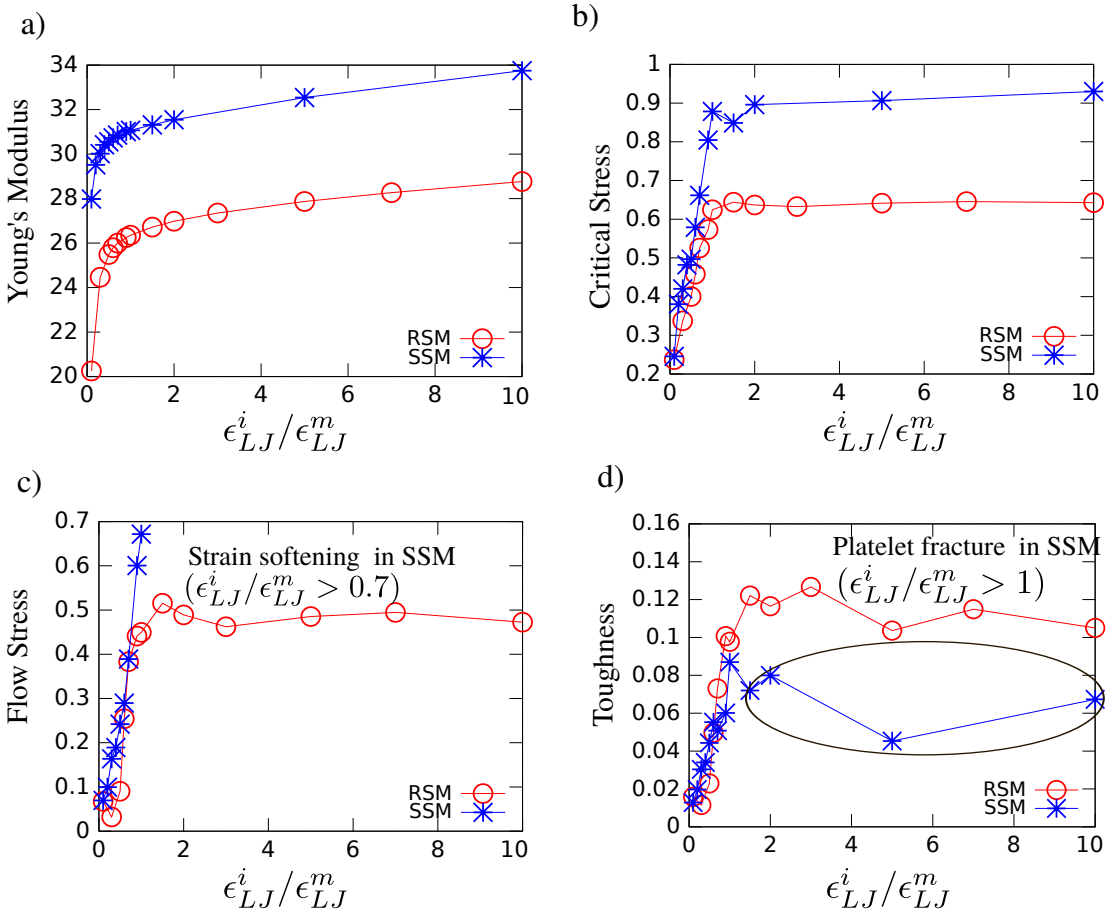

Figure 6.5 Variation of mechanical properties with the ratio of interface bond strength (ϵ^i_{LJ}) to matrix bond strength (ϵ^m_{LJ} is kept as 0.1) for RSM and SSM models: (a) Young's modulus, (b) critical stress, (c) flow stress, and (d) toughness.

Further, in the case of RSM model the flow stress and toughness initially increase with interface strength. When the interface strength is increased beyond that of matrix strength in RSM model, the flow stress and toughness remain a constant. In the case of SSM model, though initially the flow stress and toughness increase with interface strength, for $\epsilon^i_{LJ}/\epsilon^m_{LJ} > 0.7$ strain softening is observed and for $\epsilon^i_{LJ}/\epsilon^m_{LJ} > 1$ platelet fracture occurs in SSM model; these deformation mechanisms are discussed in detail in the next section. Therefore, flow stress for $\epsilon^i_{LJ}/\epsilon^m_{LJ} > 0.7$ is not shown in the figure. Moreover, the variation of toughness with interface strength is similar to that of the variation of flow stress in both the models. How the deformation mechanisms are

affected by different interface strengths will be discussed next.

6.3.2.2 Deformation Mechanisms

In this section, the deformation mechanisms occurring for different interface strengths are explored. Here, visual analysis is used to understand the mechanisms responsible for the variation in mechanical properties with different interface strength.

Though the mechanical properties increase when the interface strength is increased from $\epsilon^i_{LJ}/\epsilon^m_{LJ} > 0.1$ to $\epsilon^i_{LJ}/\epsilon^m_{LJ} \leq 1$, a change in deformation behavior is observed when the deformation mechanisms are compared between the interface strengths $0.7 \leq \epsilon^i_{LJ}/\epsilon^m_{LJ} \leq 1$ to that observed in $\epsilon^i_{LJ}/\epsilon^m_{LJ} < 0.7$. Based on the variation of mechanical properties with interface strength, and the variation of deformation mechanisms which is discussed in the following paragraphs, three interface strength regimes can be defined, for both RSM and SSM.

- Interface strength regime-1: $\epsilon^i_{LJ}/\epsilon^m_{LJ} < 0.7$
- Interface strength regime-2: $0.7 \leq \epsilon^i_{LJ}/\epsilon^m_{LJ} \leq 1$
- Interface strength regime-3: $\epsilon^i_{LJ}/\epsilon^m_{LJ} > 1$

The stress-strain graphs and associated deformations for various interface strengths are shown in Figs 6.6a to 6.6d, for the case of RSM model. For very low interface strengths, i.e., at interface strength regime-1 (refer Fig 6.6a for $\epsilon^i_{LJ}/\epsilon^m_{LJ} = 0.5$ and Fig 6.6b for $\epsilon^i_{LJ}/\epsilon^m_{LJ} = 0.6$), debonding at many places of interface are seen in the vertical as well as in the horizontal interfaces. This causes interface failure and very poor stress transfer, and consequent reduction in the stresses carried by the nanocomposites. At higher strains, cracks are observed in the matrix near the platelet tips along with pullout of the platelet. For an increased interface strength($\epsilon^i_{LJ} = 0.06$), critical stress and flow behavior improves (see stress-strain diagrams in Fig 6.6a and Fig 6.6b). Moreover, a small amount of dislocations are seen for this interface strength.

For the interface strengths $0.7 \leq \epsilon^i_{LJ}/\epsilon^m_{LJ} \leq 1$ i.e., at interface strength regime-2 (refer Fig 6.6c for ϵ^i_{LJ} equal to that of matrix strength), significant plastic deformation mechanisms such as nano-voids and nano-cracks are observed in the matrix for strain

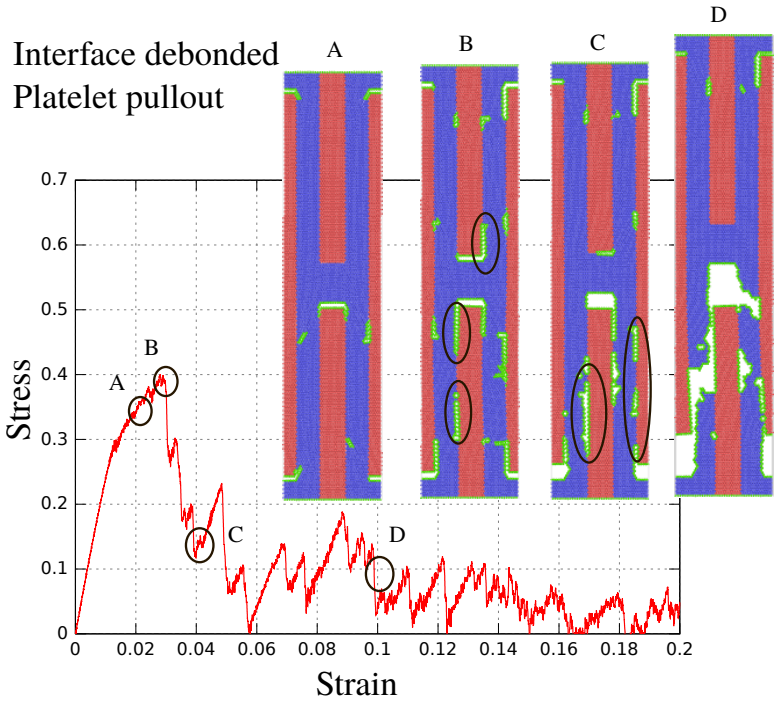

(a) $\epsilon^i_{LJ} = 0.05$ ($\epsilon^i_{LJ}/\epsilon^m_{LJ} < 0.7$)
Decohesions are marked with elliptic circles

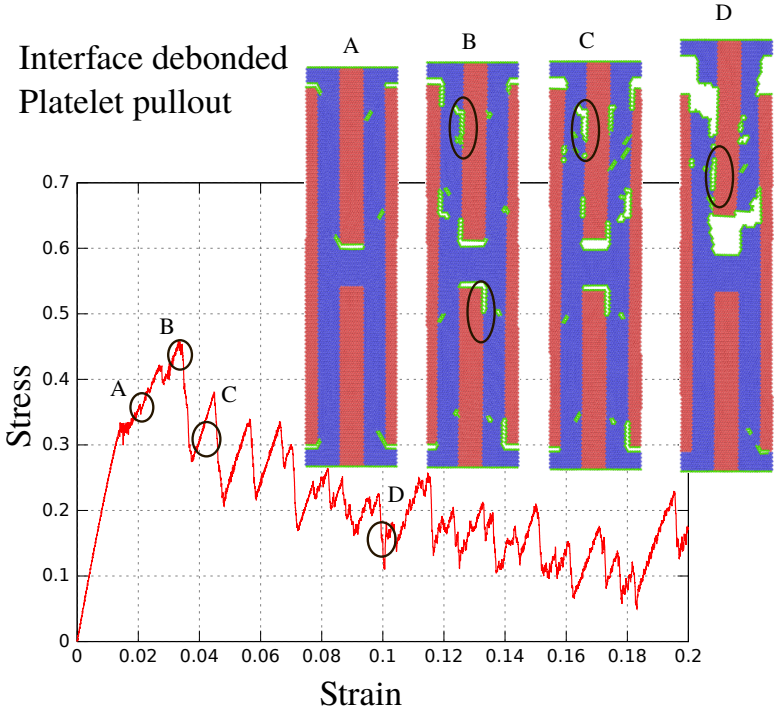

(b) $\epsilon^i_{LJ} = 0.06$ ($\epsilon^i_{LJ}/\epsilon^m_{LJ} < 0.7$)
Decohesions are marked with elliptic circles

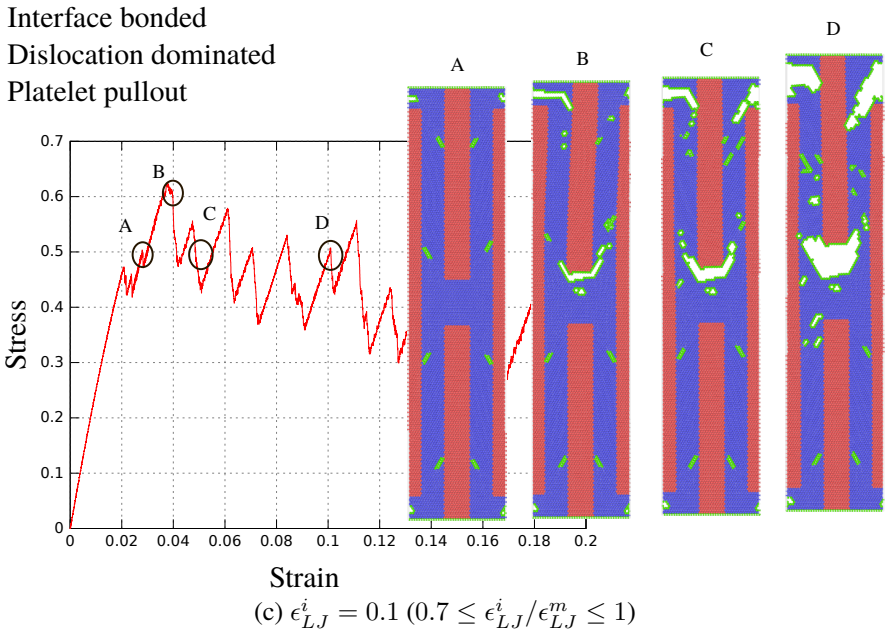

(c) $\epsilon^i_{LJ} = 0.1$ ($0.7 \leq \epsilon^i_{LJ}/\epsilon^m_{LJ} \leq 1$)

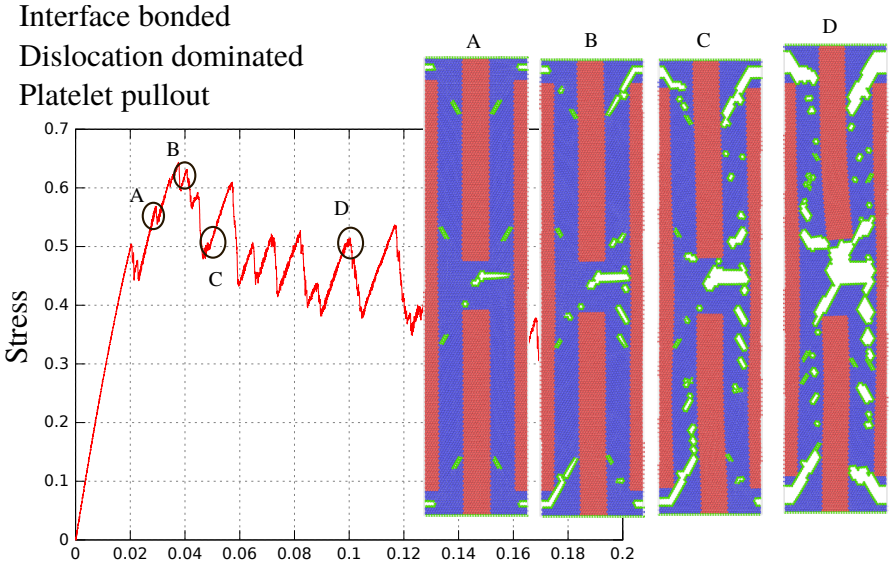

(d) $\epsilon^i_{LJ} = 1.0$ ($\epsilon^i_{LJ}/\epsilon^m_{LJ} > 1$)

Figure 6.7 Typical deformation processes of RSM model for different interface strengths along with associated stress-strain diagram. At low interface strength, low flow behavior is observed (see stress-strain diagram in a). Whereas, increase in interface strength leads to increase in flow behavior (see stress-strain diagram in b). Platelet sliding occurs in both the cases (a) and (b). High flow behavior is seen for high interface strengths as seen in stress-strain diagram of (c) and (d). Dislocation activities and cracks are observed in matrix at high interface strengths (in both c and d)

range of 4–10%. With increase in strain, cracks are observed in the matrix near the platelet tips. Thus, once the matrix has failed by various voids and cracks, pullout of platelet occurs due to the interfacial sliding and the elongation of the matrix crack that occurred at platelet tips.

For $\epsilon^i_{LJ}/\epsilon^m_{LJ} > 1$, at lower strains the deformation is similar to that of regime-2. However, at larger strains, the pull-out of platelets occurs due to the cracking of matrix region along interface rather than the elongation of cracks in the matrix near the platelet tip (refer Fig 6.6d). This cracking of matrix along the interface does not affect the flow behavior; this can be noted from the stress-strain diagrams shown in Fig 6.7 as well as from the plots of variation of flow stress with interface strength shown in Fig 6.5c.

Figs 6.8a to 6.8d show the stress-strain diagrams and associated deformations for various interface strengths for SSM model. For weak interface strengths ($\epsilon^i_{LJ}/\epsilon^m_{LJ} < 0.7$), stress-strain diagrams show good flow behavior, and flow stress increases with interface strength (compare Fig 6.8a, Fig 6.8b and Fig 6.5c). Moreover, debonding or decohesions of interface are observed at many places which are similar to that observed for RSM. Whereas, the SSM model shows good flow behavior compared to the RSM model in this interface strength regime-1.

Further, softening of the stress occurs in interface strength regime-2, i.e., $0.7 \leq \epsilon^i_{LJ}/\epsilon^m_{LJ} \leq 1$), (see Fig 6.8c). From the deformation plots, we can observe that decohesion of platelets is not observed in this regime similar to that RSM model. However, the softening occurs in SSM model; reasons for this are already discussed in Section 3.3 in detail. Moreover, platelet breakage is observed for interface strengths higher than the matrix strength (see Fig 6.8d). Therefore, it can be inferred that the weak interface is a requisite for platelets sliding to occur, and for better flow stress and toughness in SSM models which has been observed in many of the studies of biological nanocomposites as well (Buehler, 2007, 2010).

Here, we review the role of interface strength in the development of various deformation mechanisms in the nanocomposite models. It is seen that the critical interface strength ($\epsilon^{i,C}_{LJ}$) plays a major role on the deformation mechanisms. For $\epsilon^i_{LJ} < \epsilon^{i,C}_{LJ}$, the decohesion of interfaces and platelet sliding are observed. And, when $\epsilon^i_{LJ} > \epsilon^{i,C}_{LJ}$, the interface became strong enough to remain intact, which leads to the slipping of matrix

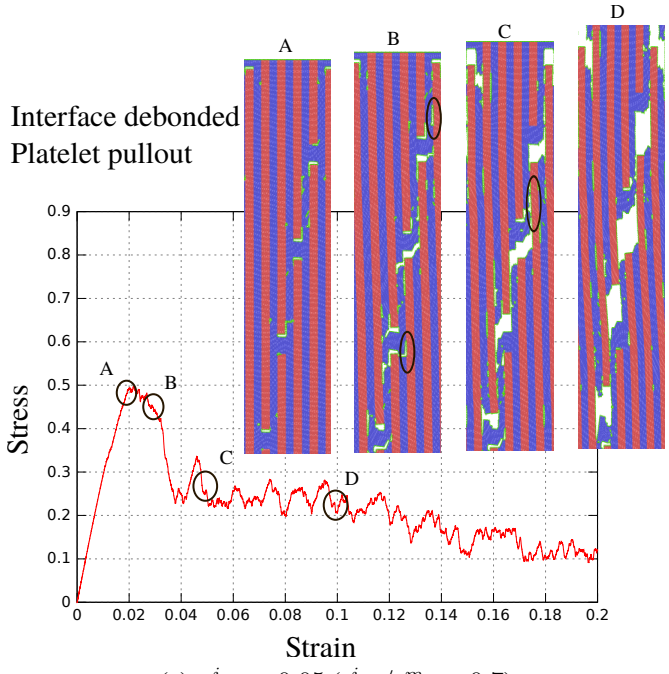

(a) $\epsilon^i_{LJ} = 0.05$ ($\epsilon^i_{LJ}/\epsilon^m_{LJ} < 0.7$)
Decohesions are marked with elliptic circles

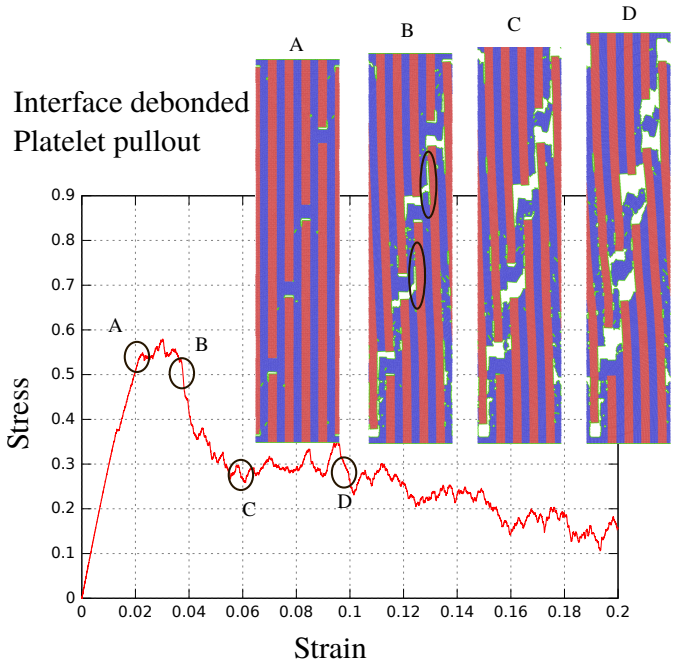

(b) $\epsilon^i_{LJ} = 0.06$ ($\epsilon^i_{LJ}/\epsilon^m_{LJ} < 0.7$)
Decohesions are marked with elliptic circles

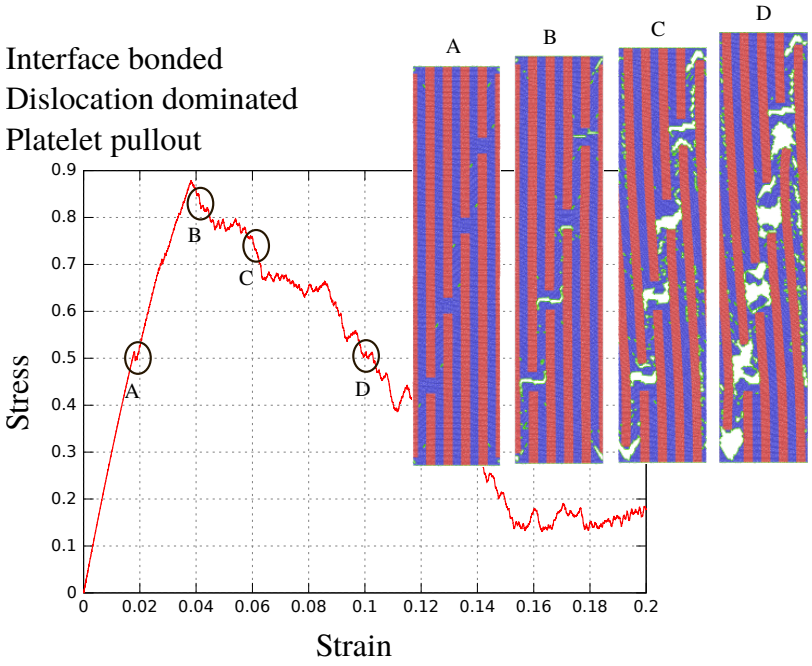

(c) $\epsilon^i_{LJ} = 0.1$ ($0.7 \leq \epsilon^i_{LJ}/\epsilon^m_{LJ} \leq 1$)

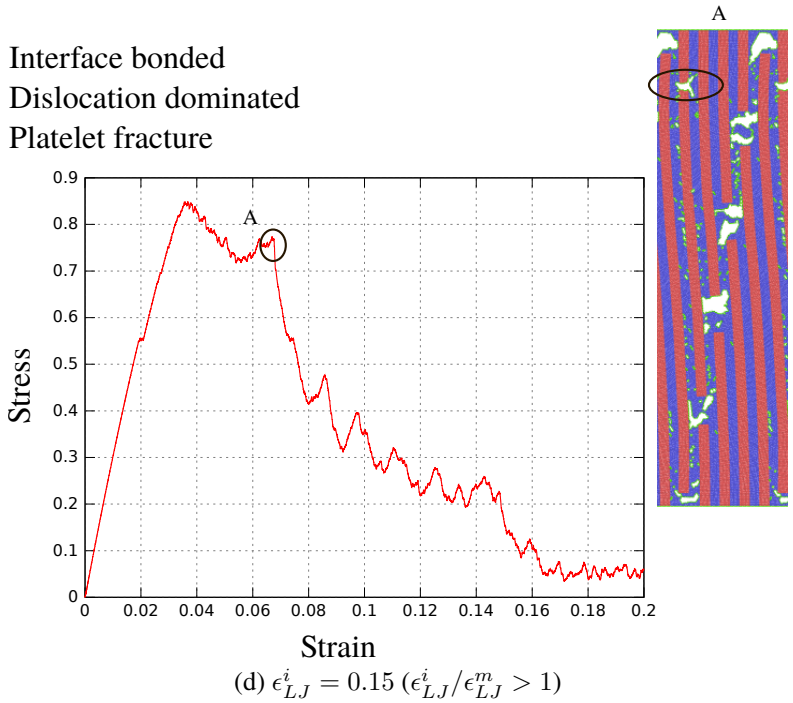

(d) $\epsilon^i_{LJ} = 0.15$ ($\epsilon^i_{LJ}/\epsilon^m_{LJ} > 1$)

Figure 6.9 Typical deformation processes in SSM model for different interface strengths along with associated stress-strain diagram. For $\epsilon^i_{LJ} < 0.07$,(a) and (b), good flow behavior is observed, though debonding or decohesions are observed at many places of interfaces. For $0.07 \leq \epsilon^i_{LJ} \leq 0.1$, strain softening occurs (c), and for $\epsilon^i_{LJ} > 0.1$, platelet fractures (d).

atoms and cracking of matrix.

The mechanical response of traditional microscale ceramic matrix composites is significantly affected by three parameters as follows (Faber, 1997): (a) Interface toughness–which needs to be kept low, in order to deflect matrix crack along interface and avoid platelet fracture. 2) Interfacial sliding stress–which should be small enough to increase the platelet pullout work and composite toughness, and (c) Lower thermal mismatch stress for avoiding platelet or matrix cracking. In this chapter, the effect of interface strength on the mechanical response of BMCs is studied; however, other physical parameters, such as thermal expansion mismatch and platelet roughness, play significant roles and need to be accounted for in the interfacial design of CMCs. The effect of these residual stresses and surface roughness are left for future studies.

6.4 Conclusion

Atomistic simulations are used to capture the influence of interface strength on the mechanical properties and deformation mechanisms of bio-inspired brittle matrix nanocomposites. The effect of interface strength on the mechanical behavior of both the regularly and stair-wise staggered models is studied.

The interface behavior is analyzed before studying the effect of interface strength on the nanocomposites. From this analysis, it is found that the depth up to which the interatomic force acts from the interface does not influence the interface behavior. Moreover, it is also found that a critical interface value ($\epsilon_{LJ}^{i,C}$) exists below which interface decohesion and platelet sliding occur and above which slipping of matrix atoms occurs.

Further, the significance of the reinforcement-matrix interface strength on the stiffening, strengthening and toughening of the bio-inspired brittle matrix nanocomposites is investigated through molecular dynamics simulations. Different regimes in interface strengths are found based on the different trends in mechanical properties and deformation mechanisms exhibited by the nanocomposites.

1) For low interface strength regime-1, interface fails; this leads to decohesion between the matrix and platelet atoms. This further leads to platelet pullout, without any plastic deformations such as interaction of dislocations and formation of cracks in the

matrix. Absence of these mechanisms leads to low mechanical properties. The mechanical properties increase with the interface strength in this regime

2) For intermediate interface strength regime-2 ($0.7 \leq \epsilon^i_{LJ}/\epsilon^m_{LJ} \leq 1$), various plastic deformation mechanisms such as nucleation of dislocations and creation of nano-voids and nano-cracks in the matrix occur. Moreover, platelet pullout occurs in addition to matrix cracking. This causes drastic increase in the flow stress and toughness for both the RSM and SSM models. These mechanical properties continue to increase with the interface strength in this regime.

3) For high interface strengths which are higher than the matrix strength, some of the deformation mechanisms remain similar to that observed in the regime-2 for example, various plastic deformation mechanisms in the matrix. However, pull-out in RSM model is accompanied by the fracture of matrix along the interface. The SSM model undergoes platelet fracture without significant plasticity. Therefore, the flow stress and toughness remain a constant for RSM model, whereas these properties are reduced or do not exist for SSM models.

Though the micro-scale CMC theory predicts the platelet fracture at higher interface strengths, the RSM model continues to show good flow stress and toughness even at these interface strengths. This is due to the deflection of cracks along the matrix which has a lower strength than the interface. However, this behavior is not observed in the SSM model, and it undergoes platelet fracture. This could be due to the notch effect created by the cracks in the matrix. The understanding of influence of interface strength on mechanical response as given in the present study would guide in the interface design and development of advanced man-made composites.

CHAPTER 7

Effect of Length scale

In this chapter, the effect of length scale on the mechanical behavior of bio-inspired brittle-matrix nanocomposites is investigated by atomistic simulations. The regularly staggered arrangement of stiff platelets reinforced in compliant matrix (RSM) is analyzed; this RSM model is inspired from the nanostructure of biological materials. The geometry of the RSM model is scaled proportionately in size and the variation in mechanical properties with length scale is explored. The present results are compared with that of the metallic matrix nanocomposites available in the literature. It is found that the number of lattice unit cells in the transverse directional gap between the platelets plays a major role in determining the critical length scale of nanocomposite materials. In the case of coherent interfaces, the critical length scale is obtained as five lattice unit cells in the matrix which is independent of the constituent materials used. However, for semi-coherent interface, the critical length scale is observed to be fourteen lattice unit cells. This investigation could provide guidelines for the design of tough ceramic matrix composites.

7.1 Introduction

Previous studies in this thesis have used the biomimetic structure in developing high-toughness ceramic matrix nanocomposites (CMNC). These ceramic composites showed ductile behavior, though their constituents are made of brittle materials. In this chapter, the effect of length scale on the mechanical behavior of ceramic matrix composites is investigated; this length scale is a peculiar characteristic applicable to nanoscale materials. The size dependent mechanical properties and plasticity have been of great interest to materials science research community in nanoscale materials, such as nanowires, nanopillars, nanolaminates, nanofilms, and nanocrystalline materials. The length scale of the intrinsic and extrinsic features of these materials play a major role in these materials to achieve superior mechanical behavior (Wu et al., 2012; Huang et al., 2011; Dao et al., 2007; Wolf et al., 2005; Wichmann et al., 2008). Though many bio-inspired

nanocomposites (Bonderer et al., 2008; Launey and Ritchie, 2009) have been fabricated, and their properties have been analyzed using many numerical and analytical methods (Begley et al., 2012; Broedling et al., 2008; Sen and Buehler, 2009; Anup et al., 2008), these studies have mainly focused on polymeric or metallic matrices. Studies which focus on the length scale effect of bio-inspired brittle matrix nanocomposites are not yet done. These studies are necessary not only to design the ceramic matrix nanocomposite materials but also to design the nanoscale building blocks of hierarchical composite materials.

Traditionally, Hall-Petch (HP) equation (Hall, 1951; Petch, 1953) is used to express the relation between the mechanical properties with the length scale of the materials. Initially, the HP equation was used to relate the yield stress with the grain size–which is the length between two grain boundaries of polycrystalline materials. Later it was extended to relate other mechanical properties with lengths measured between boundaries/interfaces introduced by different plastic deformations as well (Armstrong, 1970; Gil Sevillano et al., 1980; Xiao et al., 2001; Hansen, 2004). For nanocrystalline materials, the yield strength dramatically increases with decreasing grain size according to the HP relation. However, experiments show that below a critical grain size, the yield strength decreases with decreasing grain size. The critical grain size is usually observed to be in few tens of nanometers. To understand the transition from strengthening to softening of these nanocrystalline materials with decreasing grain size, many computer simulations were performed. It was found that this transition is due to the crossover from dislocation dominated deformation mechanisms at larger grain sizes to grain boundary mediated deformation mechanisms at smaller grain sizes. The dislocation emission is easier at larger grain sizes, and in contrast the grain boundary sliding becomes easier at smaller grain sizes (Kumar et al., 2003; Meyers et al., 2006). Moreover, many theoretical and experimental studies have concluded that the collective motion of dislocation avalanches interacting with the grain boundary results in the HP behavior. And the loss of this collective behavior of dislocations results in softening in small grain sizes (Louchet et al., 2006).

In the present study, the yield stress and flow stress are related to the spacing between the platelet-matrix interfaces. In nanocomposites such as considered in the present work, the matrix phase is softer than the platelet and hence matrix under-

goes significant plastic deformation. Therefore for such nanocomposite materials, the spacing between the platelets was taken as the length scale factor in the HP relation (Broedling et al., 2008; Sen and Buehler, 2009). Previously, Broedling et al. (2008) studied metallic nanocomposites made of hard Ni platelets embedded in soft Al matrix. They showed that different deformation mechanisms such as dislocation activities, interfacial slip, and decohesion occurs at all length scales. According to their study, the dominant deformation mechanism was dislocation dominated at large length scales and interfacial slip dominated at small length scales. Further, they observed that the flow strength follows the normal HP relation during dislocation dominated length scales and inverse HP relation at interfacial slip dominated length scales. Sen and Buehler (2009) studied the effect of length scale on the flow strength of the composite by using model EAM potentials. They showed that the interfacial strength is a key parameter that determines a critical length scale, at which the shift in dominant deformation mechanism occurs and also the maximum flow strength is obtained. Both Broedling et al. (2008) and Sen and Buehler (2009) analyzed metallic matrix nanocomposites (MMNC). However, the length scale effect on brittle matrices is still to be explored which is ventured in this chapter.

Moreover, in the present study, the mechanical behavior of the biomimetic brittle matrix composites is analyzed for different length scales. For this purpose, molecular dynamics (MD) simulations are used. MD simulations have been extensively used in studying atomistic plastic deformation mechanisms (Zhang et al., 2016a; Pei et al., 2015). As explained in the introduction and methodology of the thesis in Chapter 1 and Chapter 2, both the matrix and platelets are modeled as brittle materials, in order to study generic behavior of ceramics matrix composites. This study would be useful in transferring the design principles of biological materials to develop high performance engineering materials. The methodology is explained in Section 7.2. The results and discussion along with comparison of other findings in the literature are done in Section 7.3. The main conclusions are presented in Section 7.4.

7.2 Methodology

As mentioned in the Chapter 2, the platelets are stiff, strong and brittle. In contrast, the matrix is compliant, weak and brittle. Two dimensional hexagonal crystal lattice and LJ interatomic potential are used to simulate these brittle constituents. Further, the values of ϵ_{LJ} for platelet, matrix and their interaction are chosen as 1, 0.1 and 0.1 respectively. This leads to the strength and modulus values of platelet 10 times that of matrix. The interface condition resulting from setting $\epsilon^{i}_{LJ} = 0.1$ closely resembles that of perfect bonding (discussed in Chapter 6); therefore, this value is used for interaction in this chapter. The value of σ_{LJ} is kept unity for all the constituents to maintain uniform lattice structure and coherent interface. These values of σ_{LJ} and ϵ_{LJ} are representative values used to provide different mechanical behavior for the constituents. It is also to be noted that the reduced units are used.

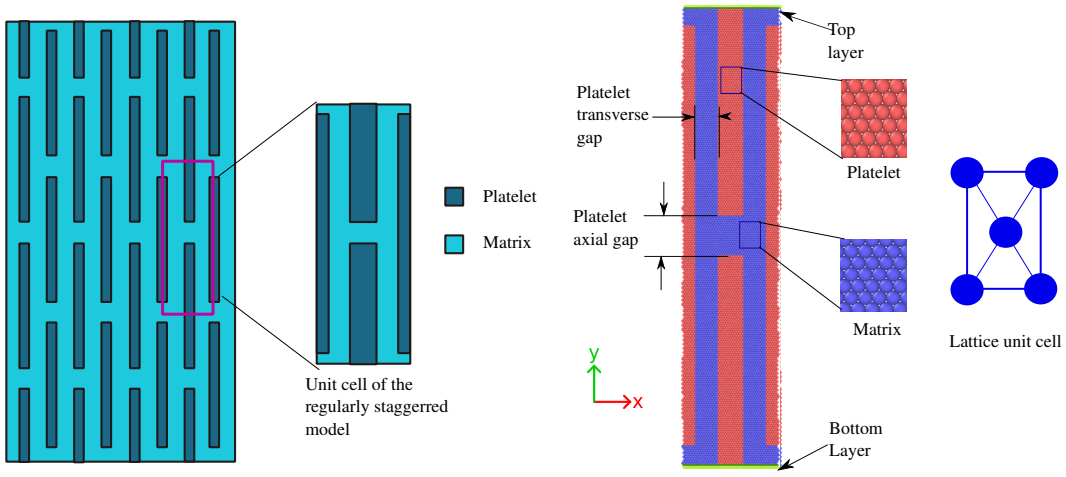

Figure 7.1 Details of the simulated model: (a) schematic diagram of the regularly staggered model (RSM) inspired from nacre and its unit cell, (b) atomistic model of the RSM and lattice unit cell

The nanocomposite model inspired from the nanostructure of nacre is shown in Fig 7.1a. The atomistic model built in LAMMPS is shown Fig 7.1b. The unit cell of the regularly staggered model and lattice unit cell are also shown in the figure. Nanocomposite models are built with platelets reinforced in the matrix. The platelets are made with 10 atoms in thickness. The platelet axial gap has 10 atoms. The space between platelets in X direction is uniformly made with 10 atoms of the matrix. Only RSM

model is analyzed in this chapter, and the platelets are made with 100 atoms along the length (Refer Fig 7.1 for nomenclature of the nanocomposite structure). The ratio of the number of atoms in the platelet thickness, platelet spacing, platelet axial gap and platelet length is kept as $1 : 1 : 1 : 10$. The ratio is referred to as the "overall ratio". Different models are created with the same "overall ratio" maintained, while the number of atoms in the platelet thickness (K) is varied from 2 to 30. This means that when the value of K is 2, the platelet thickness has two atoms and the platelet length has 20 atoms. Further modeling and other details about the computational uniaxial tensile test performed is explained in Chapter 2. All simulations were carried out using parallel molecular dynamics code LAMMPS (Plimpton, 1995). The open visualization tool (OVITO) is used to visualize MD data and generate snapshots (Stukowski, 2010).

7.3 Results and Discussion

The stress-strain graphs are obtained from the molecular dynamics simulations. A representative stress-strain curve is shown in Fig 7.2a for the length scale of K11 and the corresponding deformation processes observed are shown in the Fig 7.2b–e. This figure is used to explain how we obtain mechanical properties. Here, we briefly review the calculation of mechanical properties; more details are available in Section 2.3.1. The yield stress is taken as the stress required for the nucleation of dislocation. Comparing the deformation plots with the stress-strain diagram, it is seen that the point at which the first drop in stress (denoted by A in Fig 7.2a) occurs corresponding to the nucleation of dislocations (see subplots b and c of Fig 7.2). Therefore, yield stress is measured as the stress at point A. The flow stress is calculated as average stress in the 6% to 8% strain where the model undergoes significant plastic deformation mechanisms; it can be seen from the Fig 7.2d and Fig 7.2e that various plastic deformations such as dislocation interactions and matrix cracks are observed at points 6% (point C) and 8% (point D) strains. Thus both the stress-strain diagram and the deformation plots are used to obtain the mechanical properties.

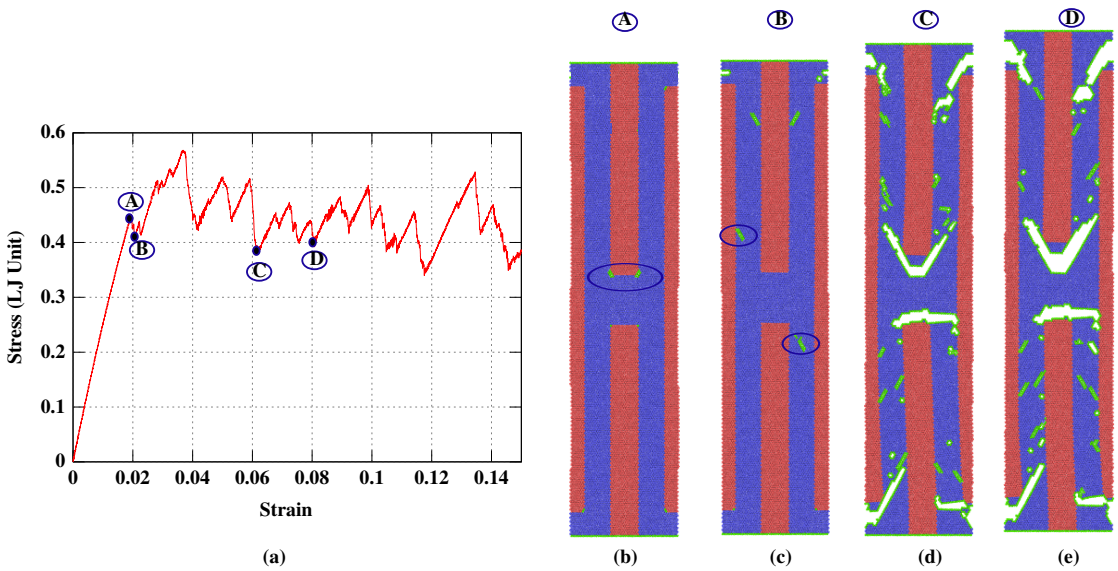

Figure 7.2 Typical stress-strain diagram of the nanocomposite for the length scale of 11 (subplot a) and associated deformation behavior (subplot b–e) obtained using MD simulations. The first drop in the stress (points A and B in subplot a) which corresponds to the first nucleation of dislocation at the platelet tips can be understood from subplot b and c; elliptical circles in these subplots indicate the emission of dislocations. The deformations observed at the strain of 6% (point C) and 8% (point D) strain values are shown in subplot d and e respectively.

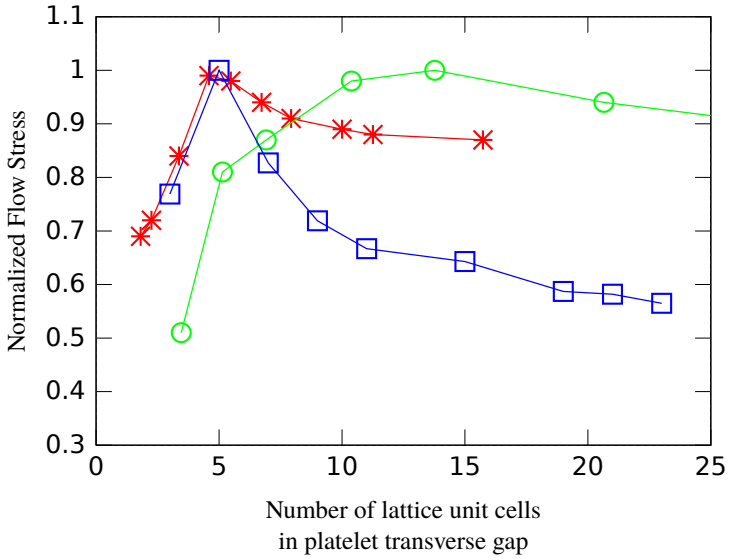

Figure 7.3 Variation of flow stress with different length scales. Blue squares show the present results obtained for the brittle matrix nanocomposite. Both the normal H-P behavior and inverse H-P behavior are seen. Red stars show the results of metallic matrix nanocomposite with coherent interface (Sen and Buehler, 2009). Further, green circles show the results of metallic matrix nanocomposite with semi-coherent interface (Broedling et al., 2008).

7.3.1 Flow Stress

The variation of flow stress for different length scales of the regularly staggered model is shown in Fig 7.3. The size of the model is expressed in terms of the number of lattice unit cells of atoms in the matrix of the platelet transverse gap region (see Fig 7.1). The flow stress is normalized with respect to the maximum flow stress attained by the model. This normalization is beneficial for comparing the results of the present study with that of the literature. From the Fig 7.3, it is observed that compared to the biggest model studied, the flow stress initially increases with decreasing size. However, after a critical length scale, the flow stress decreases with decrease in size of the model. This critical value is obtained as five lattice unit cell in the present study and referred to as the critical size ($K_c = 5$).

The increase in the flow stress with decrease in size is similar to that behavior observed in the polycrystalline materials, popularly known as Hall-Petch (HP) behavior. Moreover, the decrease in the flow stress when the size is less than a critical value is also observed in nanocrystalline materials. Therefore, the general trend in the variation of flow stress with size is similar to that of the polycrystalline materials (Schiøtz et al., 1998; Meyers et al., 2006). Moreover, the present results are also compared with studies on length scale effects of bio-inspired metallic nanocomposites by Broedling et al. (2008) and Sen and Buehler (2009). The critical size predicted by the present study matches with the results of Sen and Buehler (2009), and deviates significantly with the work of Broedling et al. (2008). Sen and Buehler (2009) used a coherent interface similar to that of the present work, and hence this may have resulted in similar values of critical size. In contrast, the semi-coherent interface used in the work of Broedling et al. (2008) could have caused the huge deviation in the critical size.

Further, the fraction of the interface over the total volume of the nanocomposite (which is calculated as the total length of the interface divided by the total area of the model in the two dimensions) is plotted against the number of lattice unit cells in the platelet transverse gap as shown in the Fig 7.4. From the Fig 7.4, it is found that the fraction of interface volume increases as the length scale of the model is decreased. Further, an interface volume fraction of about 20% is observed at the critical length scale of 5 lattice unit cells, which is obtained in the present study.

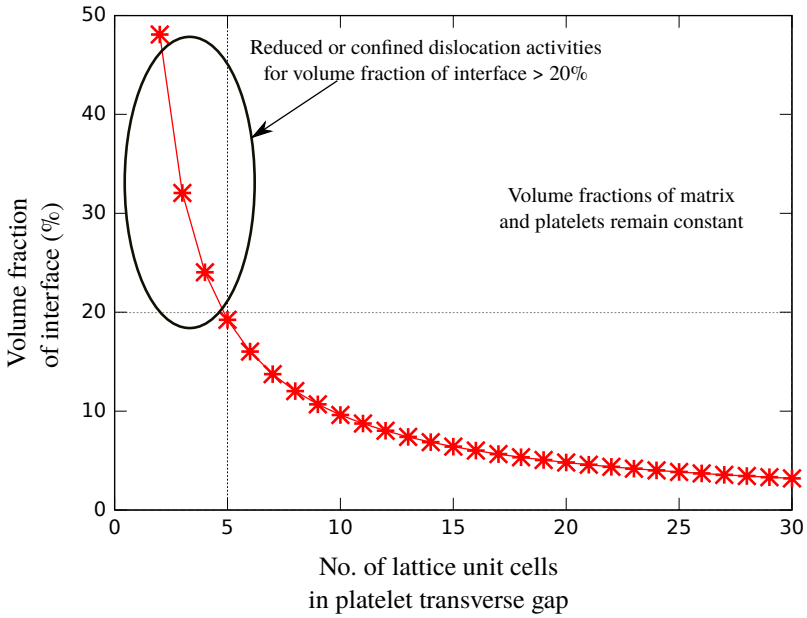

Figure 7.4 Variation of volume fraction of interface with different length scales.

From the analyses carried out in the previous chapters of the thesis (See discussions in Chapters 3, 5 and 6, it is clearly understood that the flow behavior of the nanocomposite materials is due to the combination of dislocation activities in the bulk matrix material and the pull-out platelet.

At larger length scales ($K \geq 5$), increase in flow stress is observed with decrease in length scale. The reason for this behavior is explained here. The volume fraction of interface could indicate the contribution of the interface to the flow stress of the nanocomposite material. On reducing the length scales, the volume fraction of matrix (55%) and platelets (45%) remain a constant and volume fraction of interface increases steadily. Therefore, the stress required for interfacial sliding increases as the increase in the interfacial volume fraction. Therefore, this interfacial volume fraction could be primarily responsible for any differences in the plasticity.

At smaller length scales ($K \leq 5$), decrease in the flow stress is observed with decrease in length scale. The reason for this behavior is explained here. When the volume fraction of interface increases above 20% which occurs when the length scale is smaller than 5 lattice unit cells, it is expected that the flow stress should increase due to the increase in the volume fraction of interface. Rather, the dislocation activities get reduced or arrested (This is observed from the study of deformation mechanisms, see

Section 7.3.3). This kind of behavior is referred to as geometric confinement where breakdown of dislocation activity occurs at small length scales (Sen and Buehler, 2008; Libonati et al., 2013). Therefore, the number of lattice unit cells in the platelet transverse gap determines the flow behavior at smaller length scales.

7.3.2 Yield Stress

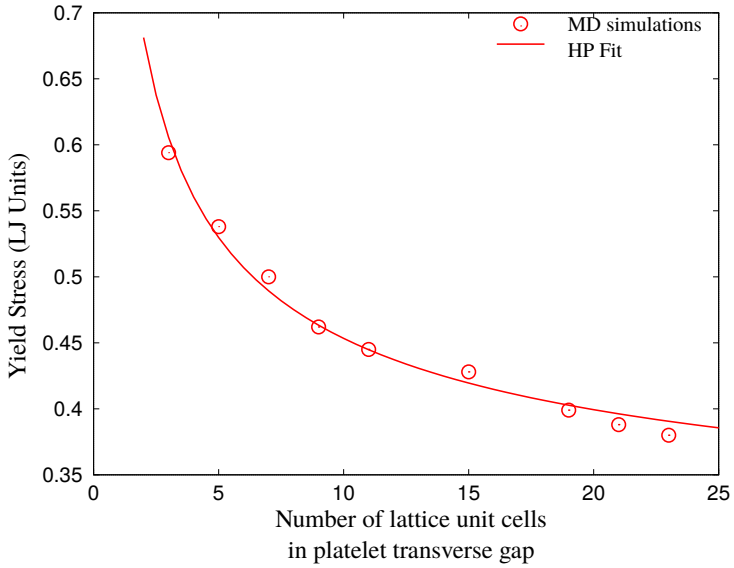

Figure 7.5 Variation of yield stress with different length scales. Yield stress shows H-P behavior and does not show inverse H-P behavior.

Fig 7.5 shows the variation of the yield stress for different sizes of the nanocomposite model. Monotonic increase of yield stress is observed with decrease in size. Moreover, the HP curve fitted to the yield stress is also shown in the Fig 7.5. It is observed that the yield stress follows the HP relation. Though flow stress follows inverse HP behavior beyond a critical size, the yield stress does not show any inverse HP behavior. This behavior of brittle matrix nanocomposites is in contrast to other nanocrystalline materials, which show an inverse HP effect in the case of yield stress (Schiøtz et al., 1998).

Moreover, it is to be noted here that different methods are used in the literature for measuring the values of flow stress and yield stresses. For example, Broedling et al. (2008) calculated the flow stress as the average stress in the strain range of 6–8% of total strain and Sen and Buehler (2009) used the average stress in the strain range of 15–20% of total strain. Similarly, flow stress is measured as average value of stress in the 0–

4% and 5–15% of inelastic strain ranges in the case of nanocrystalline BCC iron (Jeon et al., 2011). Schiøtz and Jacobsen (2003) used the average stress in the strain interval of 7–10% as the flow stress in the study of nanocrystalline Cu. Pan et al. (2008) used the 5% offset stress as the flow stress in the study of nanocrystalline Ta. In the present study, the average stress in the range of 6–8% strain is taken as flow stress, where the plasticity due to dislocation activities in the matrix and the plasticity due to pullout of platelets occur simultaneously. In the case of yield stress, many researchers have taken the 0.2% offset stress as the yield stress. However, in the present study, the stress at which the first nucleation of dislocations occurs is taken as the yield stress which is physically meaningful. Therefore, it seems that there is not a unified approach in the measurement of mechanical properties studied here. This could significantly affect the critical size and inverse Hall-Petch behavior of materials.

7.3.3 Deformation Mechanisms

In this subsection, the deformation mechanisms observed for smaller and larger length scales are discussed. In order to analyze the difference in the deformation mechanisms, deformed shape for each case, one with length scale of K=21 which is larger than critical length scale (K_c=5), and another with the length scale of K=3 which is smaller than critical length scale (K_c=5) are analyzed. Fig 7.6 shows the deformation observed at various strains for K=21 model and Fig 7.7 shows the deformation observed at various strains for K=3 model.

Fig 7.6 shows the deformation mechanisms at larger length scales. Here, large amount of dislocation activities and cracks are observed. Further, interfacial sliding is seen due to the pullout of platelets, which are similar to that discussed in previous Chapters 3, 5 and 6. Whereas for smaller length scale, from Fig 7.7, it can be observed that the dislocations are emitted from the platelet tips which are similar to that of larger length scales as discussed in previous chapters. However, these emitted dislocations are arrested at the interface. This phenomenon is referred to as geometric confinement. Moreover, the voids crated at the axial gap region grow into cracks. These cracks are arrested at the interface. Further, pullout of platelet occurs after deflection of the cracks along the interface. The geometric confinement event–the breakdown of dislocation ac-

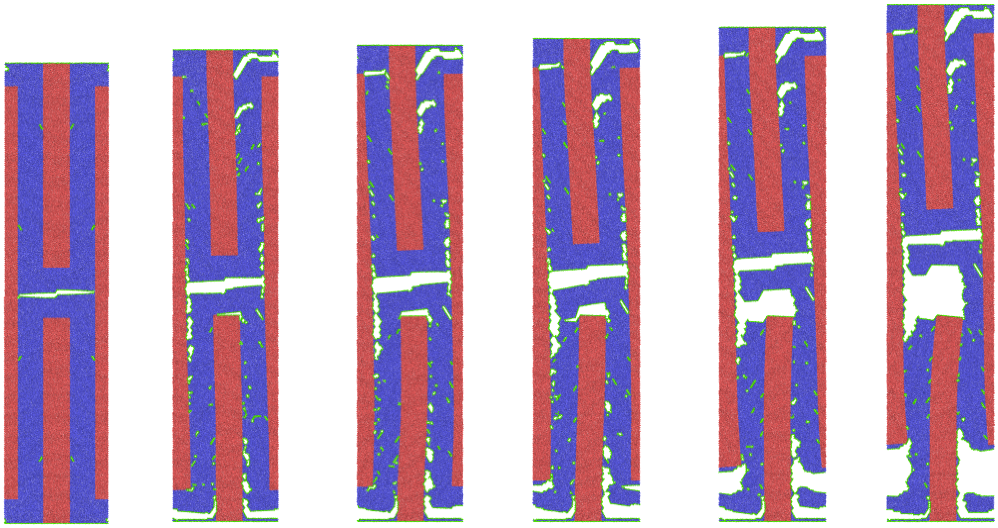

(a) 0.025 (b) 0.05 (c) 0.06 (d) 0.075 (e) 0.1 (f) 0.15

Figure 7.6 Deformation mechanisms at the length scale of K=21. Snapshots of deformation plots at various strains are shown. Dislocation activities combined with platelet pullout is observed similar to that in other studies discussed in previous chapters of the thesis.

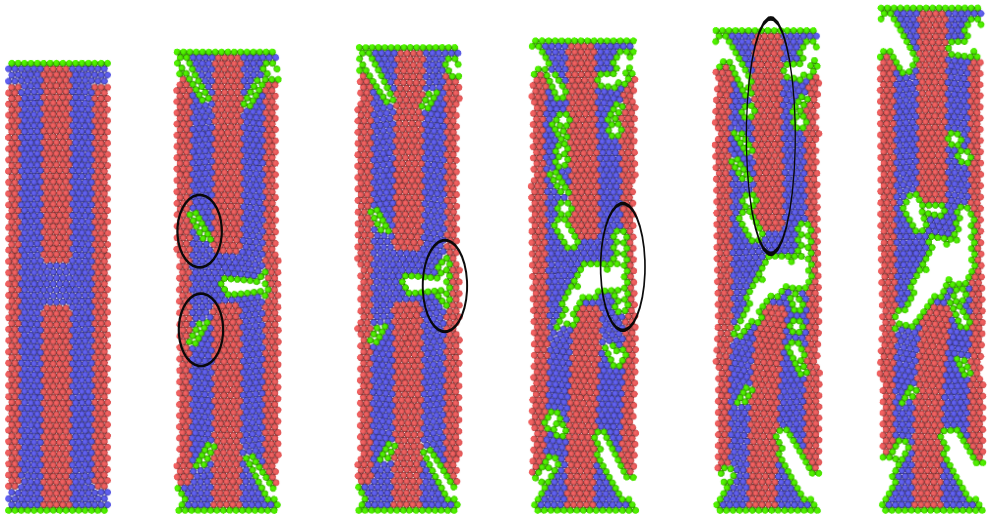

(a) 0.025 (b) 0.05 (c) 0.06 (d) 0.075 (e) 0.1 (f) 0.15

Figure 7.7 Deformation mechanisms at the length scale of K=3. Snapshots of deformation at various strains are shown. Initial model is shown in subplot (a), and the arrests of dislocations are marked with elliptical circles in subplot (b). The subplots (c) and (d) show the deflection of crack at the interface marked with elliptical circles. Platelet pull-out occurs due to platelet sliding along the interface as shown in (e). Further pullout due to elongation of platelet tip matrix crack is shown in (f).

tivities at smaller length scale, has also been reported in other studies as well (Broedling et al., 2008; Sen and Buehler, 2008). This geometric confinement of dislocations activities leads to reduction in the flow stress at smaller length scales.

7.4 Conclusion

In this chapter, the effect of length scale on the mechanical properties and deformation mechanisms of bio-inspired, brittle-matrix, regularly staggered nanocomposite model is studied. The length scale of the model is varied by proportionately increasing the number of atoms in all the characteristic dimensions of the nanostructure. Therefore, the geometrical parameters such as platelet aspect ratio and volume fractions of matrix and platelets are maintained constant. The flow stress and yield stress are calculated for different length scales of the model using molecular dynamics (MD) simulations. Moreover, in the present study the size of the model is expressed in terms of the number of lattice unit cells in the platelet transverse gap of the nanocomposite model.

From our study, it is found that the flow stress of the nanocomposite initially increases with decrease in size of the model, and below a critical size the flow stress decreases with further decrease in size of the model. At this critical size, the nanocomposite reaches its maximum flow stress. This observed variation in flow stress in the nanocomposite model is similar to that of normal and inverse Hall-Petch (H-P) relations which exist between the strength and grain size of nanocrystalline single phase materials. In the present study, the critical length scale at which the transition occurs is found as five lattice unit cells. Interestingly, this critical value is the same for the case of ductile nanocomposites with coherent interface obtained from the literature. In our study, it is also found that the yield stress shows only normal H-P behavior in all the length scale studied, though the flow stress shows both the normal and inverse H-P relations with size of the model. Further from the analysis of deformation mechanisms, it is found that though platelet pullout occurs at all length scales, large amount of dislocation activities are observed at larger length scales, whereas reduced dislocation activities due to geometric confinement of dislocations is observed at smaller length scales.

Moreover, the model considered in our present study is made up of entirely defect-free crystal structure. Whereas, defects are present in actual materials and that can

substantially affect the mechanical behavior of materials. Similarly, different interface morphologies and different interface strengths can significantly affect the critical length scale of the model. Therefore, future studies will be required to investigate the effects of the defects, interface strength and interface morphology on the overall mechanical behavior of the nanocomposites.

CHAPTER 8

Conclusions and Future Work

This dissertation presents the works carried out to understand the mechanical behavior of bio-inspired brittle matrix nanocomposites: the regularly staggered (RSM) and stair-wise staggered (SSM) arrangements of stiff platelets reinforced in compliant brittle matrix. Computational uniaxial tensile tests using atomistic simulations are carried out to examine the mechanical behavior of these brittle matrix nanocomposites. The present work documents the effect of strain-rates, the effect of aspect ratio of platelets, the effect of interface strength and the effect of length scale on the mechanical properties and deformation mechanisms of these two nanocomposite models. This chapter is the last chapter of the thesis. In this chapter, the summery of key findings are listed in first section and the works that can be extended from the thesis are discussed in the second section.

8.1 Conclusions

Mechanical behavior of bio-inspired brittle matrix nanocomposite is studied using two dimensional hexagonal lattice Lennard-Jones solid. The differences and similarities between the regularly staggered (RSM) and stair-wise staggered (SSM) models are also obtained. The MD simulation methodology is validated using the results available in the literature for homogeneous two dimensional Lennard-Jones solid as well as using the theoretical results based on atomistic elasticity concepts (Buehler, 2008). The key findings obtained from this work are listed below.

- RSM model shows continuous flow behavior. In contrast, SSM model shows strain softening behavior. The arrest of central crack symmetrically on both sides of the platelet overlap region in the RSM model causes continuous flow behavior. Whereas, the rapid crack growth in one side of the overlap regions causes strain softening in the SSM model.

- The influence of strain rate is studied for a wide spectrum of strain rate from 10^{-6} to 10^{-1} in reduced units (which approximately equals to strain rate of $10^{6}s^{-1}$ to $10^{11}s^{-1}$ in SI units). Three strain-rate regimes which are separated by two critical strain rates are found. The difference in the platelet arrangement has little influence on deformation mechanisms under varying strain rates. The deformation mechanisms observed for $\dot{\varepsilon}_{yy} \leq 10^{-5}$ are similar to that observed in quasi-static simulations of bio-inspired nanocomposites available in the literature (Broedling et al., 2008). In the subsequent chapters, further analyses are performed at these low strain rates. Moreover, deformation mechanisms such as amorphous deformation and direct debonding of platelets are observed as the strain rate is increased. Moreover, strain rate effects are explored under adiabatic conditions and shock wave loadings. It is observed that the critical strain rates are reduced by one order of magnitude, based on the similar changes in the deformation mechanisms.

- The aspect ratio (AR) of platelets is varied, and the resulting changes in the mechanical properties and deformation behavior are studied. For RSM model, the existence of a critical AR is found up to which the increase in AR results in increase in the strength of the composite and above which the strength remains a constant. Further, the deformation mechanism changes from platelet pullout to platelet fracture at this critical AR. In contrast, there exist two critical ARs for SSM model. The change in deformation mechanism similar to that of RSM is observed at smaller of the two critical ARs and the increase in strength is found up to the larger of the two critical ARs. Moreover, a new theoretical model is developed to predict the strength of the SSM models based on the simulation results.

- In order to study the effect of various type of interface on the overall mechanical behavior of nanocomposite materials, the binding energy of interface atoms is varied and the change in the mechanical behavior is studied. At low interface strengths, deformation mechanisms such as early interface debonding and platelet pullout without any dislocation activities in the matrix occur. This behavior leads to low mechanical properties in both the RSM and SSM models. At intermediate interface strengths (when interface strength equals to 50% – 100% of matrix

strength), platelet pullout occurs accompanied by nucleation of dislocation from platelet tips and the creation of voids in the matrix. These mechanisms cause a drastic increase in the flow strength and toughness in both the RSM and SSM models. At higher interface strengths, the deformation mechanisms and mechanical properties remains unaffected in the RSM models. However, the platelet fracture occurs in the SSM model and flow strength and toughness reduce drastically.

- Finally, length scale effect which is a peculiar characteristic of nanoscale materials is studied for RSM model. The number of lattice unit cells in all characteristic dimensions of geometry is proportionately scaled. The size of the model is taken as the number of lattice unit cells in the platelet transverse gap. The flow stress shows the Hall-Petch relation, i.e., strengthening with decreasing size as well as inverse Hall-Petch relation, i.e., softening with decreasing size below a critical size. The critical size is found as five lattice unit cells in the platelet transverse gap. This is consistent with the results of the bio-inspired metallic matrix nanocomposite with coherent interface available in literature.

Though two dimensional models are used in this thesis which are simplification of real three dimensional systems, a separate three dimensional analysis, which is carried out using the LJ parameters same as that of used in 2D models, showed that the 2D models can indeed reproduce the results qualitatively similar to that of 3D models. Moreover, in the thesis, the binding energy of interface atoms is taken to be equal to that of matrix atoms. Consequently, a strong, perfect and coherent interface is used in all the analyses carried out. However, a separate study on effect of interface is studied to understand its influence (See Chapter 6).

Moreover, these nanocomposite materials show large amount of plastic deformation for large strain levels despites its brittle constituents. Therefore, nanocomposites materials made of brittle materials like ceramics could lead to a good amount of ductility and toughness. These studies enhance our knowledge in the deformation mechanisms of bio-inspired nanocomposites and could help in building advanced engineering materials.

8.2 Recommendations for Future Work

In the previous section, the important findings obtained from this work through the atomistic simulation of bio-inspired brittle matrix nanocomposite models were discussed. In this section, some discussions on future extensions of this work are given. The possible extensions of this work are listed below.

- In the present studies, we have considered only the uniaxial loading along the platelet length directions. Therefore, this present work can be extended to loading in other directions, such as shear and biaxial loading.

- As a preliminary work, the coherent interface is considered in the length scale effect carried out in Chapter 7. However, the effect of semi-coherent and incoherent interface on the critical length scale of the nanocomposite models can be studied further.

- The role of different interface strengths on the value of critical length scale needs to be analyzed in future studies.

- In this thesis, mechanistic based theory is developed to understand the effect of platelet aspect ratio, using the results obtained from MD simulations. Further, mechanistic theories can be developed to understand the effect of interface strength as well as the effect of length scale.

- In the present work, defect free crystal structures are considered which causes the dislocations being predominantly nucleated from the interface of the constituents. However, the actual engineering materials possess various defects in their crystal structures. These defects could affect the deformation mechanisms as well the stress strain response. Presence of these defects can lead to more dislocation activities, reduction in stress levels and increase in toughness. The effects of these defects could be considered in further studies.

- Though generic understanding has been gained through the present work, the question of exactly how different ceramic materials as constituents of the nanocomposite materials can be developed into superior materials needs to be further analyzed with realistic potentials.

REFERENCES

1. Abraham, F. F. (1996). Dynamics of brittle fracture with variable elasticity. *Phys. Rev. Lett.*, *77*, 869–872.

2. Abraham, F. F. (2001). The atomic dynamics of fracture. *J. Mech. Phys. Solids*, *49*, 2095–2111.

3. Abraham, F. F., Brodbeck, D., Rudge, W. E., and Xu, X. (1997). A molecular dynamics investigation of rapid fracture mechanics. *J. Mech. Phys. Solids*, *45*, 1595–1619.

4. Abraham, F. F., Walkup, R., Gao, H., Duchaineau, M., Rubia, T. D. D. L., and Seager, M. (2002a). Simulating materials failure by using up to one billion atoms and the world's fastest computer: Brittle fracture. *Proc. Natl. Acad. Sci. U. S. A.*, *99*, 5777–5782.

5. Abraham, F. F., Walkup, R., Gao, H., Duchaineau, M., Rubia, T. D. D. L., and Seager, M. (2002b). Simulating materials failure by using up to one billion atoms and the world's fastest computer: Work-hardening. *Proc. Natl. Acad. Sci. U. S. A.*, *99*, 5783–5787.

6. Ahmad, I., Cao, H., Chen, H., Zhao, H., Kennedy, A., and Zhu, Y. Q. (2010). Carbon nanotube toughened aluminium oxide nanocomposite. *J. Eur. Ceram. Soc.*, *30*, 865–873.

7. Aikin, R. (1997). The mechanical properties of in-situ composites. *JOM*, *49*, 35–39.

8. Akisanya, A., and Fleck, N. (1992). Brittle fracture of adhesive joints. *International Journal of Fracture*, *58*, 93–114.

9. Anderson, T. (1995). *Fracture Mechanics: Fundamental and Applications*. New York: CRC Press.

10. Anup, S., Sivakumar, S. M., and Suraishkumar, G. K. (2007). Structural arrangement effects of mineral platelets on the nature of stress distribution in bio-composites. *Comput. Model. Eng. Sci.*, *18*, 145–153.

11. Anup, S., Sivakumar, S. M., and Suraishkumar, G. K. (2008). Influence of relative strength of constituents on the overall strength and toughness of bone. *J. Mech. Med. Biol.*, *8*, 527–539.

12. Anup, S., Sivakumar, S. M., and Suraishkumar, G. K. (2010). Influence of viscoelasticity of protein on the toughness of bone. *J. Mech. Behav. Biomed. Mater.*, *3*, 260–7.

13. de Arcangelis, L., Redner, S., and Herrmann, H. J. (1985). A random fuse model for breaking Process. *J. Phys. - Lett.*, *46*, 585–590.

14. Armstrong, R. W. (1970). The influence of polycrystal grain size on several mechanical properties of materials. *Metall. Mater. Trans.*, *1*, 1169–1176.

15. Ashby, M. F., Gibson, L. J., Wegst, U. G. K., and Olive, R. (1995). The mechanical properties of natural materials . I . Material property charts. *Proc. R. Soc. Lond. A*, *450*, 123–140.

16. Ashurst, W., and Hoover, W. (1976). Microscopic fracture studies in the two-dimensional triangular lattice. *Phys. Rev. B*, *14*, 1465–1473.

17. Baimova, J. A., and Dmitriev, S. V. (2011). High-energy mesoscale strips observed in two-dimensional atomistic modeling of plastic deformation of nano-polycrystal. *Comput. Mater. Sci.*, *50*, 1414–1417.

18. Barthelat, F. (2014). Designing nacre-like materials for simultaneous stiffness, strength and toughness: Optimum materials, composition, microstructure and size. *J. Mech. Phys. Solids*, *73*, 22–37.

19. Barthelat, F., Dastjerdi, A. K., and Rabiei, R. (2013). An improved failure criterion for biological and engineered staggered composites. *J. R. Soc. Interface*, *10*, 20120849.

20. Begley, M. R., Philips, N. R., Compton, B. G., Wilbrink, D. V., Ritchie, R. O., and Utz, M. (2012). Micromechanical models to guide the development of synthetic 'brick and mortar' composites. *J. Mech. Phys. Solids*, *60*, 1545–1560.

21. Berendsen, H. J. C., Postma, J. P. M., van Gunsteren, W. F., DiNola, a., and Haak, J. R. (1984). Molecular dynamics with coupling to an external bath. *J. Chem. Phys.*, *81*, 3684–3690.

22. Bhowmik, R., Katti, K. S., and Katti, D. R. (2009). Mechanisms of load-deformation behavior of molecular collagen in hydroxyapatite-tropocollagen molecular system: steered molecular dynamics study. *J. Eng. Mech.*, *135*, 413.

23. Bonderer, L. J., Studart, A. R., and Gauckler, L. J. (2008). Bioinspired design and assembly of platelet reinforced polymer films. *Science*, *319*, 1069–73.

24. Bouville, F., Maire, E., Meille, S., Van de Moortèle, B., Stevenson, A. J., and Deville, S. (2014). Strong, tough and stiff bioinspired ceramics from brittle constituents. *Nat. Mater.*, *13*, 508–14.

25. Brandl, C., Derlet, P. M., and Van Swygenhoven, H. (2009). Strain rates in molecular dynamics simulations of nanocrystalline metals. *Philos. Mag.*, *89*, 3465–3475.

26. Branício, P., and Rino, J. (2000). Large deformation and amorphization of Ni nanowires under uniaxial strain: a molecular dynamics study. *Phys. Rev. B*, *62*, 950–955.

27. Broedling, N. C., Hartmaier, A., Buehler, M. J., and Gao, H. (2008). The strength limit in a bio-inspired metallic nanocomposite. *J. Mech. Phys. Solids*, *56*, 1086–1104.

28. Buehler, M. J. (2007). Molecular nanomechanics of nascent bone : fibrillar toughening by mineralization. *Nanotechnology*, *18*, 295102.

29. Buehler, M. J. (2008). *Atomistic Modeling of Materials Failure*. New York: Springer.

30. Buehler, M. J. (2010). Computational and theoretical materiomics: properties of biological and de novo bioinspired materials. *J. Comput. Theor. Nanosci.*, *7*, 1203–1209.

31. Buehler, M. J., Abraham, F. F., and Gao, H. (2003). Hyperelasticity governs dynamic fracture at a critical length scale. *Nature*, *426*, 141–146.

32. Buehler, M. J., Hartmaier, A., Gao, H., Duchaineau, M., and Abraham, F. F. (2004). Atomic plasticity: description and analysis of a one-billion atom simulation of ductile materials failure. *Comput. Methods Appl. Mech. Eng.*, *193*, 5257–5282.

33. Büyüköztürk, O., Buehler, M. J., Lau, D., and Tuakta, C. (2011). Structural solution using molecular dynamics: Fundamentals and a case study of epoxy-silica interface. *Int. J. Solids Struct.*, *48*, 2131–2140.

34. Cammarata, R. C. (1994). Mechanical properties of nanocomposite thin films. *Thin Solid Films*, *240*, 82–87.

35. Carnahan, B., Luther, H. A., and Wilkes, J. O. (1969). *Applied Numerical Methods*. New York: J. Wiley & Sons.

36. Chang, H.-J., Segurado, J., Rodríguez de la Fuente, O., Pabón, B. M., and LLorca, J. (2013). Molecular dynamics modeling and simulation of void growth in two dimensions. *Model. Simul. Mater. Sci. Eng.*, *21*, 075010.

37. Chen, B., Wu, P. D., and Gao, H. (2009). A characteristic length for stress transfer in the nanostructure of biological composites. *Compos. Sci. Technol.*, *69*, 1160–1164.

38. Cho, J., and Sun, C. T. (2007). A molecular dynamics simulation study of inclusion size effect on polymeric nanocomposites. *Comput. Mater. Sci.*, *41*, 54–62.

39. Clegg, W. J., Kendall, K., Alford, N. M., Button, T. W., and Birchall, J. D. (1990). A simple way to make tough ceramics. *Nature*, *347*, 455–457.

40. Cui, W., Li, M., Liu, J., Wang, B., Zhang, C., Jiang, L., and Cheng, Q. (2014). A strong integrated strength and toughness artificial nacre based on dopamine cross-linked graphene oxide. *ACS Nano*, *8*, 9511–9517.

41. Cui, Z., and Brinson, L. C. (2013). Thermomechanical properties and deformation of coarse-grained models of hard-soft block copolymers. *Phys. Rev. E*, *88*, 1–10.

42. Curtin, W. a. (1991). Theory of mechanical properties of ceramic-matrix composites. *J. Am. Ceram. Soc.*, *74*, 2837–2845.

43. Dao, M., Lu, L., Asaro, R. J., Dehosson, J., and Ma, E. (2007). Toward a quantitative understanding of mechanical behavior of nanocrystalline metals. *Acta Mater.*, *55*, 4041–4065.

44. Dieter, G. E. (1988). *Mechanical Metallurgy*. London: Mc Graw-Hill.

45. Dubey, D. K., and Tomar, V. (2008). Microstructure dependent dynamic fracture analyses of trabecular bone based on nascent bone atomistic simulations. *Mech. Res. Commun.*, *35*, 24–31.

46. Dubey, D. K., and Tomar, V. (2010). Role of molecular level interfacial forces in hard biomaterial mechanics: A review. *Ann. Biomed. Eng.*, *38*, 2040–2055.

47. Dunlop, J. W., and Fratzl, P. (2010). Biological composites. *Annu. Rev. Mater. Res.*, *40*, 1–24.

48. Dutta, A., Tekalur, S. A., and Miklavcic, M. (2013). Optimal overlap length in staggered architecture composites under dynamic loading conditions. *J. Mech. Phys. Solids*, *61*, 145–160.

49. Dzenis, Y. A. (2008). Structural nanocomposites. *Science (80-.).*, *319*, 419–420.

50. Espinosa, H. D., Rim, J. E., Barthelat, F., and Buehler, M. J. (2009). Merger of structure and material in nacre and bone-Perspectives on de novo biomimetic materials. *Prog. Mater. Sci.*, *54*, 1059–1100.

51. Evans, A. G. (1990). Perspective on the development of high-toughness ceramics. *J. Am. Ceram. Soc.*, *73*, 187–206.

52. Evans, A. G., and Marshall, D. B. (1989). The mechanical behavior of ceramic matrix composites. *Acta Metall.*, *37*, 2567–2583.

53. Faber, K. T. (1997). Ceramic composite interfaces: properties and design. *Annu. Rev. Mater. Sci.*, *27*, 499–524.

54. Falk, M. L., and Langer, J. (1998). Dynamics of viscoplastic deformation in amorphous solids. *Phys. Rev. E*, *57*, 7192–7205.

55. Ferroni, L. P., and Pezzotti, G. (2002). Evidence for bulk residual stress strengthening in Al_2O_3-SiC nanocomposites. *J. Am. Ceram. Soc.*, *85*, 2033–2038.

56. Frankland, S. J. V., Caglar, A., Brenner, D. W., and Griebel, M. (2002). Molecular simulation of the influence of chemical cross-links on the shear strength of carbon nanotube-polymer interfaces. *J. Phys. Chem. B*, *106*, 3046–3048.

57. Fratzl, P., Gupta, H. S., Paschalis, E. P., and Roschger, P. (2004). Structure and mechanical quality of the collagen–mineral nano-composite in bone. *J. Mater. Chem.*, *14*, 2115.

58. a.G. Frøseth, Derlet, P., and Van Swygenhoven, H. (2004). Dislocations emitted from nanocrystalline grain boundaries: nucleation and splitting distance. *Acta Mater.*, *52*, 5863–5870.

59. Fu, S.-Y., Lauke, B., and Mai, Y.-W. (2009). *Science and Engineering of Short Fibre Reinforced Polymer Composites*. New York: CRC Press.

60. Galema, S., Howardb, E., Engberts, J., and Grigera, J. (1994). The effect of stereochemistry upon carbohydrate hydration. a molecular dynamics next term simulation of β-d-galactopyranose and (α,β)-d-talopyranose. *Carbohydrate Research*, *265*, 215–225.

61. Gao, H. (2006). Application of fracture mechanics concepts to hierarchical biomechanics of bone and bone-like materials. In *Adv. Fract. Res.* (pp. 101–137).

62. Gao, H., Ji, B., Jäger, I. L., Arzt, E., and Fratzl, P. (2003). Materials become insensitive to flaws at nanoscale: lessons from nature. *Proc. Natl. Acad. Sci.*, *100*, 5597–5600.

63. Gil Sevillano, J., van Houtte, P., and Aernoudt, E. (1980). Large strain work hardening and textures. *Prog. Mater. Sci.*, *25*, 69–134.

64. Gleiter, H. (2000). Nanostructured materials: basic concepts and microstructure. *Acta Mater.*, *48*, 1–29.

65. Greer, J. R., and De Hosson, J. T. M. (2011). Plasticity in small-sized metallic systems: Intrinsic versus extrinsic size effect. In *Prog. Mater. Sci.* (pp. 654–724). Elsevier Ltd volume 56.

66. Gupta, H. S., Messmer, P., Roschger, P., Bernstorff, S., Klaushofer, K., and Fratzl, P. (2004). Synchrotron diffraction study of deformation mechanisms in mineralized tendon. *Phys. Rev. Lett.*, *93*, 158101–4.

67. Gupta, H. S., Seto, J., Wagermaier, W., Zaslansky, P., Boesecke, P., and Fratzl, P. (2006). Cooperative deformation of mineral and collagen in bone at the nanoscale. *Proc. Natl. Acad. Sci. U. S. A.*, *103*, 17741–6.

68. Hall, E. O. (1951). The Deformation and Ageing of Mild Steel: III Discussion of Results. *Proc. Phys. Soc. Sect. B*, *64*, 747.

69. Hambli, R., and Barkaoui, A. (2012). Physically based 3D finite element model of a single mineralized collagen microfibril. *J. Theor. Biol.*, *301*, 28–41.

70. Hansen, N. (2004). Hall-petch relation and boundary strengthening. *Scr. Mater.*, *51*, 801–806.

71. He, M.-Y., and Hutchinson, J. W. (1989a). Crack deflection at an interface between dissimilar elastic materials. *Int. J. Solids Struct.*, *25*, 1053–1067.

72. He, M.-Y., and Hutchinson, J. W. (1989b). Kinking of a crack out of an interface. *J. Appl. Mech.*, *111*, 270.

73. H.L.Cox (1952). The elasticity and strength of paper and other fibrous materials. *Br. J. Appl. Phys.*, *3*, 72.

74. Holian, B. L., Wagner, N. J., Chen, S. P., Hoover, W. G., Hoover, C. G., Hammerberg, J. E., and Dontje, T. D. (1991). Effects of pairwise versus many-body forces on high-stress plastic deformation. *Phys. Rev. A*, *43*, 2655–2661.

75. Horstemeyer, M. F., Baskes, M. I., Prantil, V. C., Philliber, J., and Vonderheide, S. (2003). A multiscale analysis of fixed-end simple shear using molecular dynamics, crystal plasticity, and a macroscopic internal state variable theory. *Model. Simul. Mater. Sci. Eng.*, *11*, 265–286.

76. Hsueh, C.-H. (1994). A two-dimensional stress transfer model for platelet reinforcement. *Composites Engineering*, *4*, 1033–1043.

77. Huang, D., Zhang, Q., and Qiao, P. (2011). Molecular dynamics evaluation of strain rate and size effects on mechanical properties of FCC nickel nanowires. *Comput. Mater. Sci.*, *50*, 903–910.

78. Hull, D., and Clyne, T. (1996). *An Introduction to Composite Materials*. Cambridge: Cambridge University Press.

79. Hutchinson, J., and Suo, Z. (1992). Mixed mode cracking in layered materials. *Advances in Applied Mechanics*, *29*, 163–191.

80. Ikeda, H., Qi, Y., Çagin, T., Samwer, K., Johnson, W. L., and Goddard III, W. A. (1999). Strain rate induced amorphization in metallic nanowires. *Phys. Rev. Lett.*, *82*, 2900.

81. Jackson, A. P., Vincent, J. F. V., and Turner, R. M. (1988). The mechanical design of nacre. *Proc. R. Soc. Lond. B.*, *234*, 415–440.

82. Jager, I., and Fratzl, P. (2000). Mineralized collagen fibrils : A mechanical model with a staggered arrangement of mineral particles. *Biophys. J.*, *79*, 1737–1746.

83. Jeon, J. B., Lee, B.-J., and Chang, Y. W. (2011). Molecular dynamics simulation study of the effect of grain size on the deformation behavior of nanocrystalline body-centered cubic iron. *Scr. Mater.*, *64*, 494–497.

84. Ji, B. (2008). A study of the interface strength between protein and mineral in biological materials. *J. Biomech.*, *41*, 259–266.

85. Ji, B. (2010). An atomistic study of the strength of protein-mineral interface of biological materials with a biomimicking model system at nanoscale. *J. Comput. Theor. Nanosci.*, *7*, 7.

86. Ji, B., and Gao, H. (2004). Mechanical properties of nanostructure of biological materials. *J. Mech. Phys. Solids*, *52*, 1963–1990.

87. Ji, B., and Gao, H. (2010). Mechanical principles of biological nanocomposites. *Annu. Rev. Mater. Res.*, *40*, 77–100.

88. Kamat, S., Su, X., Ballarini, R., and Heuer, A. (2000). Structural basis for the fracture toughness of the shell of the conch strombus gigas. *Nature*, *405*, 1036–40.

89. Kampe, S. L., Sadler, P., Christodoulou, L., and Larsen, D. E. (1994). Room-Temperature Strength and Deformation of TiB_2-Reinforced Near-γ Titanium Aluminides. *Metall. Mater. Trans. A*, *25A*, 2181–2197.

90. Kapoor, R., and Nemat-Nasser, S. (1998). Determination of temperature rise during high strain rate deformation. *Mech. Mater.*, *27*, 1–12.

91. Kelchner, C., Plimpton, S., and Hamilton, J. (1998). Dislocation nucleation and defect structure during surface indentation. *Phys. Rev. B*, *58*, 85–88.

92. Kelly, A., and Tyson, W. R. (1965). Tensile properties of fibre-reinforced metals: Copper/ Tungsten and Copper/Molybdenum. *J. Mech. Phys. Solids*, *13*, 329–350.

93. Khandelwal, A., Kumar, A., Ahluwalia, R., and Murali, P. (2017). Crack propagation in staggered structures of biological and biomimetic composites. *Comput. Mater. Sci.*, *126*, 238–243.

94. Kim, J.-K., and Mai, Y.-W. (1998). *Engineered Interfaces in Fiber Reinforced Composites*. Oxford: Elsevier.

95. Koch, C. C., Ovid'ko, I. A., Seal, S., and Veprek, S. (2007). *Structural Nanocrystalline Materials: Fundamentals and Applications*. New York: Cambridge University Press.

96. Koh, A. S. J., and Lee, H.-P. (2006a). Shock-induced localized amorphization in metallic nanorods with strain-rate-dependent characteristics. *Nano Letters*, *6*, 2260–2267.

97. Koh, S. J. A., Lee, H., Lu, C., and Cheng, Q. (2005). Molecular dynamics simulation of a solid platinum nanowire under uniaxial tensile strain: Temperature and strain-rate effects. *Phys. Rev. B*, *72*, 085414.

98. Koh, S. J. A., and Lee, H. P. (2006b). Molecular dynamics simulation of size and strain rate dependent mechanical response of FCC metallic nanowires. *Nanotechnology*, *17*, 3451–67.

99. Kotha, S. P., and Guzelsu, N. (2000). The effects of interphase and bonding on the elastic modulus of bone: changes with age-related osteoporosis. *Med. Eng. Phys.*, *22*, 575–85.

100. Kotha, S. P., Kotha, S., and Guzelsu, N. (2000). A shear-lag model to account for interaction effects between inclusions in composites reinforced with rectangular platelets. *Compos. Sci. Technol.*, *60*, 2147–2158.

101. Kotha, S. P., Li, Y., and Guzelsu, N. (2001). Micromechanical model of nacre tested in tension. *J. Mater. Sci.*, *36*, 2001–2007.

102. Kumar, K., Swygenhoven, H. V., and Suresh, S. (2003). Mechanical behavior of nanocrystalline metals and alloys. *Acta Mater.*, *51*, 5743–5774.

103. LAMMPS Documentation (2015). http://lammps.sandia.gov/doc/Manual.html.

104. Landis, W., Song, M., Leith, A., McEwen, L., and McEwen, B. (1993). Mineral and organic matrix interaction in normally calcifying tendon visualized in 3 dimensions by high-voltage electron-microscopic tomography and graphic image-reconstruction. *Journal of Structural Biology*, *110*, 39–54.

105. Launey, M. E., Buehler, M. J., and Ritchie, R. O. (2010a). On the mechanistic origins of toughness in bone. *Annu. Rev. Mater. Res.*, *40*, 25–53.

106. Launey, M. E., Munch, E., Alsem, D. H., Saiz, E., Tomsia, A. P., and Ritchie, R. O. (2010b). A novel biomimetic approach to the design of high-performance ceramic-metal composites. *J. R. Soc. Interface*, *7*, 741–753.

107. Launey, M. E., and Ritchie, R. O. (2009). On the fracture toughness of advanced materials. *Adv. Mater.*, *21*, 2103–2110.

108. Lei, H. J., Zhang, Z., Han, F., Liu, B., Zhang, Y.-W., and Gao, H. (2013). Elastic Bounds of Bioinspired Nanocomposites. *J. Appl. Mech.*, *80*, 061017.

109. Li, X., Wei, Y., Lu, L., Lu, K., and Gao, H. (2010). Dislocation nucleation governed softening and maximum strength in nano-twinned metals. *Nature*, *464*, 877–80.

110. Libonati, F., Nair, A. K., Vergani, L., and Buehler, M. J. (2013). Fracture mechanics of hydroxyapatite single crystals under geometric confinement. *J. Mech. Behav. Biomed. Mater.*, *20*, 184–191.

111. Libonati, F., Nair, A. K., Vergani, L., and Buehler, M. J. (2014). Mechanics of collagen-hydroxyapatite model nanocomposites. *Mech. Res. Commun.*, *58*, 17–23.

112. Liu, W., Karpov, E., Zhang, S., and Park, H. (2004). An introduction to computational nanomechanics and materials. *Comput. Methods Appl. Mech. Eng.*, *193*, 1529–1578.

113. Louchet, F., Weiss, J., and T., R. (2006). Hall–petch law revisited in terms of collective dislocation dynamics. *Phys. Rev. Lett.*, *97*, 075504.

114. Lu, Q., and Bhattacharya, B. (2005). The role of atomistic simulations in probing the small-scale aspects of fracture - A case study on a single-walled carbon nanotube. *Eng. Fract. Mech.*, *72*, 2037–2071.

115. Luo, Q., Nakade, R., Dong, X., Rong, Q., and Wang, X. (2011). Effect of mineral-collagen interfacial behavior on the microdamage progression in bone using a probabilistic cohesive finite element model. *J. Mech. Behav. Biomed. Mater.*, *4*, 943–52.

116. Luo, S.-N., Zheng, L., An, Q., and Zhao, S. (2006). Tensile Failure of Single-Crystal and Nanocrystalline Lennard-Jones Solids Under Uniaxial Strain. *Int. J. Mod. Phys. C*, *17*, 1551–1561.

117. Lusis, J., Woodhams, R. T., and Xanthos, M. (1973). The effect of flake aspect ratio on the flexural properties of mica reinforced plastics. *Polym. Eng. Sci.*, *13*, 139–145.

118. Maloney, C., and Lemaître, A. (2004). Subextensive scaling in the athermal, quasistatic limit of amorphous matter in plastic shear flow. *Phys. Rev. Lett.*, *93*, 016001.

119. Mara, N. a., and Beyerlein, I. J. (2014). Review: effect of bimetal interface structure on the mechanical behavior of Cu–Nb fcc–bcc nanolayered composites. *J. Mater. Sci.*, *49*, 6497–6516.

120. McEntire, B. J., Bal, B. S., Rahaman, M. N., Chevalier, J., and Pezzotti, G. (2015). Ceramics and ceramic coatings in orthopaedics. *J. Eur. Ceram. Soc.*, *35*, 4327–4369.

121. Meyers, M. A., and Chawla, K. K. (2009). *Mechanical Behavior of Materials*. New York: Cambridge University Press.

122. Meyers, M. A., McKittrick, J., and Chen, P.-Y. (2013). Structural biological materials: critical mechanics-materials connections. *Science*, *339*, 773–9.

123. Meyers, M. A., Mishra, A., and Benson, D. J. (2006). Mechanical properties of nanocrystalline materials. *Prog. Mater. Sci.*, *51*, 427–556.

124. Miller, R. E., and Tadmor, E. B. (2002). The Quasicontinuum Method: Overview, applications and current directions. *J. Comput. Mater. Des.*, *9*, 203–239.

125. Momeni, K. (2014). Enhanced mechanical properties of ZnO nanowire-reinforced nanocomposites: a size-scale effect. *Acta Mech.*, (pp. 1–14).

126. Munch, E., Launey, M. E., Alsem, D. H., Saiz, E., Tomsia, A. P., and Ritchie, R. O. (2008). Tough, bio-inspired hybrid materials. *Science*, *322*, 1516–20.

127. Munilla, J., Castro, M., and Carnicero, A. (2009). Surface effects in atomistic mechanical simulations of Al nanocrystals. *Phys. Rev. B*, *80*, 1–9.

128. Nairn, J. (1997). On the use of shear-lag methods for analysis of stress transfer in unidirectional composites. *Mech. Mater.*, *26*, 63–80.

129. Nalla, R. K., Kinney, J. H., and Ritchie, R. O. (2003). Mechanistic fracture criteria for the failure of human cortical bone. *Nat. Mater.*, *2*, 164–8.

130. Nishioka, T., Syano, S., and Fujimoto, T. (2003). Concepts of separated j-integrals, separated energy release rates, and the component separation method of the j-integral for interfacial fracture mechanics. *Journal of Applied Mechanics- Transactions of the ASME*, *70*, 505–516.

131. Ortiz, C., and Boyce, M. C. (2008). Bioinspired structural materials. *Science (80-.).*, *319*, 1053–1054.

132. Padawer, G., and Beecher, N. (1970). On the strength and stiffness of planar reinforced plastic resins. *Polym. Eng. Sci.*, *10*, 185–192.

133. Pan, Z., Li, Y., and Wei, Q. (2008). Tensile properties of nanocrystalline tantalum from molecular dynamics simulations. *Acta Mater.*, *56*, 3470–3480.

134. Park, H. S., and Zimmerman, J. A. (2005). Modeling inelasticity and failure in gold nanowires. *Phys. Rev. B*, *72*, 054106.

135. Pavia, F., and Curtin, W. A. (2011). Interfacial sliding in carbon nanotube/diamond matrix composites. *Acta Mater.*, *59*, 6700–6709.

136. Pavia, F., and Curtin, W. A. (2013). Molecular modeling of cracks at interfaces in nanoceramic composites. *J. Mech. Phys. Solids*, *61*, 1971–1982.

137. Pei, L., Lu, C., Tieu, K., Zhao, X., Zhang, L., Cheng, K., and Michal, G. (2015). Brittle versus ductile fracture behaviour in nanotwinned FCC crystals. *Mater. Lett.*, *152*, 65–67.

138. Petch, N. (1953). The cleavage strength of polycrystals. *J. Iron Steel Inst.*, *174*, 25–28.

139. Piggott, M. (2002). *Load Bearing Fibre Composites*. New York: Kluwer Academic Publishers.

140. Plimpton, S. (1995). Fast parallel algorithms for short-range molecular dynamics. *Journal of Computational Physics*, *117*, 1–19. `http://lammps.sandia.gov`.

141. Podsiadlo, P., Kaushik, A. K., Arruda, E. M., Waas, A. M., Shim, B. S., Xu, J., Nandivada, H., Pumlin, B. G., Lahann, J., Ramamoorthy, A., and Kotov, N. A. (2007). Ultrastrong and stiff layered polymer nanocomposites. *Science (80-.).*, *318*, 80–83.

142. Pu, Q., Leng, Y., and Cummings, P. T. (2008). Rate-dependent energy release mechanism of gold nanowires under elongation. *J. Am. Chem. Soc.*, *130*, 17907–12.

143. Qi, Y., and Cheng, Y. T. (2004). General Motors R&D Report. *Report Number–9947*, .

144. Qin, Z., Cranford, S., Ackbarow, T., and Buehler, M. J. (2009). Robustness-strength performance of hierarchical alpha-helical protein filaments. *Int. J. Appl. Mech.*, *1*, 85–112.

145. Qin, Z., Gautieri, A., Nair, A. K., Inbar, H., and Buehler, M. J. (2012). Thickness of hydroxyapatite nanocrystal controls mechanical properties of the collagen-hydroxyapatite interface. *Langmuir*, *28*, 1982–1992.

146. Raabe, D. (1998). *Computational Materials Science: The Simulation of Materials, Microstructures and Properties*. New York: J. Wiley & Sons.

147. Rabiei, R., and Bekah, S. (2010). Failure mode transition in nacre and bone-like materials. *Acta Biomater.*, *6*, 4081–4089.

148. Rajan, V., and Curtin, W. A. (2016). Micromechanical design of hierarchical composites using global load sharing theory. *J. Mech. Phys. Solids*, *90*, 1–17.

149. Rapaport, D. C. (2004). *The Art of Molecular Dynamics Simulation*. New York: Cambridge University Press.

150. Rappaz, M., Bellet, M., and Deville, M. (2010). *Numreical Modeling in Materials Science and Engineering*. Berlin: Springer.

151. Rho, J.-Y., Kuhn-Spearing, L., and Zioupos, P. (1998). Mechanical properties and the hierarchical structure of bone. *Med. Eng. Physics;*, *20*, 92–102.

152. Ritchie, R. O. (2011). The conflicts between strength and toughness. *Nat. Mater.*, *10*, 817–822.

153. Rittel, D., a.a. Kidane, Alkhader, M., Venkert, a., Landau, P., and Ravichandran, G. (2012). On the dynamically stored energy of cold work in pure single crystal and polycrystalline copper. *Acta Mater.*, *60*, 3719–3728.

154. Robinson, I. M., and Robinson, J. M. (1994). Review: The influence of fibre aspect ratio on the deformation of discontinuous fibre-reinforced composites. *J. Mater. Sci.*, *29*, 4663–4677.

155. Rosso, M. (2006). Ceramic and metal matrix composites : Routes and properties. *J. Mater. Process. Technol.*, *175*, 364–375.

156. Rottler, J., and Robbins, M. (2003). Shear yielding of amorphous glassy solids: Effect of temperature and strain rate. *Phys. Rev. E*, *68*, 011507.

157. Ruestes, C. J., Bringa, E. M., Stukowski, A., Rodríguez Nieva, J. F., Tang, Y., and Meyers, M. A. (2014). Plastic deformation of a porous bcc metal containing nanometer sized voids. *Comput. Mater. Sci.*, *88*, 92–102.

158. Rühle, M., and Evans, A. G. (1989). High toughness ceramics and ceramic composites. *Prog. Mater. Sci.*, *33*, 85–167.

159. Sadd, M. H. (2009). *Elasticity: Theory, Applications and Numerics*. Cambridge, Massachusetts: Academic Press.

160. Sahputra, I. H., and Echtermeyer, a. T. (2013). Effects of temperature and strain rate on the deformation of amorphous polyethylene: a comparison between molecular dynamics simulations and experimental results. *Model. Simul. Mater. Sci. Eng.*, *21*, 065016.

161. Sahu, R., and Anup, S. (2016). Molecular dynamics study of toughening mechanisms in nano-composites as a function of structural arrangement of reinforcements. *Mater. Des.*, *100*, 132–140.

162. Sainath, G., and Choudhary, B. (2015). Molecular dynamics simulation of twin boundary effect on deformation of Cu nanopillars. *Phys. Lett. A*, *379*, 1902–1905.

163. Sakhavand, N., and Shahsavari, R. (2015). Universal composition–structure–property maps for natural and biomimetic platelet–matrix composites and stacked heterostructures. *Nat. Commun.*, *6*, 6523.

164. Samvedi, V., and Tomar, V. (2009). Atomistic Simulations - Based Understanding of the Mechanism behind the Role of Second-Phase SiC Particles in Fracture Resistance of SiC-Si3N4 Nanocomposites. *Int. J. Multiscale Comput. Eng.*, *7*, 277–294.

165. Schiøtz, J., and Jacobsen, K. W. (2003). A maximum in the strength of nanocrystalline copper. *Science*, *301*, 1357–1359.

166. Schiøtz, J., Tolla, F. D. D., and Jacobsen, K. W. (1998). Softening of nanocrystalline metals at very small grain sizes. *Nature*, *391*, 561–563.

167. Schiøtz, J., Vegge, T., Di Tolla, F. D., and Jacobsen, K. W. (1999). Atomic-scale simulations of the mechanical deformation of nanocrystalline metals. *Phys. Rev. B*, *60*, 11971–11983.

168. Sellinger, A., Weiss, P. M., Nguyen, A., Lu, Y., Assink, R. a., Gong, W., and Brinker, C. J. (1998). Continuous self-assembly of organic-inorganic nanocomposite coatings that mimic nacre. *Nature*, *394*, 256–260.

169. Sen, D., and Buehler, M. J. (2008). Crystal size controlled deformation mechanism: Breakdown of dislocation mediated plasticity in single nanocrystals under geometric confinement. *Phys. Rev. B*, *77*, 195439.

170. Sen, D., and Buehler, M. J. (2009). Size and geometry effects on flow stress in bioinspired de novo metal-matrix nanocomposites. *Adv. Eng. Mater.*, *11*, 774–781.

171. Shao, Y., Zhao, H.-p., and Feng, X.-q. (2014). On flaw tolerance of nacre: a theoretical study. *J. R. Soc. Interface*, *11*, 20131016.

172. Smith, L., Zimmerman, J. a., Hale, L. M., and Farkas, D. (2014). Molecular dynamics study of deformation and fracture in a tantalum nano-crystalline thin film. *Model. Simul. Mater. Sci. Eng.*, *22*, 045010.

173. Sprous, D., Young, M., and Beveridge, D. (1999). Molecular dynamics studies of axis bending in d(G5-(GA4T4C)2-C5) and d(G5-(GT4A4C)2-C5): effects of sequence polarity on DNA curvature. *Journal of Molecular Biology*, *285*, 1623–1632.

174. Sternitzke, M. (1997). Review : structural ceramic nanocomposites. *J. Eur. Ceram. Soc.*, *17*, 1061–1082.

175. Stukowski, A. (2010). Visualization and analysis of atomistic simulation data with OVITO - the Open Visualization Tool. *Modelling Simul. Mater. Sci. Eng.*, *18*, 015012. `http://ovito.org/`.

176. Stukowski, A., Bulatov, V. V., and Arsenlis, A. (2012). Automated identification and indexing of dislocations in crystal interfaces. *Model. Simul. Mater. Sci. Eng.*, *20*, 085007.

177. Su, Y., Ji, B., Hwang, K.-C., and Huang, Y. (2012). Micro-buckling in the nanocomposite structure of biological materials. *J. Mech. Phys. Solids*, *60*, 1771–1790.

178. Suzuki, T., Miyajima, T., and Sakai, M. (1994). The role of the fiber/matrix interface in the first matrix cracking of fiber-reinforced brittle-matrix composites. *Compos. Sci. Technol.*, *51*, 283–289.

179. Tadmor, E. B., and Miller, R. E. (2011). *Modeling Materials: Continuum, Atomistic and Multiscale Techniques*. New York: Cambridge University Press.

180. Tang, M., and Marian, J. (2014). Temperature and high strain rate dependence of tensile deformation behavior in single-crystal iron from dislocation dynamics simulations. *Acta Mater.*, *70*, 123–129.

181. Tang, Z., Kotov, N. a., Magonov, S., and Ozturk, B. (2003). Nanostructured artificial nacre. *Nat. Mater.*, *2*, 413–8.

182. Tomar, V., Gan, M., and Kim, H. S. (2010). Atomistic analyses of the effect of temperature and morphology on mechanical strength of Si-C-N and Si-C-O nanocomposites. *J. Eur. Ceram. Soc.*, *30*, 2223–2237.

183. Tsai, D. (1979). The virial theorem and stress calculation in molecular dynamics. *J. Chem. Phys.*, *70*, 1375.

184. Tsige, M., and Stevens, M. J. (2004). Effect of cross-linker functionality on the adhesion of highly cross-linked polymer networks: a molecular dynamics study of epoxies. *Macromolecules*, *37*, 630–637.

185. Vo, N. Q., Averback, R., Bellon, P., Odunuga, S., and Caro, A. (2008). Quantitative description of plastic deformation in nanocrystalline Cu: Dislocation glide versus grain boundary sliding. *Phys. Rev. B*, *77*, 134108.

186. Vo, N. Q., Averback, R. S., Bellon, P., and Caro, A. (2009). Yield strength in nanocrystalline Cu during high strain rate deformation. *Scr. Mater.*, *61*, 76–79.

187. Voter, A. (1993). Embedded atom method potentials for seven fcc metals: Ni, Pd, Pt, Cu, Ag, Au, and Al. *Los Alamos National Laboratory*, (pp. Unclassified Technical Report No. LA–UR 93–3901).

188. Walker, L. S., Marotto, V. R., Rafiee, M. A., Koratkar, N., and Corral, E. L. (2011). Toughening in graphene ceramic composites. *ACS Nano*, *5*, 3182–3190.

189. Wang, J., Cheng, Q., and Tang, Z. (2012). Layered nanocomposites inspired by the structure and mechanical properties of nacre. *Chem. Soc. Rev.*, *41*, 1111–1129.

190. Wang, J., Wolf, D., Phillpot, S. R., and Gleiter, H. (1996). Computer simulation of the structure and thermo-elastic properties of a model nanocrystalline material. *Philos. Mag. A*, *73*, 517–555.

191. Wang, R., and Gupta, H. S. (2010). Deformation and fracture mechanisms of bone and nacre. *Annu. Rev. Mater. Res.*, *41*, 12.1–12.33.

192. Ward, D. K., Curtin, W. A., and Qi, Y. (2006). Mechanical behavior of aluminum–silicon nanocomposites: A molecular dynamics study. *Acta Mater.*, *54*, 4441–4451.

193. Wegst, U. G. K., Bai, H., Saiz, E., Tomsia, A. P., and Ritchie, R. O. (2015). Bioinspired structural materials. *Nat. Mater.*, *14*, 23–36.

194. Wei, X., Naraghi, M., and Espinosa, H. D. (2012). Optimal length scales emerging from shear load transfer in natural materials: application to carbon-based nanocomposite design. *ACS Nano*, *6*, 2333–44.

195. Weingarten, N. S., and Selinger, R. L. (2007). Size effects and dislocation patterning in two-dimensional bending. *J. Mech. Phys. Solids*, *55*, 1182–1195.

196. Wen, Y., Zhu, Z., and Zhu, R. (2008). Molecular dynamics study of the mechanical behavior of nickel nanowire: Strain rate effects. *Comput. Mater. Sci.*, *41*, 553–560.

197. Wichmann, M. H., Schulte, K., and Wagner, H. D. (2008). On nanocomposite toughness. *Compos. Sci. Technol.*, *68*, 329–331.

198. Winey, K. I., and Vaia, R. A. (2007). Polymer nanocomposites. *MRS Bull.*, *32*, 314–322.

199. Wolf, D., Yamakov, V., Phillpot, S., Mukherjee, a., and Gleiter, H. (2005). Deformation of nanocrystalline materials by molecular-dynamics simulation: relationship to experiments? *Acta Mater.*, *53*, 1–40.

200. Wu, Z., Zhang, Y.-W., Jhon, M. H., Gao, H., and Srolovitz, D. J. (2012). Nanowire failure: long = brittle and short = ductile. *Nano Lett.*, *12*, 910–4.

201. Xia, Z., and Li, L. (2014). Understanding interfaces and mechanical properties of ceramic matrix composites. *Advances in Ceramic Matrix Composites*, (p. 267).

202. Xiao, C., Mirshams, R. A., Whang, S. H., and Yin, W. M. (2001). Tensile behavior and fracture in nickel and carbon doped nanocrystalline nickel. *Mater. Sci. Eng. A*, *301*, 35–43.

203. Yamakov, V., Wolf, D., Phillpot, S. R., Mukherjee, A. K., and Gleiter, H. (2002). Dislocation processes in the deformation of nanocrystalline aluminium by molecular-dynamics simulation. *Nat. Mater.*, *1*, 45–8.

204. Yang, Z., Zhou, Y., Wang, T., Liu, Q., and Lu, Z. (2014). Crack propagation behaviors at Cu/SiC interface by molecular dynamics simulation. *Comput. Mater. Sci.*, *82*, 17–25.

205. Yuan, F., Stock, S. R., Haeffner, D. R., Almer, J. D., Dunand, D. C., and Brinson, L. C. (2011). A new model to simulate the elastic properties of mineralized collagen fibril. *Biomech. Model. Mechanobiol.*, *10*, 147–60.

206. Yuuki, R., and Xu, J. (1992). Stress based criterion for an interface crack kinking out of the interface in dissimilar materials. *Engineering Fracture Mechanics*, *41*, 635–644.

207. Zhang, J., and Ghosh, S. (2013). Molecular dynamics based study and characterization of deformation mechanisms near a crack in a crystalline material. *J. Mech. Phys. Solids*, *61*, 1670–1690.

208. Zhang, L., Lu, C., Zhang, J., and Tieu, K. (2016a). A dual deformation mechanism of grain boundary at different stress stages. *Mater. Lett.*, *167*, 278–283.

209. Zhang, R., Gao, L., and Guo, J. (2004). Preparation and characterization of coated nanoscale Cu / SiC p composite particles. *Ceram. Int.*, *30*, 401–404.

210. Zhang, Y., Gong, S., Zhang, Q., Ming, P., Wan, S., Peng, J., Jiang, L., and Cheng, Q. (2016b). Graphene-based artificial nacre nanocomposites. *Chem. Soc. Rev.*, *45*, 2378–2395.

211. Zhang, Z., Liu, B., Huang, Y., Hwang, K., and Gao, H. (2010). Mechanical properties of unidirectional nanocomposites with non-uniformly or randomly staggered platelet distribution. *J. Mech. Phys. Solids*, *58*, 1646–1660.

212. Zhang, Z., Zhang, Y.-W., and Gao, H. (2011). On optimal hierarchy of load-bearing biological materials. *Proc. Biol. Sci.*, *278*, 519–25.

213. Zhou, M. (2003). A new look at the atomic level virial stress: on continuum-molecular system equivalence. *Proc. R. Soc. A Math. Phys. Eng. Sci.*, *459*, 2347–2392.

214. Ziegenhain, G., Hartmaier, A., and Urbassek, H. M. (2009). Pair vs many-body potentials: Influence on elastic and plastic behavior in nanoindentation of fcc metals. *J. Mech. Phys. Solids*, *57*, 1514–1526.

215. Zienkiewicz, O. C., and Taylor, R. L. (1989). *The Finite Element Method*. New York: Mc Graw-Hill.

216. Zimmerman, J. A., Webb III, E., Hoyt, J., Jones, R., Klein, P., and Bammann, D. (2004). Calculation of stress in atomistic simulation. *Model. Simul. Mater. Sci. Eng.*, *12*, S319–S332.

LIST OF PUBLICATIONS BASED ON THE RESEARCH WORK

Publications in Peer-Reviewed International Journals

1. S. Mathiazhagan, S. Anup, (2016), Influence of platelet aspect ratio on the mechanical behavior of bio-inspired nanocomposites using molecular dynamics, ***Journal of the Mechanical Behavior of Biomedical Materials***, Vol–59, pp.21–40. (DOI:10.1016/j.jmbbm.2015.12.008)

2. S. Mathiazhagan, S. Anup, (2016), Investigation of deformation mechanisms of staggered nanocomposites using molecular dynamics, ***Physics Letters A***, Vol–380, pp.2849–2853. (DOI:10.1016/j.physleta.2016.06.046)

3. S. Mathiazhagan, S. Anup, (2016), Mechanical behaviour of bio-inspired brittle-matrix nanocomposites under different strain rates using molecular dynamics, ***Molecular Simulation***, Vol–42, pp.1490–1501 (DOI:10.1080/08927022.2016.1205192)

4. S. Mathiazhagan, S. Anup, Atomistic studies on the length scale effect of bio-inspired brittle-matrix nanocomposites, ***(Under Review)***.

5. S. Mathiazhagan, S. Anup, Atomistic studies on the effect of interface strength on bio-inspired brittle-matrix nanocomposites, ***(To be submitted)***.

Presentations in Conferences

1. S. Mathiazhagan, S. Anup, (2012), Numerical study on nanoscale failure mechanism of bone, ***Fourth International Congress on Computational Mechanics and Simulation (ICCMS-2012)***, IIT Hyderabad, 9-12 December,2012

2. S. Mathiazhagan, S. Anup, (2013), Mechanical behavior of bone nanostructure using molecular dynamics methods, ***Indian Conference on Applied Mechanics (INCAM)***, IIT Madras, 4-6 July,2013
   ISBN: 978-93-5137-273-8

3. S. Mathiazhagan, S. Anup, (2014), Studies on the effect of strain-rate on a bio-inspired nanocomposite using molecular dynamics, ***Fifth International Congress on Computational Mechanics and Simulation (ICCMS-2014)***, CSIR-SERC Chennai, 10-13 December, 2014 ***ISBN: 978-981-09-1139-3*** ,
online at "`http://dx.doi.org/10.3850/978-981-09-1139-3_067`"

4. S. Mathiazhagan, S. Anup, (2016), Length scale effect on the deformation behaviour of bio-inspired nanocomposites using molecular dynamics, ***Sixth International Congress on Computational Mechanics and Simulation (ICCMS-2016)***, IIT Bombay, 27 June–1 July, 2016